SEARCH FOR W' PRODUCTION IN THE SINGLE-TOP CHANNEL WITH THE ATLAS DETECTOR

By

Patrick True

A DISSERTATION

Submitted to
Michigan State University
in partial fulfillment of the requirements
for the degree of

Physics - Doctor of Philosophy

2015

ABSTRACT

SEARCH FOR W' PRODUCTION IN THE SINGLE-TOP CHANNEL WITH THE ATLAS DETECTOR

By

Patrick True

This thesis presents the search for $W' \rightarrow t\bar{b}$ using the LHC pp collision data collected with the ATLAS detector at a center-of-mass energy of 8 TeV. The primary backgrounds to this search are ttbar, W+jets, and multijets processes. To reduce the contributions of these backgrounds we require a leptonic final state and use Boosted Decision Trees to discriminate between signal and background-like events. This measurement gives limits on the $W' \rightarrow t\bar{b}$ cross-section times branching ratio and on the coupling strength of the W' boson as a function of its mass.

ACKNOWLEDGMENTS

First and foremost I would like to thank my wife Amber for her infinite support while I wrote this thesis. I would not be the person I am today without her.

I would like to thank my advisor Kirsten Tollefson for teaching me the ropes of working in high energy physics and always having good advice. It would be impossible to list all the ways she has helped me through graduate school.

Thanks to Barbara Alvarez for mentoring me for several years and helping me to code, troubleshoot, and understand all the tiny details that go into physics research.

Thanks to all the other graduate students and postdocs at MSU, especially James Koll, Jenny and Jeremiah Holzbauer, JT Laverty and Brad Schoenrock for your friendship and help over these six years.

Thanks to all the support staff, in particular Brenda Wenzlick and Debbie Barratt for making sure I stayed enrolled, got paid, and successfully navigated graduate school.

Thanks to my committee members for accepting the task of reviewing my work and providing me unparralleld insight and advice.

Finally I have to thank my family for their love and support for all of these years. Without them none of this would have been possible.

TABLE OF CONTENTS

LIST OF TABLES

LIST OF FIGURES

Chapter 1

Introduction

Humans have always sought to understand their environment. People have progressed from an intuitive understanding of the universe based on practical experience to a more scientific understanding based on logic and the rigorous study of phenomena. The understanding brought about by science has allowed humanity to achieve feats which would otherwise be impossible, and we continue to seek more understanding. At the forefront of this quest, particle physicists work to understand the most basic components of the universe and the most fundamental of interactions between them. Our understanding of the universe has progressed from classical theories of the four natural elements, through the chemical elements and nuclear structure, to modern relativistic quantum field theories that describe the most fundamental objects yet imagined. Continuing research in the field takes many forms: precision measurements of trapped and isolated atoms over months allow theoretical models to be tested, detection of particles accelerated by supernovae and other astronomical objects allows access to an energy regime physicists are unable to recreate on Earth, and experiments at particle colliders allow for the investigation of the rarest phenomena.

This dissertation describes a search for a new particle using the largest detector in the world at the highest energy particle collider ever built and is part of an international research program in collaboration with a multinational research group, specifically the search for $W' \to t\bar{b}$ using the ATLAS detector at CERN. Similar searches have previously been performed by collaborations at CERN and Fermilab and their results are described in Section 8.4. This analysis is the first search for $W' \rightarrow t\bar{b}$ using the ATLAS detector to include events with 1 b-tagged jet, as described in Chapter 5. This approximately doubles the signal acceptance relative to the previous ATLAS search for $W' \rightarrow t\bar{b}$. These additional events are kinematically distinct from the events with 2 b-tagged jets and the entire analysis has been optimized in 4 independant channels based on the jet content of the events. This analysis also uses a larger dataset than the previous ATLAS search and uses the latest recomendations for event simmulation, data callibration, and the estimation of systematic uncertainties. Thus this analysis is expected to be currently the most sensitive search for $W' \rightarrow t\bar{b}$ using the ATLAS detector.

Throughout this text the natural unit system is used in which $c = 1$, $\hbar = 1$, and $e = 1$. Energies and momenta are expressed in electronvolts (eV), where 1 eV is the energy gained by a unit charge traversing a 1 Volt electric potential. This dissertation is divided into chapters intended to first establish the environment the analysis takes place in, to build up the analysis from basic components, and finally to present the results and put them into context with the rest of the field. Towards this end the chapters are as follows:

- **Chapter 2** discusses the theoretical background for the analysis.
- **Chapter 3** describes the physical apparatus of the experiment.
- **Chapter 4** defines the analysis level objects reconstructed from the detector response.
- **Chapter 5** defines the criteria for an event to be included in the analysis.
- **Chapter 6** details the simulation methods used to model the backgrounds and potential signal processes.

- **Chapter 7** describes the multivartiate analysis technique and its specific implementation.
- **Chapter 8** details the results of the analysis and their statistical significance.
- **Chapter 9** discusses the results of the analysis and their context in current research.
- **Appendix A** describes alternative multivariate analysis optimizations which were investigated for the analysis but not used in the final result.

Chapter 2

Theory

High energy physics attempts to deal with the fundamental particles and forces of the universe, and the Standard Model (SM) of high energy physics is the theoretical framework used in this analysis. The Standard Model describes the universe as being composed of 17 fundamental particles and their interactions through three of the four fundamental forces. This thesis is a search for a W' particle not included in the Standard Model which would be indicative of extended physical theories, collectively called Beyond the Standard Model (BSM) theories. There are a wide variety of BSM theories therefore this analysis is performed in a model-independent manner using an effective Lagrangian which has a form that many of these theories which include a W' boson can be reparameterized into. The motivation behind searching for a W' is explored by examining some representative BSM theories and their consequences. The focus of this chapter is not to derive the Standard Model or any BSM theories from first principles, but rather to provide a practical framework and context in which to understand this analysis and the implications of the results. There are a number of texts which provide a more comprehensive overview of particle physics [13, 14] or a more rigorous derivation of the mathematical models used [15, 16].

2.1 The Standard Model

The Standard Model has provided accurate predictions of experimental observables for over 40 years. It was developed after decades of experimentation had catalogued a myriad of particle states. The properties of these states were observed to follow patterns and symmetries, and eventually these symmetries were developed into the Standard Model. The symmetries of the Standard Model are described in group theory terms as $SU(3) \otimes SU(2) \otimes U(1)$ with each symmetry giving rise to its own conservation law. The Standard Model is a quantum field theory arising from a unification of quantum mechanics and special relativity, and is mathematically described by a Lagrangian [16].

2.1.1 The forces

The Standard Model includes three of the four fundamental forces of nature: the electromagnetic, weak, and strong forces - but not the gravitational force as no complete quantum mechanical theory of gravity has been discovered yet. The electromagnetic and weak forces can be unified into a single electroweak force similar to the unification of the electric and magnetic forces into the electromagnetic force. The electroweak force is described by the $SU(2) \otimes U(1)$ symmetry of the Standard Model and is mediated by the massless photon as well as the massive $W^{\pm}$ and Z bosons which are described in Section 2.1.2. One of the greatest theoretical achievements of the Standard Model was the prediction of the existence of the $W^{\pm}$ and Z bosons well before their experimental discovery. The strong force is described by the $SU(3)$ symmetry of the Standard Model and is mediated by massless gluons which are described in Section 2.1.2. The strong force differs from the electroweak force in that the strong force grows with increased distance between objects which has unique consequences when compared to the electroweak force which diminishes with distance. There have been many attempts to unify the strong force with the electroweak force and even to include a quantum field theory of gravity, such as supersymmetry or string theory. However, there is no clear experimental evidence to support these theories and they are not part of the Standard Model [14].

The electroweak force is a unification of the electric, magnetic, and weak forces. The electric and magnetic forces were unified by Maxwell in 1879, and were described as a quantum field theory called quantum electrodynamics (QED) by Dirac in the 1920's. The resulting electromagnetic force decreases as the distance between objects increases, and the force is carried to infinite distance by its massless mediator, the photon. The weak force is responsible for a wide range of observed phenomena, including nuclear beta decay and the violation of parity and charge-conjugation invariance. The violation of these symmetries is due to the weak force only interacting with the left-handed chirality of particles and fields. These processes can be described with phenomenological theories at low and intermediate energies, however at higher energies, above a few GeV, these phenomenological weak theories break down. Unlike the electromagnetic force which is caried to an infinite distance by the massless photon, the weak force is mediated by the massive $W^{\pm}$ and Z bosons and so has a limited range of typically 2.5 am, less than the radius of a proton. It is only after unification that electroweak theory provides consistent predictions for the energy ranges probed by modern accelerators of up to several TeV [14].

The strong force is responsible for holding baryons, mesons, and nuclei together and is described in the Standard Model by quantum chromodynamics (QCD). QCD describes the strong force using a type of charge called "color" which comes in three types of colors and their anti-colors. Quarks each carry either a color or anti-color charge; whereas gluons, the mediating particles of the strong force, carry both a color and an anti-color charge. The color charge carried by the gluons is a key difference between QCD and QED - in which the mediating particle is charge neutral. This means that gluons are self-interacting and so it is a non-Abelian gauge theory. This self-interaction also leads to anti-shielding of bare color charges by the vacuum and the force between colored objects becoming larger as the distance between them increases. This corresponds to the fact that only colorless objects are observed in nature, either those objects without a color charge or which are compsed of objects which have no net color charge. If the color charged constituent particles of such a composite object begin to separate it becomes energetically favorable to pair-produce new colored particles from the vacuum which will form new colorless bound states with the original color charged particles. When very energetic colored particles are produced, such as from the decay of a heavy resonance, this process is rapidly repeated which causes the formation of particle showers called "jets", as discussed further in Section 2.1.2.1 [14].

2.1.2 The particles

The Standard Model contains 17 fundamental particles and their anti-particles which compose all objects. These particles can be classified into three types called leptons, quarks, and bosons as shown in Table 2.1. For each particle in Table 2.1 there is a corresponding anti-particle with opposite electric charge. In general a particle name or symbol refers to both the particle and its anti-particle except where they are explicitly distinguished. Thus "electron" refers to both electrons and positrons. The structure visible in Figure 2.1 of quarks and leptons both having three generations of pairs, with each lepton pair consisting of a charged lepton and neutrino and each quark pair consisting of an "up-type" quark with an electric charge of $2/3$ and one "down-type" quark with electric charge $-1/3$, is not accidental and is vital to our understanding of the particles.

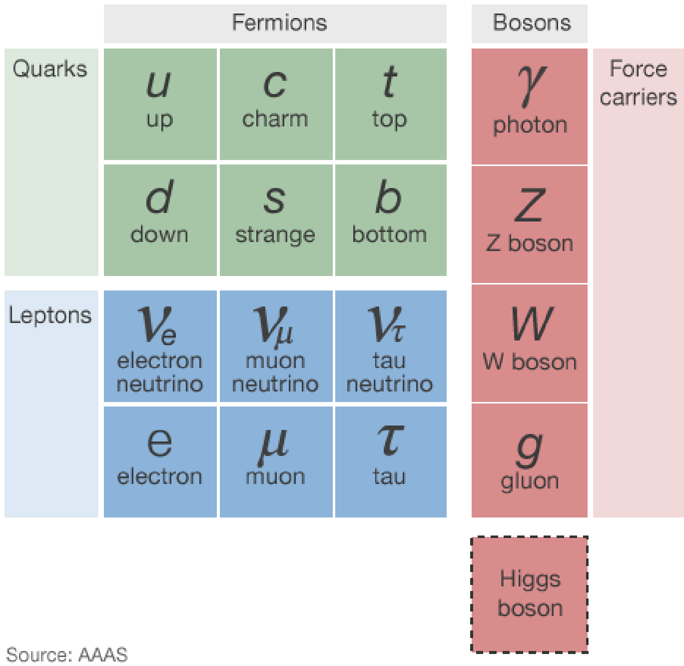

Figure 2.1: Diagram of the Standard Model particles grouped into bosons and fermions, with the fermions further grouped into quarks and leptons with three generations of pairs each [4].

The six lepton flavors (electron, electron neutrino, muon, muon neutrino, tau, tau neutrino) can be classified into 3 generations, each containing a charged lepton and its neutrino. The charged leptons all have mass and carry an electrical charge of -1, while the neutrinos are electrically neutral but their masses have not been directly observed. The observation of neutrino flavor oscillations [17] implies that neutrinos are not massless and the current best limits on the mass of each neutrino flavor are given in Table 2.1. Leptons do not interact through the strong force, the charged leptons interact through the weak and electromagnetic forces while the neutrinos only interact weakly. Because neutrinos can only interact through the weak force their interaction with matter, such as a detector, is rare and specialized experiments are necessary to study them. In contrast the first generation charged lepton, the electron, is easily detected through electromagnetic interactions and is readily available in nature. This difference in detectability has led to the term "lepton" generally indicating the charged leptons with the neutrinos being indicated separately. Experimentalists often further restrict lepton to mean only electrons and muons because taus decay within a particle detector and are difficult to identify. This convention will be followed in the experimental portions of this thesis.

Similar to the leptons, the quarks (up, down, charm, strange, top, bottom) can also be described by 3 generations, each containing 2 flavors. Each generation contains one quark with an electric charge of $2/3$ and one quark with an electric charge of $-1/3$, called up-type and down-type respectively based on the first generation quarks with those charges. Quarks interact through all 3 of the forces in the Standard Model and thus are readily detectable using a variety of methods. Since quarks have a color charge, bare quarks are not directly detectable but will form jets as described in Section 2.1.2.1.

The final group of particles in Table 2.1 are the bosons. The bosons all have integer spins, with the photon, gluon, $W^{\pm}$ and Z bosons all being spin 1 and the Higgs boson being spin 0. The photon, $W^{\pm}$ and Z bosons are the mediating particles of electroweak theory with the $W^{\pm}$ boson having an electric charge of ± 1 and the photon and Z boson being electrically neutral. The $W^{\pm}$ and Z bosons are massive, unlike the photon, and they gain their masses through the Higgs mechanism. The Higgs mechanism adds a quartic complex scalar field potential to the Lagrangian density, described in Section 2.1.3, which is locally gauge invariant. Through an appropriate choice of parameters the field is made to have a non-zero expectation value and induce spontaneous symmetry breaking in the $SU(2) \otimes U(1)$ electroweak group. What is left is the massive $W^{\pm}$ and Z bosons, the massless photon, and a new massive Higgs boson, which was just recently discovered at the LHC [18, 19]. The final boson is the gluon which mediates the strong force. The gluon has a color and anti-color charge which makes it self-interacting as described in Section 2.1.1, and a bare gluon will form a jet, as described in Section 2.1.2.1, similar to a bare quark.

Particle	Symbol	Mass	Charge [e]	Spin
Leptons				
Electron	e	511 KeV	-1	1/2
Electron Neutrino	ν_e	<2.05 eV	0	1/2
Muon	μ	106 MeV	-1	1/2
Muon Neutrino	ν_μ	<0.17 MeV	0	1/2
Tau	τ	1.78 GeV	-1	1/2
Tau Neutrino	ν_τ	<18.2 MeV	0	1/2
Quarks				
Up	u	2.3 MeV	2/3	1/2
Down	d	4.8 MeV	$-1/3$	1/2
Charm	c	1.28 GeV	2/3	1/2
Strange	s	95 MeV	$-1/3$	1/2
Top	t	173 GeV	2/3	1/2
Bottom	b	4.18 GeV	$-1/3$	1/2
Bosons				
Photon	γ	0	0	1
$W^\pm$ Boson	$W^\pm$	80.4 GeV	$\pm$ 1	1
Z Boson	Z	91.2 GeV	0	1
Gluon	g	0	0	1
Higgs	H	126 GeV	0	0

Table 2.1: The fundamental particles of the Standard Model and their properties [1].

2.1.2.1 Jets

Jets are phenomenological objects that are formed when individual colored particles, single quarks and gluons, are produced at sufficiently high energies. As the colored particle moves away from the initial colored object it is connected to, the energy of the strong interaction between them increases until it becomes energetically favorable to produce a quark-antiquark pair from the vacuum for the particle and the initial colored object to be bound to. This bound state has no net color and is called a hadron. The production of new hadrons is called hadronization and each hadron produced absorbs a small amount of the initial colored particle's energy. This process will repeat itself until there is insufficient energy remaining for further hadronization, which is when the energies of the processes involved drop to the mass of the lightest hadron. This creates a narrow shower of hadrons that in total have the same energy and momentum as the original colored particle. This particle shower is called a "jet" and it is the detectable product of the original color charged particle. This is a general picture of what happens to quarks and gluons but there are subtle differences depending on the flavor of the initial particle, in particular if the initial particle is a top or bottom quark. Because of its large mass, a top quark almost exclusively decays into a $W^{\pm}$ boson and bottom quark before hadronization can occur, creating a very different signal from other quarks. Bottom quarks also have unique phenomenology in that the hadron produced with the initial bottom quark has an unusually long lifetime and will travel a considerable distance in a detector before the b quark decays and further hadronization takes place. By carefully tracking the trajectories of the products of the hadronization in these jets and projecting them backwards, a secondary production vertex can be formed which is displaced from the primary production vertex of the other objects in an event [14].

2.1.3 The Lagrangian

In order to concisely describe the mathematics behind the Standard Model it is necessary to define some common notation. Einstein summation notation is used throughout this section and any repeated index in a term is summed over. In all of the equations in this section, B, W^i, and G^j are vector potentials with 1 time-like dimension and 3 space-like dimensions and all Greek lettered indices, namely μ and ν, run over these four dimensions. There is one electromagnetic potential (B), three weak potentials (W^i), and eight strong potentials (G^j).

For each potential B, W^i, and G^j, g is a coupling constant that determines the strength of the interaction between an object and that potential. The Dirac matrices are the generators of the Minkowski space with 1 time-like dimension and 3 space-like dimensions. The Dirac matrices are denoted as γ, and are given in the Dirac representation in Equation 2.1. Finally, the chirality operator γ^5 is not a Dirac matrix but is defined in terms of them in Equation 2.2. γ^5 is important for describing left-handed and right-handed interactions, with the left-handed projection having the form $\frac{1-\gamma^5}{2}$ and the right-handed projection having the form $\frac{1+\gamma^5}{2}$.

$$\gamma^0 = \begin{pmatrix} 1 & 0 & 0 & 0 \\ 0 & 1 & 0 & 0 \\ 0 & 0 & -1 & 0 \\ 0 & 0 & 0 & -1 \end{pmatrix}, \gamma^1 = \begin{pmatrix} 0 & 0 & 0 & 1 \\ 0 & 0 & 1 & 0 \\ 0 & -1 & 0 & 0 \\ -1 & 0 & 0 & 0 \end{pmatrix}$$
$$\gamma^2 = \begin{pmatrix} 0 & 0 & 0 & -i \\ 0 & 0 & i & 0 \\ 0 & i & 0 & 0 \\ -i & 0 & 0 & 0 \end{pmatrix}, \gamma^3 = \begin{pmatrix} 0 & 0 & 1 & 0 \\ 0 & 0 & 0 & -1 \\ -1 & 0 & 0 & 0 \\ 0 & 1 & 0 & 0 \end{pmatrix} \tag{2.1}$$

$$\gamma^5 = i\gamma^0\gamma^1\gamma^2\gamma^3 = \begin{pmatrix} 0 & 0 & 1 & 0 \\ 0 & 0 & 0 & 1 \\ 1 & 0 & 0 & 0 \\ 0 & 1 & 0 & 0 \end{pmatrix} \tag{2.2}$$

The mathematics of the Standard Model are typically formulated in terms of a Lagrangian L and its density $\mathcal{L}$, such that $L = \int \mathcal{L} d^3x$. The Standard Model includes many different phenomena so it is useful to group the terms of the Lagrangian density by their physical motivation as seen in Equation 2.3 [15].

$$\mathcal{L} = \mathcal{L}_{EW} + \mathcal{L}_{QCD} + \mathcal{L}_{YUK} \tag{2.3}$$

Here $\mathcal{L}_{EW}$ is the electroweak Lagrangian denstiy which describes the electroweak interaction mediated by the photon, $W^{\pm}$ and Z bosons, as well as the Higgs mechanism and the Higgs boson, $\mathcal{L}_{QCD}$ is the QCD Lagrangian density which describes the strong interaction between gluons and quarks, and $\mathcal{L}_{YUK}$ is the Yukawa Lagrangian density which describes the fermions and how they derive their mass from the Higgs mechanism.

The Lagrangian density that describes the electroweak force ($\mathcal{L}_{EW}$) is given in Equation 2.4.

$$\mathcal{L}_{EW} = -\frac{1}{4}B_{\mu\nu}B^{\mu\nu} - \frac{1}{4}W_{\mu\nu i}W_i^{\mu\nu} + \bar{l}_L^F\gamma^\mu D_\mu l_L^F + \bar{e}_R^F\gamma^\mu D_\mu e_R^F + D_\mu\phi D^\mu\phi - \mu^2\phi^2 - \lambda(\phi^2)^2 \tag{2.4}$$

The first two terms describe the electroweak fieldss with the index i running over the three weak fields associated with the $W^{\pm}$ and Z bosons. $B_{\mu\nu}$ is the electromagnetic field tensor and is defined as:

$$B_{\mu\nu} = \partial_\mu B_\nu - \partial_\nu B_\mu \tag{2.5}$$

while $W_{\mu\nu i}$ are the three weak field tensors, given in Equation 2.6 where ϵ_{ijk} is the Levi-Civita tensor.

$$W_{\mu\nu i} = \partial_\mu W_{\nu i} - \partial_\nu W_{\mu i} + ig_w \epsilon_{ijk} W_{\mu j} W_{\nu k} \tag{2.6}$$

The third and fourth terms of Equation 2.4 describe the left-handed fermions and right-handed fermions respectively, with the index F running over the three generations. D_μ is the covariant derivative, which is defined as:

$$D_\mu = \partial_\mu - gB_\mu - \frac{1}{2} g_w (1 - \gamma_5) W_{\mu i} \tag{2.7}$$

The last three terms of Equation 2.4 describe the Higgs field ϕ. The first of these is the kinetic term for the Higgs field. The final two terms of the electroweak Lagrangian density describe the Higgs potential which is quartic in ϕ. In these terms μ and λ are parameters which determine the shape of the Higgs potential, where a negative value for μ^2 and a positive value for λ produces a Higgs potential with a minimum value at a finite $\phi \neq 0$ which causes spontaneous symmetry breaking and gives the $W^\pm$ and Z bosons mass.

The QCD Lagrangian density ($\mathcal{L}_{QCD}$) is given in Equation 2.8.

$$\mathcal{L}_{QCD} = \sum_j \bar{\psi}_m (i\gamma^\mu D_\mu - m_j \delta_{mn}) \psi_n - \frac{1}{4} G_{\mu\nu a} G_a^{\mu\nu} \tag{2.8}$$

The first term describes the quarks with index j running over all six of the quarks with masses m_j, and the m and n indices running over the three colors. The covariant derivative D_μ is similar to Equation 2.7 but now contains eight gauge fields (A_a) corresponding to the eight gluons denoted by the index a:

$$D_\mu = \left(\partial_\mu - gB_\mu - \frac{1}{2} g_w (1 - \gamma_5) W_{\mu i} \right) \delta_{mn} + ig_s T_{mna} A_{\mu a} \tag{2.9}$$

where T_{mna} are the Gell-Mann matrices which are the generators of the $SU(3)$ QCD group which indicate that when a gluon interacts with a quark it changes the quark's color, and g_s is the strong coupling strength.

The second term of the QCD Lagrangian density describes the gluons. $G_{\mu\nu a}$ is analogous to $B_{\mu\nu}$ in the electroweak Lagrangian density, but for each of the eight gauge fields.

$$G_{\mu\nu a} = \partial_\mu A_{\nu a} - \partial_\nu A_{\mu a} - g_s f_{abc} A_{\mu b} A_{\nu c} \tag{2.10}$$

The f_{abc} in Equation 2.10 are the structure constants of the QCD $SU(3)$ group, which are related to the generators of the group according to Equation 2.11.

$$[T_a, T_b] = i f_{abc} T_c \tag{2.11}$$

The Yukawa Lagrangian density ($\mathcal{L}_{YUK}$) describes the fermions' interactions with the Higgs field and is given in Equation 2.12.

$$\mathcal{L}_{YUK} = \sum_f \bar{\psi} G_f \phi \psi \tag{2.12}$$

The index f runs over the fermions, with the covariant derivative defined in Equation 2.7. The mass of each fermion is determined by $G_f \phi$ where G_f is the fermion's coupling to the Higgs field ϕ, and in this way the Higgs field gives the fermions their masses.

2.2 Beyond the Standard Model theories

While the Standard Model has described the observations of particle physics experiments for over 40 years, there are known problems with the theory. Some examples are:

- The Standard Model does not include gravity, a force which has been experimentally verified to exist.

- There is no mechanism to produce the amount of matter-antimatter asymmetry that is observed in the universe today.

- The Standard Model does not include a suitable dark matter particle to match astronomical observations. While mathematically possible, the observed masses of the $W^{\pm}$ and Z bosons require very precise cancellations of parameters which seems unnatural.

While this list is by no means exhaustive, there have been decades of work to solve these problems with Beyond the Standard Model (BSM) theories.

2.2.1 W' boson

Many of these BSM theories predict additional particles beyond those of the Standard Model. Often these new particles are related to the Standard Model particles, such as through a new symmetry in the BSM theory, and the BSM particles and SM particles share many of the same properties. It is common practice in these cases to call the BSM particles by the name of their SM counterparts but with a prime, thus a W' boson is similar to a Standard Model $W^{\pm}$ boson. In particular a W' boson is a massive, spin-1, colorless particle with an electrical charge of ± 1. The W' boson couplings are determined by each specific BSM theory [20, 21, 22] and they may be similar to the $W^{\pm}$ boson couplings in the Standard Model or they may be very different. In cases where the W' couplings are similar to the Standard Model $W^{\pm}$ couplings the most sensitive decay channel to search for at particle colliders is usually $W' \rightarrow l\nu$. If the leptonic couplings of the W' boson are very small or if the leptonic decay of the W' boson is suppressed for some other reason in the BSM theory, such as if a right-handed W' boson were to decay to a right-handed BSM neutrino but the right-handed neutrino is more massive than the W' boson, then another decay channel of the W' boson to search for is $W' \to t\bar{b}$. The third generation (top and bottom) quark decay is specified because some BSM theories predict an enhanced coupling of the W' boson to the third generation and also because there are fewer Standard Model processes that produce this state which provides an advantage in the experimental analysis.

2.2.2 Extensions of $SU(2) \otimes U(1)$

Theories that include a W' boson often extend the $SU(2)\otimes U(1)$ electroweak symmetry which describes the $W^{\pm}$ boson. The simplest such extension is $SU(2) \otimes SU(2) \otimes U(1)$, where the new $SU(2)$ can be a right-handed extension of the left-handed $SU(2)$ group which describes the Standard Model weak interactions or some other $SU(2)$ symmetry. The $SU(2) \otimes U(1)$ symmetry can also be extended by embedding the $SU(2)$ into a group of higher degree, resulting in symmetries such as $SU(3) \otimes U(1)$ or $SU(4) \otimes U(1)$. Each of these extensions contains a myriad of specific theories with different coupling structures and a variety of experimental predictions [1, 20, 21, 22]. Since there is currently no strong experimental evidence to distinguish between these theories, this analysis does not assume any specific theory but instead uses an effective Lagrangian approach.

2.2.3 Effective Lagrangian approach

In all of these theories the W' boson is described by a Lagrangian density term of the form given in Equation 2.13 [3] which is added to the Standard Model Lagrangian density in Equation 2.3.

$$\mathcal{L}_{W'} = \frac{1}{2\sqrt{2}} V'_{ij} W'_\mu \bar{f}^i \gamma^\mu (g'_R(1+\gamma_5) + g'_L(1-\gamma_5)) f^j \tag{2.13}$$

This Lagrangian density includes arbitrary right-handed and left-handed coupling strengths g'_R and g'_L respectively. These coupling strengths are a common feature across all models regardless of how they are determined within each theory, and thus they are a model-independant parameter which can be experimentally measured or constrained. In principle these coupling strengths can be flavor-dependant, however for this analysis the coupling strengths are assumed to be flavor-universal. The right-handed and left-handed couplings are analyzed independantly using benchmark models where one of the BSM couplings g'_R or g'_L is equal to the Standard Model coupling g for $W^\pm$ boson and the other BSM coupling is zero. These benchmark models are refered to as the W'_R and W'_L models respectively.

Chapter 3

ATLAS and the LHC

The search for $W' \to t\bar{b}$ requires a very large and extensive experimental setup. In order to set limits competitive to those currently in the literature [23, 24, 25, 26], particles need to be collided with at least several TeV of energy, and in order to correctly distinguish W' events from background events, the products of these collisions need to be carefully measured. The ATLAS (A Toroidal Lhc ApparatuS) experiment meets these criteria, it is the largest collider detector ever built and is capable of very precise measurements of the products of particle collisions. The collisions it measures are produced by the Large Hadron Collider (LHC) which is designed to collide protons with up to 14 TeV[1] center-of-mass-energy and is located at CERN near Geneva, Switzerland.

3.1 The Large Hadron Collider

3.1.1 The Accelerator Chain

The LHC is only the final accelerator in a chain designed to take ions from rest, accelerate and collide them at up to 14 TeV center-of-mass-energy. This acceleration occurs in stages, with protons being accelerated through a separate chain than other ions such as lead. The entire CERN accelerator chain is shown in Figure 3.1. Since this analysis uses proton-proton

[1] Units are expressed throughout this thesis using SI prefixes, so 1 TeV = 10^{12} eV, 1 GeV = 10^9 eV, 1 MeV = 10^6 eV where 1 eV = 1.6×10^{-19} Joules.

collisions only their acceleration is detailed here. The proton source is a bottle of hydrogen gas, which is stripped of its electrons and accelerated to a 50 MeV proton beam by the Linac2 linear accelerator [27]. This 50 MeV proton beam is then passed to the Proton Synchroton Booster (PSB) which accelerates the beam to 1.4 GeV in four superimposed synchrotron rings before injecting the bunches into the Proton Synchrotron (PS). By adjusting the timings of the four superimposed rings of the PSB and varying which rings the PS is filled from, a plethora of bunch patterns can be selected based on the current operating goals [28]. The PS accelerates the proton beam from 1.4 GeV to 25 GeV in a 628 meter circumference synchrotron. The PS also does the final bunch splitting, creating the bunch pattern which will be kept through the remainder of the beam acceleration and collision [29]. After being accelerated and bunched by the PS, the beams enter the Super Proton Synchrotron (SPS) for final acceleration and tuning before injection into the LHC. The SPS is a synchrotron nearly 7 km in circumference which accelerates the proton beam up to 450 GeV before injecting it into the LHC [30].

The final stage of the accelerator chain is the LHC itself. The LHC is a 27 km circumference synchrotron with 2 superimposed rings which reside in what was previously the Large Electron-Positron collider (LEP) tunnel. It consists of 1104 superconducting dipole magnets designed to reach a peak field of 8.33 T to bend the proton beams around the ring, and 384 quadrupole magnets per ring to control the focusing of the beams. Each ring has a further 536 quadrupole, 1608 sextupole, 784 octupole, and 616 decapole magnets to control and correct instabilities in the beams due to couplings during acceleration and collision. Nominally the LHC is designed to collide proton bunches at ATLAS every 25 nanoseconds with a center-of-mass-energy of 14 TeV, however it is still early in the LHC program and these were not the conditions that the 2012 dataset was taken under. Due to difficulties with the magnet fault protection system the collisions took place at 8 TeV center-of-mass-energy, and because the accelerator and beams are being actively studied a variety of beam configurations were used with bunches separated by 25 to 75 nanoseconds [31].

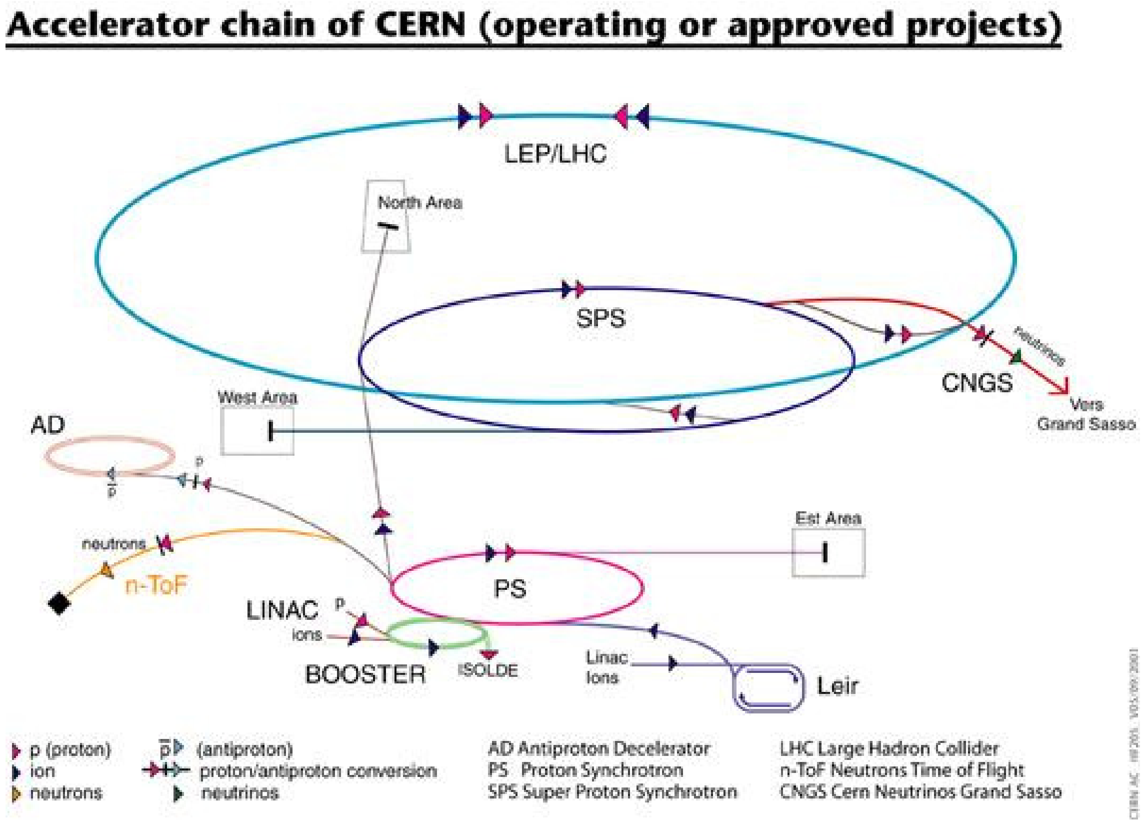

Figure 3.1: Diagram of the CERN accelerator chain [5].

3.2 The ATLAS detector

The ATLAS detector is one of two large general purpose experiments which study collisions produced by the LHC. It is designed to perform a wide variety of searches and measurements by collecting as much information as possible about the products of each collision. ATLAS uses a multilayered design that has become standard for collider experiments and can be seen in Figure 3.2. The innermost portion is called the inner detector which provides fine granularity tracking of charged particles. Moving radially outwards from the interaction point the next detectors are the calorimeters which measure the energy of the particles, and the outermost portion of the detector consists of the muon system which detects and tracks muons traveling through ATLAS. Each of these portions of ATLAS are made up of sub-detector systems designed to work together with the other systems and provide more information than any single technology detector [32].

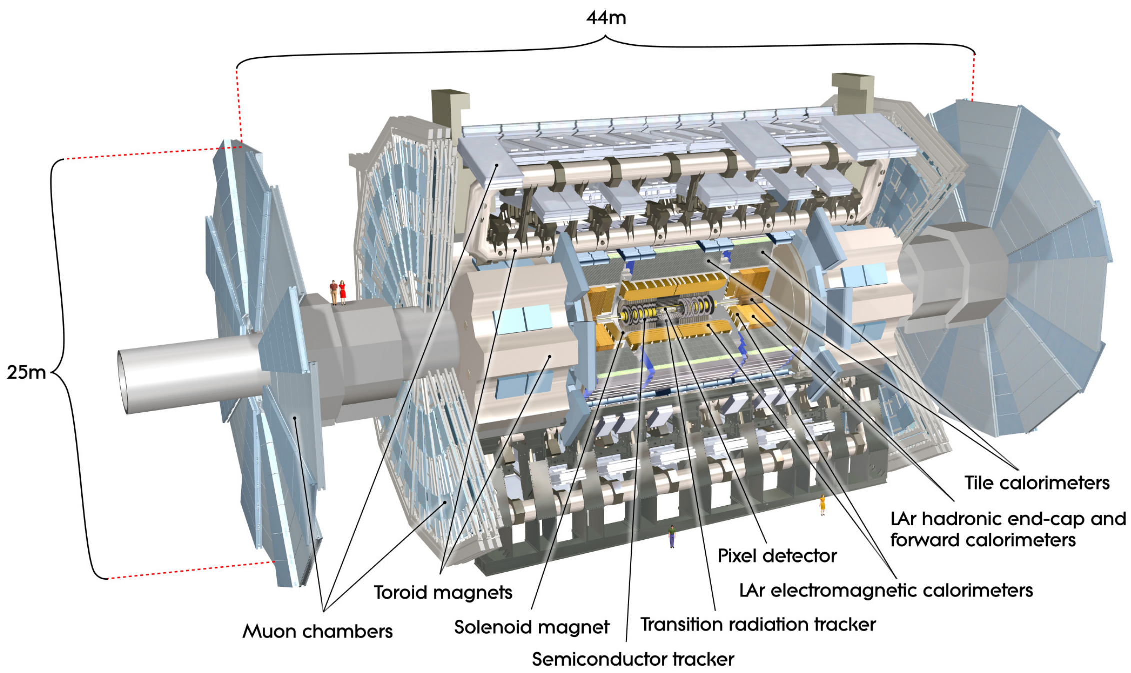

Figure 3.2: Cutaway diagram of the ATLAS detector [6].

3.2.1 Detector geometry

Before detailing each detector system that makes up ATLAS it is useful to discuss the coordinate system used in the experiment. The center of the detector is taken to be the origin and the z-axis extends along the beam line with positive being counterclockwise around the LHC when viewed from above. The x-axis points towards the center of the LHC and the y-axis points vertically upwards. While this forms a complete basis to describe the detector and it is sometimes used, it is not the most common coordinate system. Ignoring gravitational effects all directions transverse to the beams are equivalent and can be described by an angle ϕ taken to be zero along the x-axis and increasing right-handedly with respect to the z-axis. The angle from the beam line is a common parameter for describing decays. However because objects are produced with Lorentz boosts in the z direction ranging from 0 to nearly 1 it is more useful to use a relativistic invariant to describe this angle. The equation for the Lorentz invariant rapidity (y) of a particle in terms of the particle's energy (E) and momentum along the beam line (p_z) is:

$$y = \frac{1}{2} ln \left(\frac{E + p_z}{E - p_z} \right) \tag{3.1}$$

While useful, the rapidity of a particle is dependent on the particle's mass and a different rapidity coordinate system to describe the detector would be necessary for each mass. Almost all particles produced by the LHC have $m << E$ so we can calculate rapidity with $m = 0$ and it is approximately the rapidity for all particles produced by the LHC. This is called the pseudorapidity (η), and is given in terms of the magnitude of a particle's momentum ($|\vec{p}|$) and the particles momentum along the beam line(p_z) in Equation 3.2.

$$\eta = \frac{1}{2} ln \left(\frac{|\vec{p}| + p_z}{|\vec{p}| - p_z} \right) \tag{3.2}$$

Which can be rewritten using the angle from the z-axis (θ) as:

$$\eta = -ln \left(tan \left(\frac{\theta}{2} \right) \right) \tag{3.3}$$

Thus pseudorapidity is a purely geometric quantity, with $\eta = 0$ corresponding to the transverse plane and $|\eta| = \infty$ corresponding to the beamline. In detector parlance regions with small $|\eta|$ (approximately $|\eta| < 2.5$) are called "central" and regions with larger $|\eta|$ are called "forward." An illustration showing the ATLAS geometry is shown in Figure 3.3.

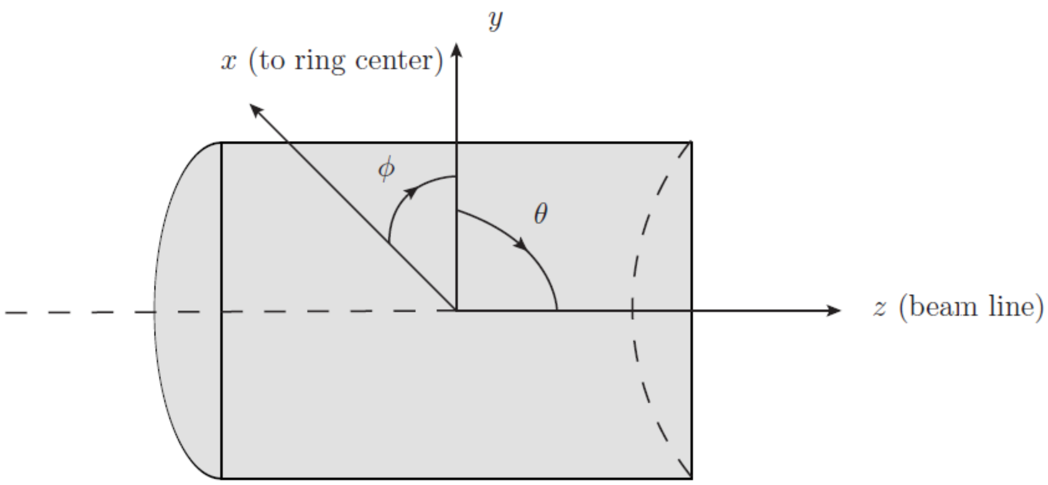

Figure 3.3: Illustration of the ATLAS coordinate system.

3.2.2 Magnet system

The ATLAS detector has three large superconducting magnet systems, the superconducting solenoid, the barrel toroid, and the endcap toroids as shown in Figure 3.4. The purpose of these magnets is to bend the path of charged particles as they propagate through the detector. With careful tracking of a charged particle's path through the magnetic field, it is possible to determine the particle's momentum [32].

The superconducting solenoid is a cylinder 5.3 m long and 2.63 m in diameter. It has 1173 turns of superconducting wire in a single layer along its length with an operating current of 7.6 kA. The inner volume contained by the solenoid has a central magnetic field of 2 T with a peak field of 2.6 T at the superconducting wire. The solenoid is designed to be as thin as possible in order to minimize the interaction between itself and particles from physics events. The particles pass through the 19 cm thick (at most 0.66 radiation lengths) solenoid before they enter the calorimeters [33].

The barrel toroid consists of 8 coils, each of which is a 25.3 m long and 5.35 m wide "racetrack" design. These magnets run the length of ATLAS with their long dimension running parallel to z and their short dimension running radially. They are spaced evenly around the detector with their outer edge at a radius of 10.05 m. Each coil contains 120 turns of superconducting wire with an operating current of 20.5 kA which produces a peak field of 3.9 T [33].

The two endcap toroids complete the ATLAS magnet system. Each endcap contains 8 coils of a racetrack design similar to the barrel toroid, however these coils are 4.5 m in the radial direction and 5 m in the z direction. The endcap coils are offset from the barrel toroid coils by 22.5° in ϕ so that they bisect the angle between adjacent barrel toroid coils. They are aligned in z to share a common outer edge with the barrel toroid, and are placed radially from 0.825 m to 5.35 m. With 116 turns per coil of superconducting wire carrying 20 kA, the endcap toroids produce a peak field of 4.1 T [33].

3.2.3 Inner detector

The ATLAS inner detector is designed to provide excellent tracking information for charged particles with $|\eta| < 2.5$ and is comprised of three concentric subsystems as shown in Figure 3.5. The silicon pixel detector is nearest the beamline and provides the most precise position information with 97 million channels across three layers in the barrel region and with 43 million channels across five disk layers at both ends. Moving radially outwards from

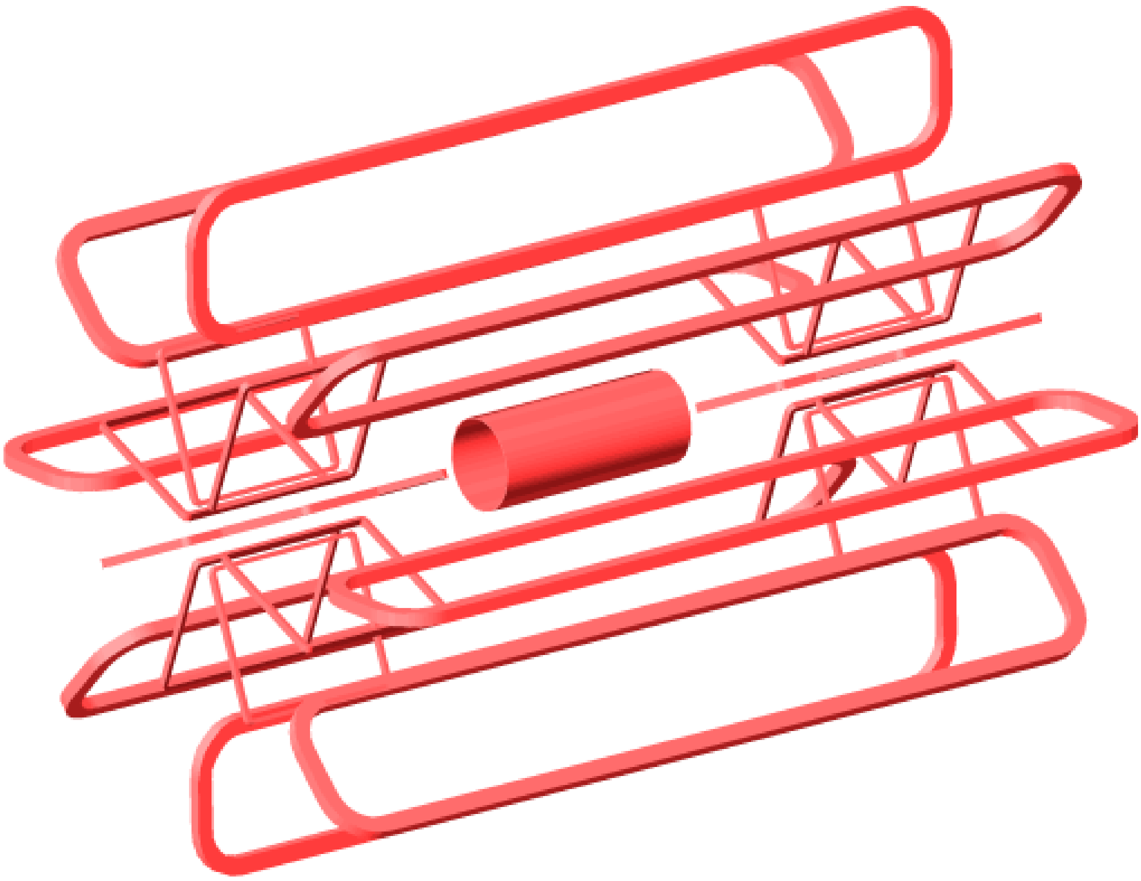

Figure 3.4: Illustration of the ATLAS magnet system, showing the barrel solenoid, barrel toroid, and endcap toroid coils [7].

the beamline the next subsystem is the semiconductor tracker (SCT) which uses eight layers of thin silicon microstrip sensors in the barrel and 44 sensor layers in each endcap, with alternating layers at a 40 mrad angle to each other to allow full determination of position. The final subsystem of the inner detector is the transition radiation tracker (TRT) which is a straw tube system consisting of a barrel section containing axial straws and 18 radial straw wheel segments in each endcap, designed so that most particles will transverse 36 detecting straws [32].

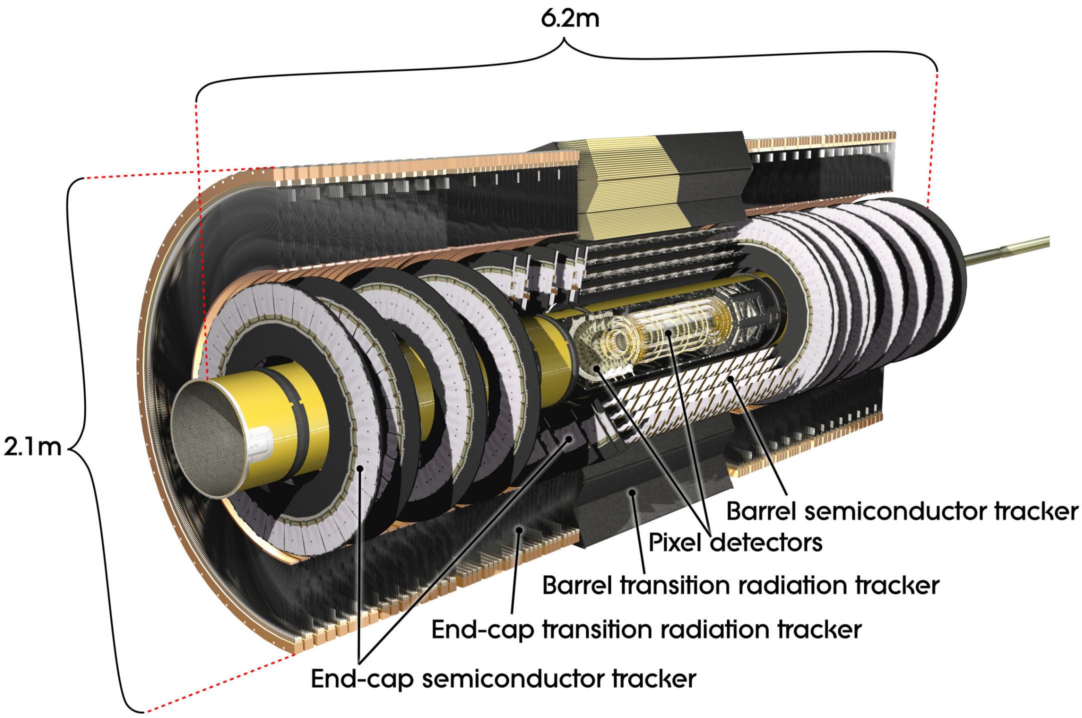

Figure 3.5: Cutaway diagram of the ATLAS inner detector [8].

3.2.3.1 Pixel detector

The pixel detector has the highest granularity and offers the best position and tracking information of charged particles in ATLAS. The system contains three barrel layers with three transverse disk layers at each end. The barrel layers are all 801 mm long, with the innermost layer located at a mean radius of 50.5 mm, the middle layer at 88.5 mm, and the outermost layer at 122.5 mm. The disk layers are all identical annuli with an inner radius of 89 mm and outer radius of 150 mm. These disks are placed at a mean $|z|$ of 495 mm, 580 mm, and 650 mm. This gives the pixel detector a total detecting area of 1.7 m^2 and coverage of $|\eta| \leq 2.5$ [32] [34].

The active medium in the detector is silicon sensor cells 50 μm $\times$ 400 μm in size. In the barrel layers the long dimension is in the z direction and in the disk layers the long dimension is radial. These sensor cells are bump bonded to readout chips with each chip reading an 18 $\times$ 160 cell array. The signal from each cell is amplified and compared to a programmable threshold on each chip. If the signal exceeds the threshold the location is stored in a buffer on the chip to be read out via optical link in the case of a level-1 trigger acceptance, as detailed in Section 3.2.6 [32, 34].

3.2.3.2 Semiconductor tracker

While the pixel detector provides the highest resolution for tracking particles, the technology is not cost-effective to use to cover the larger areas corresponding to larger radii. The next subdetector is the semiconductor tracker (SCT) with four cylinders at radii of 299 mm, 371 mm, 443 mm, and 514 mm and nine disks at both endcaps with mean $|z|$ of 853.8 mm - 2720.2 mm. Each cylinder is 1492 mm long and contains two layers of silicon microstrip sensors at a 40 mrad angle to each other. The microstrip sensors are each 63.6 mm wide and 64 mm long rectangles divided into 768 microstrips each 16 μm wide [35]. The endcap disks have a more complicated geometry with each disk containing 1-3 “rings” of sensor modules depending on position. Each endcap module has two layers of microstrip silicon sensors at a 40 mrad angle to each other similar to the barrel modules. However, unlike the barrel modules, the endcap microstrip sensors are tapered to form trapezoidal segments rather than rectangular. This tapering also causes variable microstrip widths of 16 μm - 20 μm. Each module for both the endcap and barrel regions has four silicon sensors (two per layer) attached to central logic circuits which amplify the signals from each microstrip and compare them to a programable threshold. Similar to the pixel detector, the channels with signals exceeding the threshold are stored in a buffer to be read out if the event is accepted by the level-1 trigger system [32, 35, 36].

3.2.3.3 Transition radiation tracker

The final subdetector of the inner detector is the TRT. While both the pixel detector and SCT use variations of silicon detector technology, the TRT uses a modification of drift tube technology to detect particles. The TRT is divided into one barrel and two endcap sections. The barrel section consists of 52,544 straw tubes arranged in 73 layers parallel to the beam axis. Each straw tube is a drift tube 1441 mm long and 4 mm in diameter and contains a 70% Xe, 27% CO_2 and 3% O_2 gas mixture. Each straw tube also contains a central 31 μm diameter gold-plated W-Re wire which is held at a potential of -1.53 kV relative to the straw tube wall [37].

The endcaps are each made up of 122,880 straw tubes arranged radially in 160 layers. These straw tubes are identical to those used in the barrel except that they are each 370 mm long. These endcap straw tubes are bundled into modules called wheels of 8 layers each, and the wheels are distributed with 848 mm $\leq |z| \leq$ 2710 mm to give nearly uniform coverage in η [38]. Overall the barrel covers $|\eta| < 1.0$ and the endcaps cover $1.0 < |\eta| < 2.0$ with most particles traversing a total of 30 straw tubes.

As a charged particle traverses each straw it causes primary ionization within the gas, which undergoes avalanche multiplication as it accumulates toward the wire giving an amplification factor of 2.5×10^4 with the operating gas mixture and voltage. The unique feature of the ATLAS TRT is that surrounding each straw tube is a layer of transition radiation (TR) material. The TR material is made up of many layers of polypropylene and polyethylene, and is designed to maximize the production of transition radiation produced by charged particles traversing the boundary between the two materials with different dielectric constants. The transition radiation produced in the TR material is generally a soft x-ray photon which is absorbed by the xenon in the straw tubes, ionizing the xenon and producing an energy cascade much larger than a typical ionizing particle does when traversing a straw tube. This is particularly useful because electrons and charged pions are difficult to discriminate between, however the likelihood of transition radiation occuring is proportional to $\gamma = E/m$ and is thus much more likely for electrons due to their lower mass. The TRT readout electronics have two different thresholds: a low threshold designed to detect ionization tracks, and a high threshold designed to detect transition radiation. By using the number of high threshold occurrences along a track, an additional rejection factor for pions of 50-100 is achieved depending on the electron quality definition as described in Section 4.1 [32, 39].

3.2.4 Calorimeters

Having measured the positions of particles as precisely as possible in the inner detector, the next detector systems particles will encounter are designed to measure their energy. The electromagnetic (EM) calorimeter is nearest the beamline covering $|\eta| < 3.2$ and uses liquid argon (LAr) technology with lead absorber plates in a distinctive accordion pattern. The hadronic calorimeter resides around the EM calorimeter, using scintillating tiles with iron absorbers in the barrel region of $|\eta| < 1.7$ and using LAr technology with copper and tungsten absorbers in the $1.5 < |\eta| < 3.2$ and $3.1 < |\eta| < 4.9$ regions respectively. The layout of these systems can be seen in Figure 3.6. It is important that the calorimeter system provides the best containment of particles possible while maintaining good energy resolution so that the total energy of events can be determined [32].

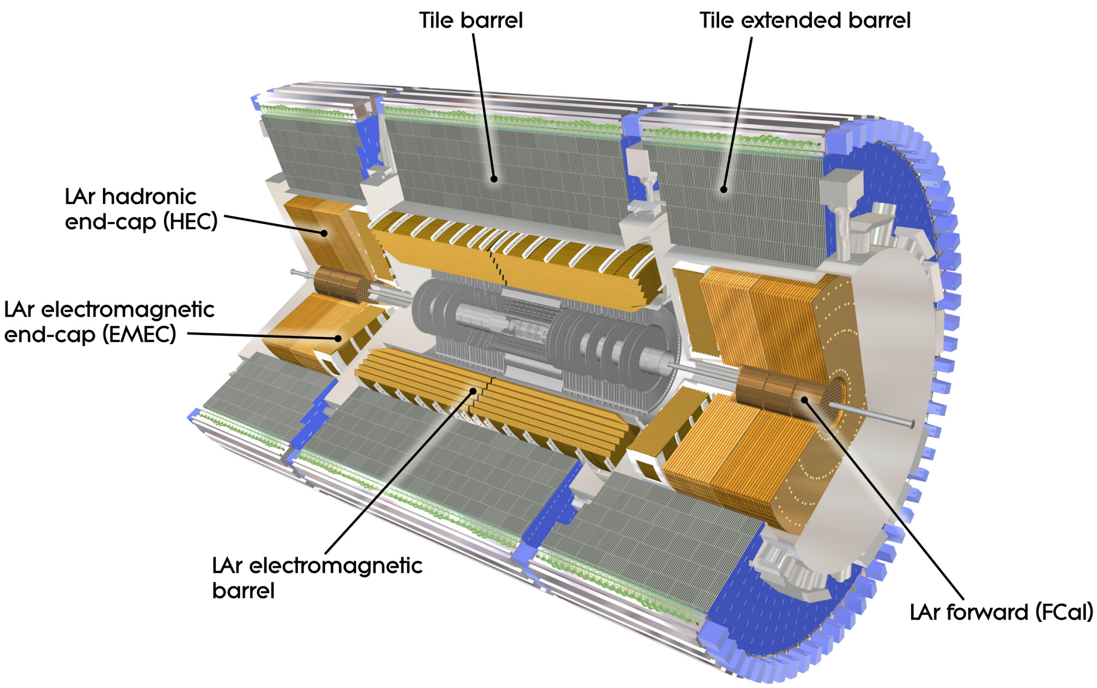

Figure 3.6: Cutaway diagram of the ATLAS calorimeter systems [9].

3.2.4.1 Electromagnetic Calorimeter

The ATLAS EM calorimeter is divided into a barrel section, a presampler, and two endcap sections. The barrel calorimeter is made up of two half barrels which surround the superconducting solenoid and covers the range $|\eta| < 1.475$ with one half barrel covering $\eta > 0$ and the other half barrel covering $\eta < 0$. Each half barrel is a cylinder 3.2 m long and has a 2.8 m inner radius and 4 m outer radius. There are 1024 accordion-shaped absorber plates arrayed radially in each half barrel with the oscillations increasing in amplitude as the radius increases to provide uniform density in ϕ. The absorbers are 1.53 mm thick lead for $|\eta| < 0.8$ and 1.13 mm thick lead for $0.8 < |\eta| < 1.475$ with 0.2 mm thick stainless steel sheets glued to each side to provide structural support. Centered between consecutive absorbers is a readout electrode held at 2 kV relative to the absorber with the 2 mm gap between the electrode and absorber filled with liquid argon. Electrically charged incident particles will shower via Bremsstrahlung in the absorber and this shower will exit the thin absorber layer and enter the liquid argon. The shower ionizes the liquid argon and this ionization is collected at the electrode where it is amplified and read out at both the inner and outer edges of the calorimeter [40].

The presampler is a 22 mm thick detector covering the interior of the barrel calorimeter. It is similar to the barrel detector in that it uses liquid argon with 1.9-2.0 mm gaps between electrodes, but has no absorbers. The purpose of the presampler is to measure showers produced by interactions with the material between the interaction point and the EM calorimeter and improve the energy resolution of the EM calorimeter [41].

The endcap sections are each a detector wheel 630 mm thick with a 330 mm inner radius and 2098 mm outer radius which covers $1.375 < |\eta| < 3.2$. Each wheel is further divided into an inner wheel and an outer wheel by a 3 mm gap located at $|\eta| = 2.5$. The endcaps have a design similar to the barrel calorimeter, with accordion-shaped absorber plates placed radially and readout electrodes interleaved. Each outer wheel contains 768 absorbers of 1.7 mm thick lead, while the inner wheels each have 256 absorbers of 2.2 mm thick lead. The endcap sections also have an 11 mm thick presampler of similar design to that used in the barrel section [32, 42].

3.2.4.2 Hadronic Calorimeter

The hadronic calorimeter makes up the remainder of the ATLAS calorimeter system and is comprised of four sub-systems; the tile barrel calorimeter and tile extended barrel calorimeter are both based on using iron absorber plates with plastic scintillator tiles interspersed, while the hadronic endcap calorimeter and the forward calorimeter are both based on LAr technology similar to the EM calorimeter. The tile barrel calorimeter has an inner radius of 1144 mm and an outer radius of 2115 mm with a length of 5640 mm. The tile barrel calorimeter consists of 64 modules, each of which is a radial slice of the detector. Each module consists of 64 steel plates that are each 5 mm thick and run the radial length of the module. Between consecutive full length plates there are 11 alternating layers of scintillating plastic tiles and steel spacing tiles which are 4 mm thick. These layers progressively increase in length from the inner radius to the outer radius in order to provide high precision measurements while maintaining the necessary depth of interaction lengths to contain very energetic jets. A 1.5 mm gap along both edges of each alternating layer contains a wavelength shifting fiber which carries the scintillation light to photomultiplier tubes located along the outer radius of the modules where the signals are amplified, digitized and processed by readout electronics. The extended barrel calorimeter consists of two sections, one at each end of the tile barrel calorimeter. Each of these sections is 2900 mm long but otherwise follows the same general design as the tile barrel calorimeter with minor modifications to 12 of the 64 modules in each extended barrel calorimeter to accommodate necessary structural supports for the LAr cryostat. A gap region exists between the tile barrel calorimeter and the extended barrel calorimeter on each side. This gap is necessary to provide services to the LAr calorimeters and the inner detector, and while approximately 750 mm wide it is adjusted as needed to accomodate these necessary services. The gap region contains the intermediate tile calorimeter which consists of an irregular arrangement of absorber and scintilator tiles used to estimate the energy lost in the dead material of the gap region. In total the tile barrel calorimeter covers the $|\eta| < 1.0$ region while the extended barrel calorimeter covers $0.8 < |\eta| < 1.7$ and the intermediate tile calorimeter covers $0.8 < |\eta| < 1.0$ [43].

The hadronic endcap calorimeter consists of two wheels located outside of the electromegnetic endcap calorimeters at both ends of the detector, for a total of four wheels. Each of these wheels is further made up of 32 identical wedge-shaped modules. The front wheel on each side starts at a $|z|$ of 4,277 mm and is 816.5 mm in length. The rear wheels start at a $|z|$ of 5134 mm with a length of 961 mm, leaving a 2 mm gap between the wheels. Each front wheel module contains 25 parallel copper plates which are each 25 mm thick and are evenly spaced in z and arrayed transverse to the beamline. The rear wheel modules each contain 17 parallel copper plates which are 50 mm thick and are also evenly spaced in z and arrayed transverse to the beamline. This means that all of the plates are separated by 8.5 mm gaps which are filled with liquid argon. Three electrodes are evenly spaced in each gap with the outer two electrodes held at 2000 V and the central electrode providing the signal for amplification and processing. All of the plates have an outer radius of 2090 mm and the first 9 plates of the front wheels have an inner radius of 372 mm while the remaining plates all have an inner radius of 475 mm, providing coverage in the region $1.5 < |\eta| < 3.2$ [44].

The final sub-system of the ATLAS hadronic calorimeter is the forward calorimeter. This system covers the region $3.1 < |\eta| < 4.9$ and resides entirely inside the 475 mm inner radius of the hadronic endcap calorimeter. This region has an extremely harsh environment with very high radiation densities so many design compromises were necessary to ensure the forward calorimeter could survive and operate in this environment. The forward calorimeter is composed of three sections at each end of the detector. These sections are cylindrical and are arranged coaxially along the length of the beam pipe as seen in Figure 3.6. Each section is made of an absorber material with holes along its length in a honeycomb pattern. Each of these holes contains a thin-walled electrode tube and an electrode rod of slightly smaller radius. The small gap between the electrode rod and tube is filled with liquid argon and the electrode rod is held at 250 V relative to the electrode tube. In the section on either side of the detector which is nearest the interaction point the absorber and the electrode rod are both made of copper. In the remaining sections the absorber and electrode rods are made of tungsten. These materials were chosen due to their densities as well as their thermal properties, ability to be produced to the necessary specifications, and hadronic shower sizes. In all of the modules the electrode tube is made of copper and the electrical signal is read out from each absorber rod for amplification and processing. The liquid argon gaps are smaller than is common in LAr detectors, being 269 μm, 376 μm, and 508 μm in the three sections at each end of the detector and increasing with the distance from the interaction point. This is necessary to prevent charge accumulation in the liquid argon which would degrade performance and is caused by the high radiation density of the region, which decreases with distance from the interaction point. The overall layout of the segments is approximately projective from the interaction point, with the inner radius of the segments increasing proportional to $|z|$, the electrode spacing increasing from 7.50 mm to 9.00 mm across the three segments, and the number of electrodes decreasing from 12,260 tubes in each module nearest the interaction point to 8,224 electrodes in each module furthest from the interation point [45, 46].

3.2.5 Muon Spectrometer

The ATLAS Muon Spectrometer (MS) is the outermost of the ATLAS detector systems and accounts for a majority of the detector's volume. The purpose of this system is to detect muons as they traverse the ATLAS detector and make precision position measurements at three different detector layers to calculate the momentum of each muon based on the curvature of the muon's trajectory as it travels through the ATLAS magnetic field. To accomplish this goal the muon spectrometer has four subsystems which employ differing detector technologies as needed in the various regions of the ATLAS detector. Monitored Drift Tubes (MDTs) and Cathode Strip Chambers (CSCs) provide high precision tracking information over the large area of the muon spectrometer in three concentric layers, called stations. The MDT system uses gas drift tube technology and covers the region $|\eta| < 2.7$, while the CSC system uses multiwire proportional chambers with a cathode strip readout and covers $2.0 < |\eta| < 2.7$. Both the MDT and CSC systems have long response times and are not capable of being used in the level-1 trigger system as described in Section 3.2.6, so two additional muon spectrometer systems are employed for the initial detection of muons. The Resistive Plate Chamber (RPC) covers the region $|\eta| < 1.05$ using resistive plate capacitors which locally discharge when their internal gas is ionized. The Thin Gap Chamber (TGC) system covers $1.05 < |\eta| < 2.4$ using multiwire proportional chambers with a smaller geometry than the CSC system [47]. The overall layout of these systems is shown in Figure 3.7.

3.2.5.1 Monitored drift tubes

The monitored drift tube (MDT) chambers provide the majority of the precision muon tracking capability in ATLAS. MDT modules are arranged into barrel and end-cap regions, with the barrel composed of three concentric cylinders with radii of 5, 7.5, and 10 m with

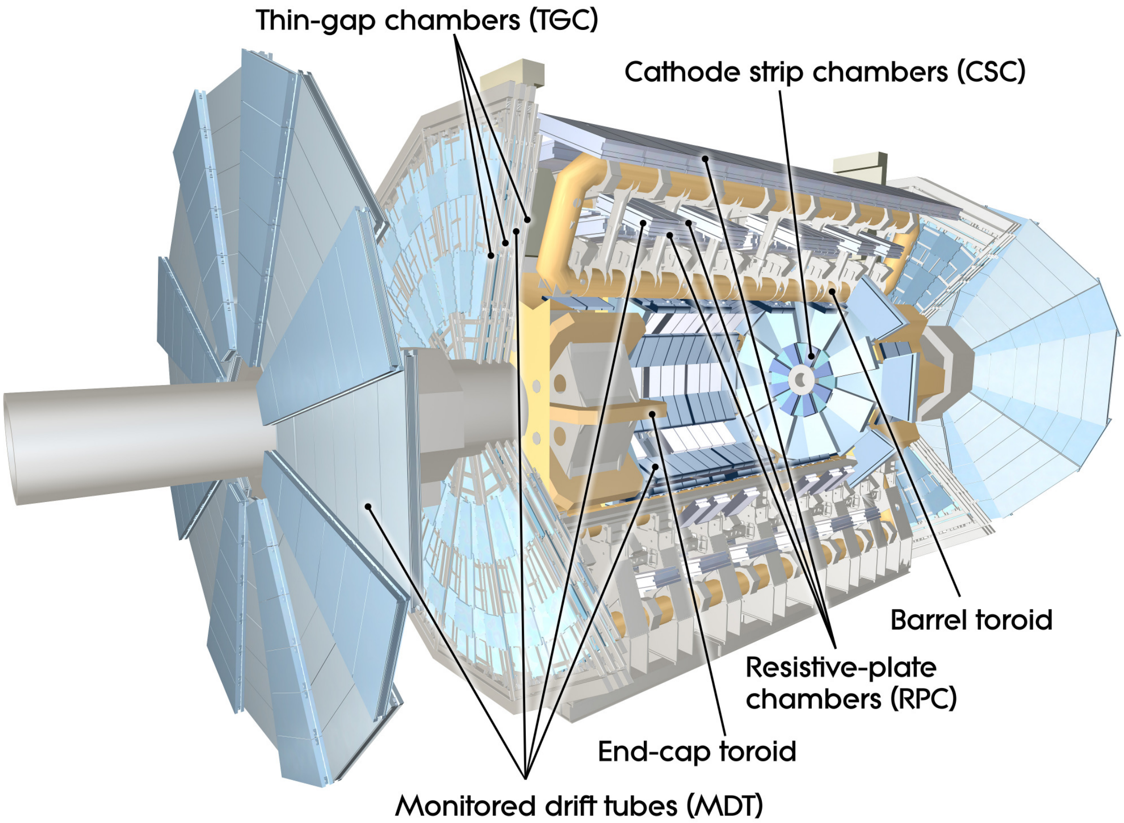

Figure 3.7: Cutaway diagram of the ATLAS muon spectrometer and toroid magnet systems [10].

coverage of $|\eta| < 1.0$ and the endcap regions containing four disks each at $|z|$ of 7, 10, 14, 22 m respectively and covering the range $1.0 < |\eta| < 2.7$. Each chamber is composed of two sets of drift tube multilayers on either side of a rigid support structure which is 150 mm thick. The multilayers in MDT chambers in the stations nearest the interaction point have four layers of drift tubes while all other MDT chamber multilayers have three layers of drift tubes. Each drift tube is 30 mm in diameter and is filled with a 91% Ar, 4% N_2, 5% CH_4 gas mixture. Each tube is read out from a central 50 μm tungsten wire. The wire is held at 3,270 V and gives a spacial resolution of 80 μm with a maximum drift time of approximately 500 ns. Because of this long drift time it is necessary to correlate the signals from the MDT system with corresponding signals in the RPC and TGC systems which provide much more prompt results in order to determine which bunch crossing the MDT signals originated from [47].

3.2.5.2 Cathode strip chambers

The cathode strip chambers (CSCs) are multiwire proportional chambers used for precision muon position measurements in the region of highest radiation density, $2.0 < |\eta| < 2.7$ in the station nearest to the interaction point. Similar to the MDT, the CSC consists of two multilayers with each multilayer containing four monolayers. Each monolayer is a 5.08 mm gas gap containing a 30% Ar, 50% CO_2 and 20% CF_4 gas mixture. In the center of each gas gap is a plane of parallel anode wires. The anode wires are 30 μm diameter tungsten wires separated by 2.54 mm and held at 2,600 V. The walls forming the gap are copper-clad and etched to form thin cathode strips. The cathode strips on one of the walls run orthogonal to the anode wires and provide the precision coordinate measurement, while the cathode strips on the other wall are coarser and run parallel to the anode wires to provide the transverse coordinate measurement. For the precision strips it is only necessary to read out every third strip in order to exceed the resolution of the MDT by using charge interpolation between the strips, and these read-out strips are separated by 5.08 mm. The final resolution in the bending direction is 60 μm for a monolayer [47].

3.2.5.3 Resistive plate chambers

The resistive plate chambers (RPCs) are designed to complement the MDT system in the barrel region ($|\eta| < 1.05$). Each RPC chamber is a simple design; two resistive plates form a capacitor and are held at 8,900 V with a 2 mm gap filled with 97% $C_2H_2F_4$ and 3% C_4H_{10}. An incident muon will ionize the gas and cause a local discharge of the capacitor. This discharge is read out via capacitative coupling by metal strips running in orthogonal directions on both sides of the resistive capacitor. The RPC chambers are placed two thick at each of three stations. The two middle stations are directly inside and outside of the middle MDT barrel station, and the far station is directly inside of the outer MDT barrel station. This system provides prompt muon detection with a delay of less than 10 ns and a timing uncertainty of 1.5 ns. The signal position is known to within a resolution of 1 cm which is used by the level-1 trigger system and provides a complementary position measurement to the MDT [47].

3.2.5.4 Thin gap chambers

The thin gap chambers (TGCs) fill a role similar to the RPC, prompt detection of muons for use in level-1 triggering and a complementary position measurement to the MDT, but in the endcap region ($1.05 < |\eta| < 2.4$). The TGCs are based on multiwire proportional chamber technology similar to the CSCs but with a smaller geometry and faster readout time. Each TGC gas gap is 2.8 mm wide and is filled with a highly quenching 55% CO_2 and 45% $n - C_5H_{12}$ gas mixture. A central plane of 50 μm tungsten anode wires are spaced 1.8 mm apart and are held at 3,100 V. The signals from these wires are read out with 4 to 20 wires forming an individual readout channel depending on η. Signals are also read out from etched copper strips on one of the walls of each gap to provide a measurement of the azimuthal angle for each track. This configuration gives each gap a position resolution of approximately 9 mm and a time response of 7 ns, which is sufficient for bunch identification and use by the level-1 trigger system. TGC modules are made up of either gas gap doublets or triplets with 20 mm of separation between consecutive gas gaps. The inner wheel at $|z|$ = 7 m of each endcap has a layer of doublet chambers and the middle layer wheel at $|z|$ = 14 m has two layers of doublet chambers and a layer of triplet chambers, giving the total system a depth of nine gaps [47].

3.2.6 Triggering and data acquisition

As described in Section 3.1, proton bunch crossings occur inside the ATLAS detector every 25 ns. With the size and complexity of the ATLAS detector (the average event is 1.3 Mbytes of data [32]) it is not possible to read out and store the detector response for every bunch crossing, thus a trigger and data aquisition system (TDAQ) has been implemented to identify and record the most interesting events. The trigger system is divided into three levels, each of which takes as input the accepted events of the previous level and reduces the rate of accepted events using increasingly complex algorithms. The level-1 (L1) trigger uses information in localized regions of the calorimeter and muon systems to reduce the accepted event rate from 40 MHz to 75 kHz. The level-2 (L2) trigger uses more precise information, including tracking from the inner detector for the region of interest (RoI) that caused the level-1 acceptance, to further reduce the accepted event rate from 75 kHz to 3.5 kHz. The event filter (EF) is the final trigger level which uses the highest granularity information from the entire detector to further reduce the accepted event rate from 3.5 kHz to the 200 Hz which is saved for analysis.

The level-1 trigger has an event input rate of 40 MHz and a maximum event acceptance rate of 75 kHz with a total latency of 2.0 μs. The 40 MHz input event rate means that no single part of the trigger decision can take more than 25 ns, which is achieved by using a highly parallelized hardware implementation. The electromagnetic liquid-argon calorimeter and hadronic tile calorimeter systems as well as the RPCs and TGCs in the muon spectrometer each have their signals read out to the level-1 trigger system. The calorimeter signals are processed by hardware located in the ATLAS counting room adjacent to the cavern which houses ATLAS, while the muon system signals are processed by hardware located on the ATLAS detector. The level-1 trigger processors each only process their local detector area and operate at a lower granularity than the systems are ultimately capable of. The processors look for energy clusters above a variety of set thresholds depending on the system and region of the detector, with an above threshold area forming a region of interest (RoI). The exception to the local scope of the level-1 trigger system is a special processor which calculates the total transverse energy of each event, as well as the missing transverse energy[2] of each event and compares them to a variety of thresholds. All of the processors send a list of surpassed thresholds to the central trigger processor (CTP) which correlates and counts

[2]To first approximation the net energy in the transverse plane for an event is expected to be zero. A large difference from zero in the vector sum of the measured energies in the transverse plane indicates the existence of an unmeasuerd particle, such as a neutrino or dark matter particle, in the event. The negative of this measured excess energy is called the missing transverse energy ($E_{\mathrm{T}}^{\mathrm{miss}}$). A more detailed definition of the $E_{\mathrm{T}}^{\mathrm{miss}}$ is used in the final event analysis as described in Section 4.4

the multiplicity of surpassed thesholds and determines a level-1 trigger decision for each event based on a programmable trigger menu [48].

The level-2 trigger has an event input rate of 75 kHz from the level-1 trigger and event acceptance rate of 3.5 kHz with a total latency of 10 ms. Unlike the level-1 trigger, the level-2 trigger system uses all of the ATLAS detector systems and is implemented in software. For each event, the signals for all of the detector systems are read out in each of the RoIs identified by the level-1 trigger system to a node in the level-2 server farm. Depending on the exact level-1 trigger conditions for the event, a series of software algorithms are then applied to the event in order to refine the measurements. A final level-2 decision is reached based on the outcome of these algorithms [49].

The final level of the trigger system is the event filter. The event filter has an event input rate of 3.5 kHz and a final event acceptance rate of 200 Hz with a latency of 1 s. This trigger level is very similar to the level-2 trigger system however rather than only calculating a trigger decision based on the RoIs, the event filter calculates a decision based on the entire event. Each event accepted by the level-2 system has all of the detector systems read out to a node in the event filter server farm. Based on the complete event information a lengthier and more precise calibration is performed, and based on this more detailed information an event filter decision is calculated. Events which are accepted by the event filter are read out from ATLAS to be saved at a dedicated computing facility for storage and analysis [48].

Chapter 4

Object Definitions

In order to perform a search for $W' \to t\bar{b}$ each event needs to be reconstructed from the raw ATLAS data. These raw data are a collection of energy deposits in the calorimeters and tracking hits from the inner detector and muon spectrometer which need to be refined into a more useable form. The raw data are reconstructed into analysis objects which generally correspond to the particles that passed through the detector. Different types of particles will interact with the various detector systems in different ways, leaving distinct signatures as illustrated in Figure 4.1.

- Electrons leave a track in the inner detector and an energy shower in the EM calorimeter.
- Muons leave a track in the inner detector and in the muon spectrometer with minimal energy deposited in the calorimeters.
- Jets leave tracks in the inner detector and energy showers in the EM and hadronic calorimeters. Jets are represented in Figure 4.1 by the proton and neutron.
- Photons do not leave a track in the inner detector and produce only an energy shower in the EM calorimeter.
- Neutrinos do not interact in the detector but their presence can be inferred from an imbalance in the total event momentum in the transverse plane.

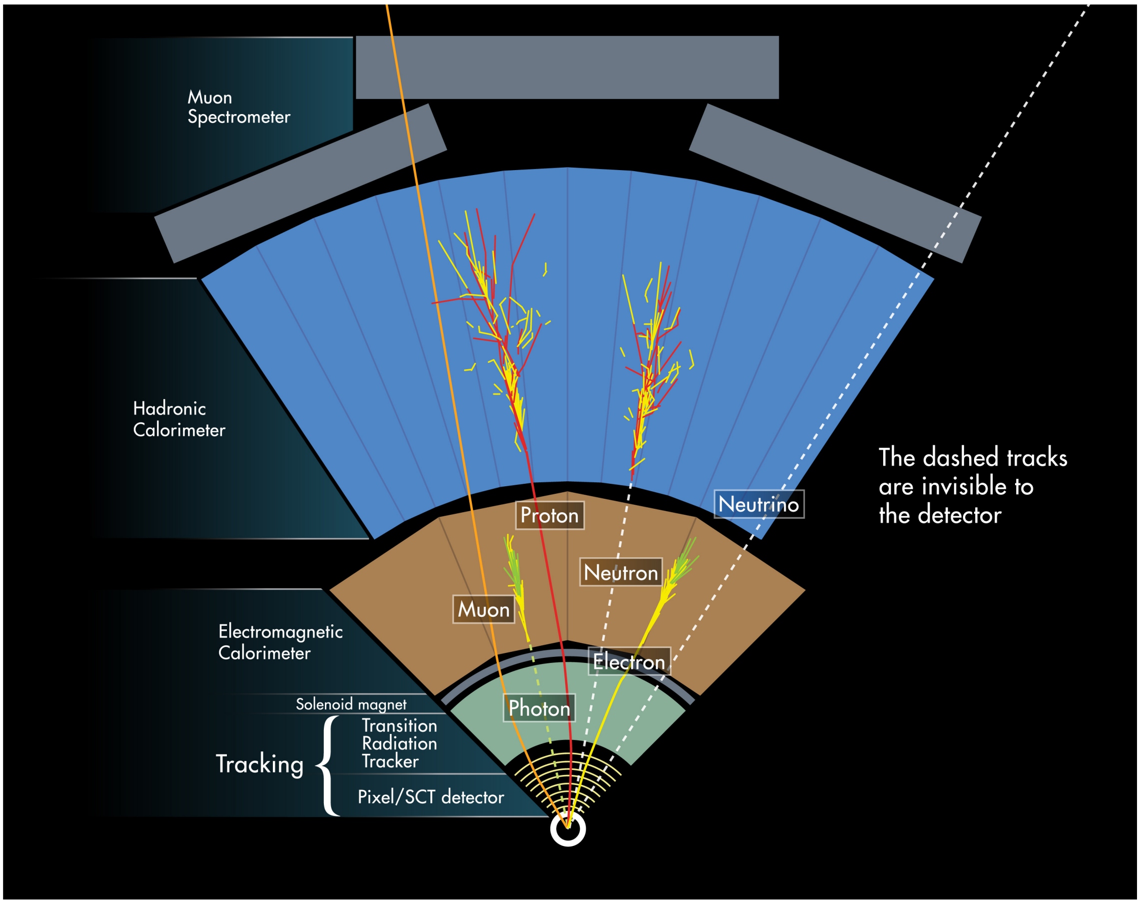

Figure 4.1: Illustration of how different particles interact with the ATLAS detector systems [11].

For the $W' \to t\bar{b}$ analysis the objects of interest are electrons, muons, jets, and the missing transverse energy ($E_{\mathrm{T}}^{\mathrm{miss}}$) corresponding to a neutrino. It is possible for "fake" objects to be created due to detector resolution effects or by other particles interacting with the detector in rare or unexpected ways. For example, jets that deposit all of their energy in the EM calorimeter before reaching the hadronic calorimeter would appear to be electrons while electrons that do not lose all of their energy in the EM calorimeter and "punch-through" to the hadronic calorimeter can appear to be jets. The object definitions are chosen to balance the rejection of fakes with the acceptance of real objects.

4.1 Electron definition

Electrons are a key component of the $W' \to t\bar{b}$ search and their reconstruction uses a complex algorithm to identify them at high efficiency while keeping the fakes rate low. In order to have access to higher efficiency or higher purity samples the electrons are reconstructed with increasingly stringent requirements to form three qualities: loose, medium, and tight. The requirements for the 3 electron qualities are summarized in Table 4.1. The reconstruction starts by performing a sliding window search of the middle layer of the EM calorimeter, where a 3×5 ($\eta \times \phi$) window of calorimeter cells (each 0.025×0.025 in $\eta \times \phi$) is moved about the calorimeter to find the local maxima of energy enclosed. Maxima with an energy above 2.5 GeV are called seed clusters. Seed clusters are then checked against the tracking information, and clusters with a track within $\Delta\eta$ and $\Delta\phi$ requirements determined by the electron quality are considered electron candidates [2].

Electron candidates have their energy recomputed using a 3×7 ($\eta \times \phi$) window of calorimeter cells with corrections applied based on the position and energy and are assigned a four-momentum based on the tracking and corrected energy. A final set of cuts, shown in Table 4.1, is applied to electron candidates based on their quality. For cuts in Table 4.1 without values specified, the cut values are optimized individually in 10 bins of η and 11 bins of cluster transverse energy (E_T), where $E_T = \frac{cluster\ E}{cosh(track\ \eta)}$ [2]. In addition to these requirements the tight electrons are required to pass an enhanced set of cuts. Electron candidates are rejected if they are in the EM calorimeter crack region of $1.37 < |\eta| < 1.52$ because the calorimeter performance is degraded. The E_T is required to be greater than 25 GeV because this analysis is focused on high energy events. Electron candidates are rejected if they are near a jet, defined as having $\Delta R < 0.4$ where $\Delta R = \sqrt{\Delta\eta^2 + \Delta\phi^2}$. The final requirement for tight electrons is that they are isolated in the tracker and calorimeter as defined by cutting on the parameters Ptcone30 and Etcone20 respectively, with both cuts being energy dependent with 90% efficiency. Ptcone30 is the sum of the p_T[1] of all tracks in a cone with half opening angle of 0.3 minus the p_T of the candidate's track. Similarly, Etcone20 is the sum of the E_T in a cone with half opening angle of 0.2 minus the E_T of the cluster.

4.2 Muon definition

Muons are of approximately equal importance to the analysis as electrons, but thankfully they are much easier to identify and reconstruct in ATLAS. As described in Section 3.2.5, the muon spectrometer is the largest ATLAS sub-detector and is dedicated to identifying and measuring muons. Muons are reconstructed with different qualities similar to how electrons

[1] p_T is the momentum in the plane transverse to the beam line. For electrons it is computed from the observed curvature in the particle's track due to the solenoid's magnetic field.

Type	Cut Description
Loose electrons	
Detector acceptance	• $\lvert\eta\rvert < 2.47$
Hadronic leakage	• Ratio of the E_T in the first layer of the hadronic calorimeter to the EM cluster E_T ($\lvert\eta\rvert < 0.8$ *and* $\lvert\eta\rvert > 1.37$) • Ratio of the E_T in all layers of the hadronic calorimeter to the EM cluster E_T ($0.8 < \lvert\eta\rvert < 1.37$)
EM calorimeter middle layer	• Ratio of the 3×7 cell energy to the 7×7 cell energy • Shower width in η
Medium electrons (including Loose cuts)	
EM calorimeter first layer	• Total shower width • Ratio of the difference in the largest and second largest energy deposits to the sum of those energies
Track quality	• Number of hits in the pixel detector (≥ 1) • Sum of hits in the pixel detector and SCT (≥ 7) • Transverse impact parameter (< 5 mm)
Track matching	• $\Delta\eta$ between the track and cluster (< 0.01)
Tight electrons (including Medium cuts)	
Track quality	• Number of hits in the first layer of the pixel detector (≥ 1) • Transverse impact parameter cut (< 1 mm)
Track matching	Ratio of the cluster energy to the track momentum • $\Delta\phi$ between the track and cluster (< 0.02) • $\Delta\eta$ between the track and cluster (< 0.005)
TRT	• Number of hits in the TRT • Ratio of the number of high-threshold hits to the total number of hits
Photon conversion	• Matches to reconstructed photon conversions are rejected

Table 4.1: Definition of variables used for electron identification cuts. For cuts without values specified, the cut values are optimized individually in 10 bins of η and 11 bins of cluster E_T [2].

Type	Cut Description
Muon energy	• $p_T > 25\ GeV$
Detector acceptance	• $0.1 < \|\eta\| < 2.5$
Track quality	• Number of pixel hits + number of crossed dead pixel cells > 0 • Number of SCT hits + number of crossed dead SCT strips ≥ 5 • Number of crossed dead pixel cells + number of crossed dead SCT strips < 3 • For $0.1 < \|\eta\| < 1.9$: number of TRT hits + number of TRT outliers > 5 and $\frac{number\ of\ TRT\ outliers}{nTRT} < 0.9$ • Distance along z from track to primary vertex $< 2\ mm$
Isolation	• $\frac{MiniIso10\_4}{muon\ p_T} < 0.05$ • Muon and all jets with $p_T > 25\ GeV$ have $\Delta R > 0.4$

Table 4.2: Definition of muidcombined muon reconstruction cuts.

are reconstructed. This analysis only uses muons reconstructed with the algorithm called "muidcombined" so only that algorithm is described here. Muidcombined muon candidates are formed by independently reconstructing a track in the muon spectrometer (MS) and inner detector (ID), and if these tracks match within $\Delta R < 0.05$ then a combined track is reconstructed from both systems. Several cuts are detailed in Table 4.2 which ensure that only well-defined tracks that lie in the most sensitive regions of the detector and that are isolated from other activity are included in the analysis. Two new variables are introduced in these cuts, nTRT is the sum of the number of TRT hits and the number of TRT outliers while MiniIso10_4 is the sum of the p_T of all objects inside a cone with half opening angle of 0.1 minus the muon p_T with a maximum of 40 GeV.

4.3 Jet definition

As described in Section 2.1.2.1, bare quarks and gluons undergo hadronization before they can interact with the detector. This forms a multitude of tracks and calorimeter energy deposits spread over an area, which is treated as a single object called a "jet". Being of such a composite nature, jets are complicated objects and there are many different ways to define and reconstruct them.

This analysis uses the $anti-k_t$ algorithm [50] to define and reconstruct jets. The $anti-k_t$ algorithm starts with a list of all objects, in this case the calorimeter cell energies. From this list of objects, a list of all two-object and object-beam distances is computed where the distance between two objects is defined in Equation 4.1, and the distance between each object and the beam as defined in Equation 4.2. If the minimum distance is between two objects then they are merged to form a new object, the original objects are removed from the list and the new combined object is added to the list, then all distances are recalculated. If the minimum distance is between an object and the beam then the object is classified as a jet and removed from the list. This process is repeated recursively until the object list is exhausted. In Equation 4.1 the parameter R is the characteristic size of the jet. Larger values of R produce fewer, wider jets which are more likely to contain products from more than one parton. Conversely smaller values of R produce more, smaller jets that may not contain all of the products of individual partons. For this analysis $R = 0.4$, consistent with other ATLAS top quark analyses.

$$d_{ij} = min(p_{T,i}^{-2}, p_{T,j}^{-2}) \frac{\Delta\eta_{ij}^2 + \Delta\phi_{ij}^2}{R^2} \tag{4.1}$$

$$d_i = p_T^{-2} \tag{4.2}$$

After forming jets with the $anti-k_t$ algorithm a correction is applied to each jet based on the jet's position and p_T to correct for the specific response of each region of the detector.

The corrected jets then have a series of quality cuts applied. Any jets with negative energy are removed as these are unphysical. If any jets are within $\Delta R < 0.2$ of an electron, the jet nearest the electron is removed because it is likely a double counting of the electron as a jet.

4.3.1 Jet b-tagging

Jets that originate from different types of particles often exhibit different kinematics, and by analyzing the kinematics of a given jet it is possible to predict the flavor of the parton that produced the jet. This process is generally referred to as "tagging," with jets that pass the tagging criteria called "tagged" and jets that fail the tagging criteria called "untagged." In this analysis "b-tagging" is employed to sort jets based on how likely they are to have originated from bottom quarks called b-jets. Specifically, the MV1 [51] b-tagging algorithm is used.

MV1 is a neural network analysis[2] of ATLAS b-tagging algorithms SV0, IP3D+SV1, and JetFitterCombNN. SV0, IP3D+SV1, and JetFitterCombNN all use the secondary vertex caused by the bottom quark's relatively long hadronization time, as discussed in Section 2.1.2.1, to distinguish b-jets from other jets. An illustration of a secondary vertex is shown in Figure 4.2. This secondary vertex can be parameterized by its transverse and longitudinal impact parameters (d_0 and z_0) which are the distances between the secondary and primary vertex in the radial or z projection respectively, or the decay length (L_0) which is the distance between the primary and secondary vertex. SV0, IP3D+SV1, and JetFitter-CombNN use varying mixtures of these parameters as well as their significances, which are

[2]Neural network analyses are multivariate classifier functions similar to the boosted decision trees described in Chapter 7. They are described in greater detail in the reference materials [52] [53].

defined as the ratio of the parameter and its uncertainty, to discriminate between b-jets and all other jets [52]. MV1 uses the outputs of these other b-tagging algorithms to produce a single weight that corresponds to how likely a jet is to have originated from a b quark. For this analysis a tagging cut on each jet is placed at the 70% b-tagging efficiency value, which means that 70% of bottom quark initiated jets are expected to pass the cut and be tagged.

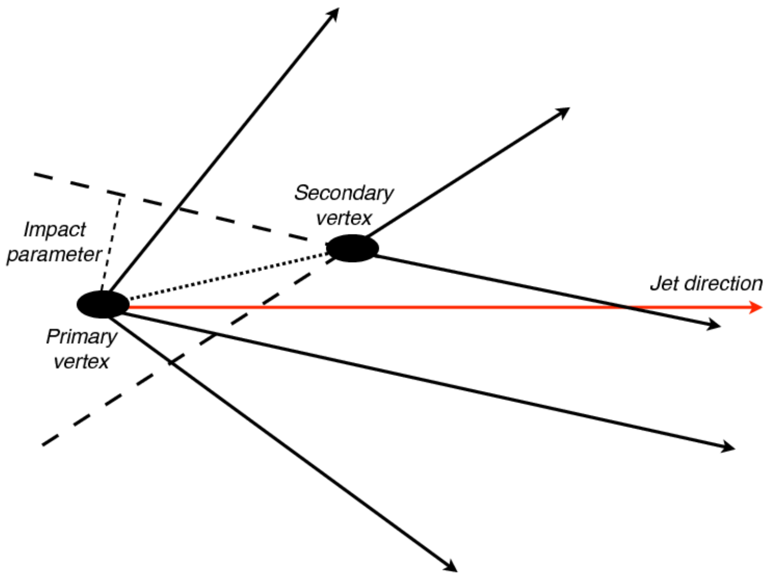

Figure 4.2: Illustration of a displaced secondary vertex caused by a b-jet [12].

It is possible for a jet that did not originate from a bottom quark to be b-tagged by the MV1 algorithm, which is called a “fake tag.” This is primarily due to the finite resolution of the inner detector causing tracks to seem to be displaced from the primary vertex and forming a secondary vertex. The likelihood of a fake tag occuring is dependant on the p_T and η of the jet and has been estimated using a data control region as well as in simulated event samples. The MV1 algorithm operating at 70% b-tagging efficiency has a likelihood of fake tagging a jet which did not originate from a botom quark of approximately 1% to 3% depending on the p_T and η of the jet [54].

4.4 Missing transverse energy definition

With particles colliding nearly head-on along the beam line, the sum of the products' momenta in the transverse plane should be approximately 0. However, neutrinos and some theoretical exotic particles are not expected to interact with the ATLAS detector, causing the measured final state to have an imbalance in the transverse momentum. The negative of this measured imbalance is called the missing transverse energy ($E_{\mathrm{T}}^{\mathrm{miss}}$). Unfortunately $E_{\mathrm{T}}^{\mathrm{miss}}$ is sensitive to any mismeasurement in the detector as well as the possibility of being faked by an interacting particle missed by the detector when traveling through cracks or dead regions. To correct for these different sources, individual calibrations are applied to the $E_{\mathrm{T}}^{\mathrm{miss}}$ from soft jets, hard jets, electrons, muons, and cell-out energy fragments before they are used to compute the $E_{\mathrm{T}}^{\mathrm{miss}}$ according to Equation 4.3.

$$E_{\mathrm{T}}^{\mathrm{miss}} = E_{\mathrm{T}}^{\mathrm{miss,e}} + E_{\mathrm{T}}^{\mathrm{miss},\mu} + E_{\mathrm{T}}^{\mathrm{miss,softjets}} + E_{\mathrm{T}}^{\mathrm{miss,hardjets}} + E_{\mathrm{T}}^{\mathrm{miss,cell-out}} \tag{4.3}$$

Hard jets are jets as defined in Section 4.3 with $p_T > 20\ GeV$. Soft jets are jets as defined in Section 4.3 with $20\ GeV > p_T > 10\ GeV$. Electrons and muons are defined using the definitions in Section 4.1 and Section 4.2 respectively. Cell-out energy fragments are any energy in the calorimeter which is not included in the other objects [55].

Chapter 5

Event selection

Before the final analysis described in Chapter 7 can be performed, an event selection specific to the signal kinematics is applied. This event selection is designed to remove background events while having minimal impact on the signal and defines the control regions used to perform the data-driven background estimates described in Section 6.4. Events are also separated into different analysis channels based on the total number of jets and the number of b-tagged jets in the event and these channels are individually optimized.

5.1 Composite objects

Chapter 4 details how basic analysis objects are reconstructed from the raw detector response, and these basic objects can be combined to reconstruct composite objects. The Feynman diagram in Figure 5.1 shows the $W' \to t\bar{b}$ signal process, with the inital state on the left and the final state on the right, with several intermediate particles in between. These intermediate particles are the W boson, top quark, and ultimately the W' boson and they are what define this channel as unique from any other process with the same final state. These intermediate particles give $W' \to t\bar{b}$ events unique kinematics that distinguish $W' \to t\bar{b}$ from other processes.

Based on Figure 5.1, the ideal analysis channel contains a lepton, $E_{\mathrm{T}}^{\mathrm{miss}}$, and two b-tagged jets. In order to increase the signal acceptance, the common ways for signal events to fail

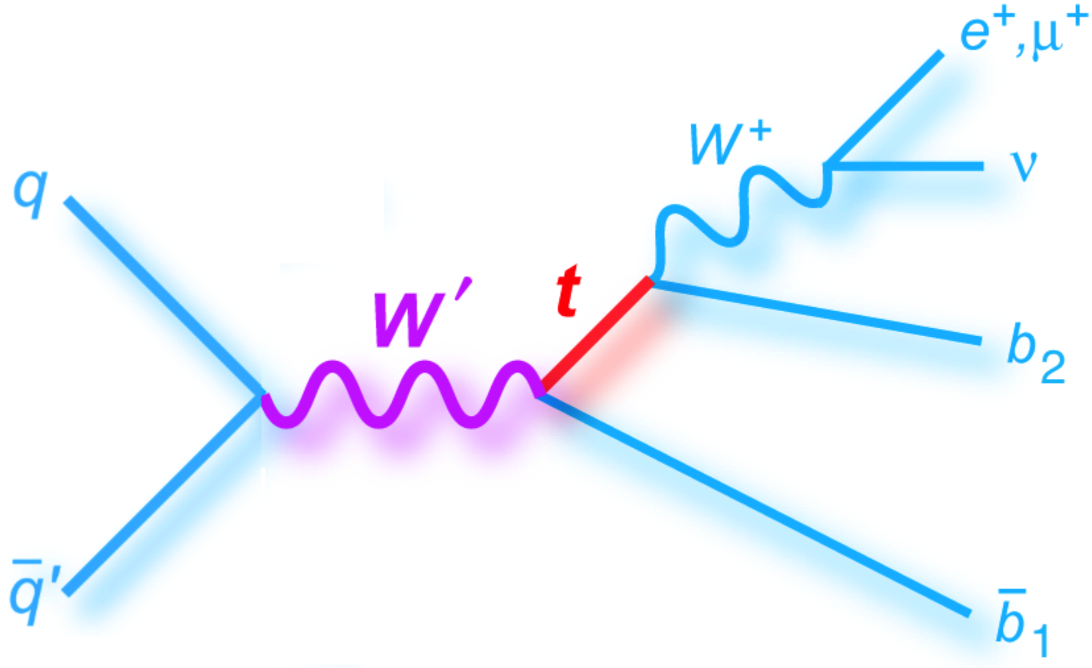

Figure 5.1: Illustration of the $W' \to t\bar{b}$ process.

such a selection are considered. Additional jets can be present in an event due to hard gluon radiation in the initial or final state, so the event selection is expanded to include events with either 2 or 3 jets. Also, the cut on the MV1 b-tagging weight used to define a jet as b-tagged is 70% efficient, thus one of the b-jets could easily fail to be tagged so the event selection is again expanded to include events with either 1 or 2 of the jets being b-tagged. This leads to the event selection detailed in Section 5.3, and four analysis channels are formed based on the total number of jets and the number of b-tagged jets in an event: 2jets 1tag, 3jets 1tag, 2jets 2tag, and 3jets 2tag. The reconstruction of the top quark and W' boson in each event, as detailed in Sections 5.1.2 and 5.1.3, differs depending on which analysis channel the event is in.

5.1.1 W boson and neutrino reconstruction

The W boson in Figure 5.1 is the only intermediate particle decaying entirely to final state objects and its reconstruction is as simple as adding the 4-momenta of the lepton and neutrino together. The complication with this is that the 4-momentum of the neutrino is not known. Section 4.4 describes how the $E_{\mathrm{T}}^{\mathrm{miss}}$ is calculated by assuming that the momentum is balanced in the transverse plane. This technique cannot be used to determine p_z (along the beamline) for the neutrino because there is no reason the interacting partons should have the same momentum along the beam line as each other. Instead the W boson and neutrino are defined simultaneously by requiring that the lepton (only events containing a single lepton will be selected as detailed in Section 5.3) and neutrino combine to form an on-shell W boson with a mass of 80.4 GeV. Both the lepton and neutrino are assumed to be massless and the neutrino's p_T is assumed to be equivalent to the $E_{\mathrm{T}}^{\mathrm{miss}}$. This gives rise to a quadratic equation for the neutrino's p_z, with solutions given by Equation 5.1.

$$p_{z,\nu} = \frac{\mu p_{z,l}}{p_{T,l}^2} \pm \sqrt{\frac{\mu^2 p_{z,l}^2}{p_{T,l}^4} - \frac{E_l^2 p_{T,\nu}^2 - \mu^2}{p_{T,l}^2}} \tag{5.1}$$

Where μ is defined as:

$$\mu = \frac{M_W^2}{2} + cos(\Delta\phi_{l,\nu}) p_{T,\nu} p_{T,l} \tag{5.2}$$

In Equations 5.1 and 5.2, $p_{T,l}$ and $p_{T,\nu}$ are the transverse momenta of the lepton and neutrino respectively,and $p_{z,l}$ and $p_{z,\nu}$ are the z-momenta of the lepton and neutrino. $\Delta\phi_{l,\nu}$ is the difference in ϕ between the lepton and neutrino. There are three possible categories of solutions to Equation 5.1 based on the sign of the discriminant. If the discriminant is positive then there are two real solutions to Equation 5.1 and the solution with the lowest $|p_z|$ is chosen to define the neutrino, thus creating a less energetic final state. This has been measured in other single top analyses to be the correct selection in approximately 70% of single top events which produce two real solutions to Equation 5.1 [56]. If the discriminant is 0 then there is only one p_z solution and the neutrino is uniquely defined. If the discriminant is negative then the solutions for p_z are imaginary. In this case the p_T of the neutrino is rescaled so that the discriminant becomes 0, then the neutrino p_z is uniquely defined and the neutrino p_T is taken to be the rescaled value. This procedure assumes that the $E_{\mathrm{T}}^{\mathrm{miss}}$ is either mismeasured or not entirely caused by a single neutrino, but that the $E_{\mathrm{T}}^{\mathrm{miss}}$ is still the best estimate of the p_T of the neutrino from the W boson's decay.

5.1.2 Top quark reconstruction

While it is possible to reconstruct the top quark from its decay products (see Figure 5.1), there is an ambiguity about which bottom quark jet in an event originated from the top quark decay. The indeterminacy is resolved differently depending on which analysis channel the event belongs to, as defined in Section 5.3.

- If the event contains only 1 b-tagged jet then the invariant mass of each individual jet (not necessarily b-tagged) and the reconstructed W boson is calculated and the combination with a mass closest to the top quark mass of 172.5 GeV forms the reconstructed top quark.

- If the event contains 2 b-tagged jets the mass of the W boson and each individual b-tagged jet is calculated, with the pair producing a mass closest to 172.5 GeV forming the top quark.

5.1.3 W' reconstruction

Similar to how the top quark is reconstructed, the W' boson is reconstructed differently depending on which analysis channel, as defined in Section 5.3, the event falls into.

- For events that contain 2 b-tagged jets the W' boson is reconstructed by combining the reconstructed top quark with the b-tagged jet that was not used to reconstruct the top quark.
- For events that contain 1 b-tagged jet the W' boson is reconstructed by combining the reconstructed top quark with the highest p_T jet not used to reconstruct the top quark, requiring that the b-tagged jet is included in the W' reconstruction. This means that for events where the top quark was reconstructed from a jet which was b-tagged, the jet combined with the top quark to form the reconstructed W' boson is not b-tagged. For events where the top quark was reconstructed from a jet which was not b-tagged, the jet combined with the top quark to form the reconstructed W' boson must be b-tagged. This ensures that the reconstructed W' boson will contain the b-tagged jet in the event.

5.2 Data triggers

In order for an event to be recorded by the ATLAS detector and included in an analysis it must pass the trigger selection described in Section 3.2.6. To search for $W' \rightarrow t\bar{b}$ the ATLAS single lepton triggers are used. The single electron triggers require that electrons either have an $E_T > 24$ GeV and pass medium isolation requirements for the hadronic leakage, shower width in η, and track isolation as described in Section 4.1 or have an $E_T > 60$ GeV without any isolation requirement. The single muon triggers require that muons either have a p_T > 24 GeV and pass medium isolation requirements for the ID track isolation described in Section 4.2 or have a p_T > 36 GeV without any isolation requirement. The complete set of requirements for electrons and muons detailed in Chapter 4 is applied offline, after the data have been recorded. Events must also have been taken during an LHC stable beam period and during a time when all of the ATLAS subsystems were properly operating. The combination of these requirements corresponds to an integrated luminosity of 20.3 fb^{-1}.[1]

5.3 Cut flow

Before performing the multivariate analysis described in Chapter 7, it is useful to apply a set of event selection cuts. These cuts are designed to remove background events with large kinematical differences from the signal samples so that the multivariate analysis can be more focused on discriminating among the hard to classify events. The event selection also defines the separate analysis channels which will undergo individually optimized multivariate analyses. The event selection cuts are as follows:

- Exactly 1 lepton (electron or muon).
- Lepton $p_T > 35$ GeV.
- $E_{\mathrm{T}}^{\mathrm{miss}} > 35$ GeV
- $(m_T(W) + E_{\mathrm{T}}^{\mathrm{miss}}) > 60$ GeV, where $m_T(W)$ is the W boson transverse mass as defined in Equation 5.3.

[1] In high energy physics the likelihood of a process occuring is usually expressed as a cross-section σ in units of barns (b) where 1 b = 10^{-24} cm^2. The integrated luminosity L is a measure of how much data has been collected and has units of inverse barns (b^{-1}) so that the expected number of events for a process is given by $N_{events} = \sigma L$.

- Exactly 2 or 3 jets with $p_T > 35$ GeV.

- Exactly 1 or 2 of the jets must be b-tagged.

- W' boson mass ($m(W')$) > 330 GeV.

$$m_T(W) = \sqrt{2p_{T,l}p_{T,\nu}(1 - cos(\Delta\phi_{l,\nu}))} \tag{5.3}$$

The total number of jets and the number of jets which are b-tagged defines four unique analysis channels which are referred to by the number of jets and b-tagged jets. For example the 2jets 1tag channel contains events with exactly 2 jets of which exactly 1 jet is b-tagged. This produces four separate analysis channels: 2jets 1tag, 2jets 2tag, 3jets 1tag, and 3jets 2tag.

The cuts on the number of leptons, lepton p_T, and $E_{\mathrm{T}}^{\mathrm{miss}}$ are chosen to match the decay channel seen in Figure 5.1 where a single high p_T lepton and large $E_{\mathrm{T}}^{\mathrm{miss}}$ from the W boson decay are expected. The cut on ($m_T(W) + E_{\mathrm{T}}^{\mathrm{miss}}$) is called the triangular cut and is commonly used in analyses to discriminate against the multijets background, which is defined in Section 6.2.6. The cut on $m(W')$ is chosen to define a control region used to perform a data driven normalization of the W+jets background as described in Section 6.4.1. The cut value of 330 GeV was chosen to maximize the size of the control region while keeping the signal contamination to less than 5% for all of the signal samples.

Both of the 1tag channels have significantly larger backgrounds than the 2tag channels so two additional cuts are applied to the 1tag channels only:

- E_T of the leading jet ($E_T(jet1)$) > 140 GeV.

- Transverse energy of the reconstructed top quark ($E_T(Top)$) > 175 GeV.

These cuts are chosen by ranking a list of event kinematics variables by their discrimination power after performing the initial event selection cuts. The discrimination power of each variable is determined by mapping the signal efficiency (ϵ_S) versus the background efficiency (ϵ_B) for successively higher cuts on the variable. The area between the curve this process maps out and the line of $\epsilon_S = \epsilon_B$ is defined to be the discrimination power of the variable, as shown in Figure 5.2. For the two most discriminating variables, $p_T(jet1)$ and $E_T(Top)$, the cut is chosen to be at least 95% efficient for all signal samples.

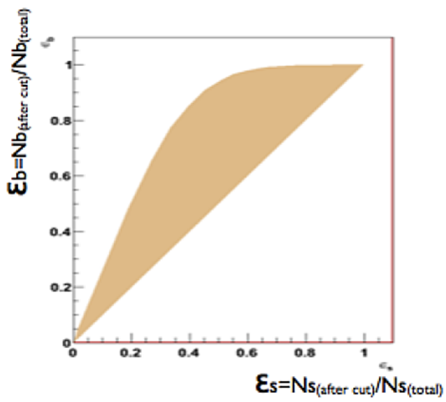

Figure 5.2: Illustration of the discrimination power of a variable, shown as the shaded region.

Chapter 6

Event Simulation

In order to devise and optimize the analysis strategy both signal and background events are modeled. Most of these events are simulated using Monte Carlo (MC) techniques where each event is generated, showered and hadronized, run through a detector simulation, and reconstructed using a variety of software packages. The exceptions to this are the W+jets and multijet backgrounds which are modeled using, either partially or wholely, data driven techniques as described in Sections 6.4.1 and 6.4.2 respectively.

6.1 Signal process

The signal process this analysis is searching for is $W' \to t\bar{b}$. The Feynman diagram for this process is shown in Figure 5.1, and the Lagrangian density that describes the W' boson's production and decay are given in Section 2.13. W'_R and W'_L Monte Carlo samples are produced with one of the BSM couplings g'_R or g'_L set equal to the Standard Model coupling g for $W^{\pm}$ bosons and the other BSM coupling set to zero. Monte Carlo samples are generated at each of 11 W' mass points ranging from 500 GeV to 3,000 GeV in 250 GeV steps for both the W'_R and W'_L processes. This is necessary because the kinematics of the intermediate and final state particles depends on the mass of the W' boson as well as the handedness of its coupling. This mass range was chosen because the searches at the Tevatron excluded W' bosons with a mass less than 500 GeV and this analysis is not expected to be sensitive to

W' bosons with a mass above 3000 GeV.

6.2 Background processes

In order to properly estimate the background for the $W' \to t\bar{b}$ analysis it is necessary to consider all of the processes which are likely to mimic the $W' \to t\bar{b}$ final state shown in Figure 5.1 and which pass the event selection described in Section 5.3. The possibility that leptons or jets can be missed or faked in an event is also taken into account and processes are included that do not match the exact final state of $W' \to t\bar{b}$ but may have events which pass the event selection.

6.2.1 Single top processes

The Standard Model single top processes form a background to $W' \to t\bar{b}$, which is a BSM single top process. Single top processes are defined as containing exactly one top quark, as opposed to a top-antitop quark pair which is described in Section 6.2.2. There are three Standard Model single top processes: the s-channel, t-channel, and Wt-channel. The Feynman diagrams for each of these processes are shown in Figure 6.1. The s-channel process is identical to the $W' \to t\bar{b}$ process this analysis is looking for, except that a $W^{\pm}$ boson takes the place of the W' boson. This means that events will have the same final particles for both the s-channel and W' processes, but the particles in the W' events tend to be at higher energies and have different angular relationships than particles in s-channel events due to the more boosted nature of the intermediate states and the possibly different chirality of the W' and $W^{\pm}$. The t-channel has the same final state as $W' \to t\bar{b}$ with an additional jet. If one of these jets fails to be reconstructed then the t-channel has the same final state particles as

$W' \rightarrow t\bar{b}$, however the kinematics of the particles will be different because of the difference in intermediate states. The Wt-channel can most easily mimic $W' \rightarrow t\bar{b}$ if the additional $W^{\pm}$ boson decays hadronically. In this case the Wt-channel has an additional jet compared to $W' \rightarrow t\bar{b}$, similar to the t-channel. In the case that the additional $W^{\pm}$ boson decays leptonically then there will be an additional lepton and a missing b-jet, and such events are unlikely to pass the event selection. All of the single top processes pass the event selection with a high efficiency relative to the other backgrounds, but because they are rarer processes with smaller cross-sections (see Section 6.3) they are not the dominant backgrounds of the analysis.

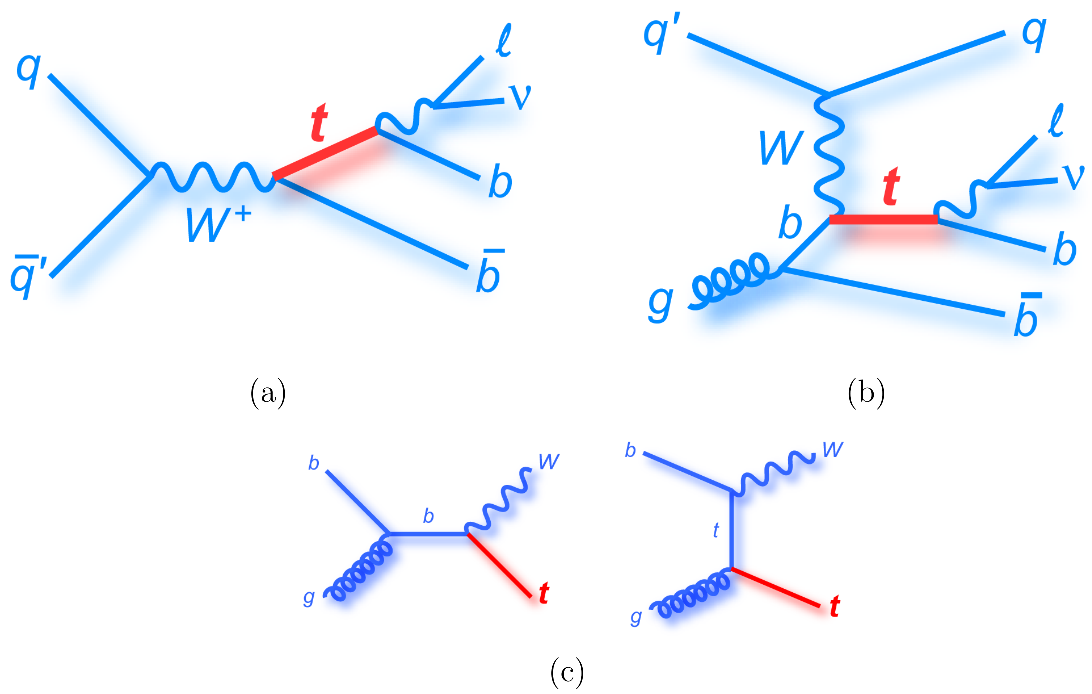

Figure 6.1: Illustration of the (a) s-channel single top process (b) t-channel single top process (c) Wt-channel single top processes.

6.2.2 Top pair production

Top pair production ($t\bar{t}$) is caused by the decay of a highly energetic particle (usually a gluon at the LHC) into a top quark and an antitop quark. A Feynman diagram of the process is shown in Figure 6.2. The resulting final state is the same as for $W' \rightarrow t\bar{b}$ with the addition of the products of an extra $W^{\pm}$ boson decay. This produces an extra lepton and neutino or an extra two jets, which if they are not reconstructed then the event may pass the event selection. This gives $t\bar{t}$ a selection efficiency lower only than single top, but because $t\bar{t}$ has a much larger cross-section (see Section 6.3) it is the dominant background for all of the analysis channels except 2jets 1tag, where it is the second largest background.

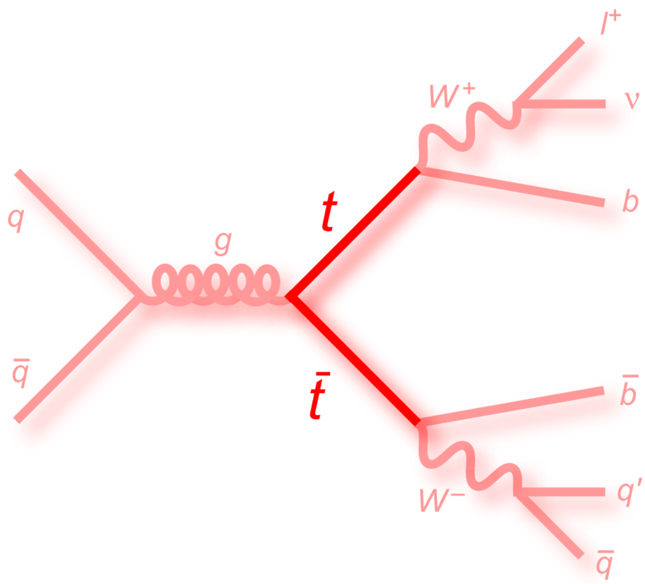

Figure 6.2: Illustration of the $t\bar{t}$ process.

6.2.3 W+jets

The W+jets process is the associated production of a $W^{\pm}$ boson and jets. This includes a variety of more specific sub-processes and these sub-processes can be categorized in many different ways, leading to many different ways to split up W+jets. Because the event selection uses b-tagging it is important to model the response of the W+jets processes to b-tagging as accurately as possible, and the W+jets sample is split into four processes: Wbb is the associated production of a $W^{\pm}$ boson and two bottom quarks, Wcc is the associated production of a $W^{\pm}$ boson and two charm quarks, Wc is the associated production of a $W^{\pm}$ boson and one charm quark and one light flavor (up, down, or strange) quark, and Wlf is the associated production of a $W^{\pm}$ boson and two light flavor quarks. An example Feynman diagram of Wbb is is shown in Figure 6.3. The kinematics of these processes are very different than for $W' \rightarrow t\bar{b}$ and Wlf and Wc events have to fake at least one b-tagged jet in order to pass the event selection, so the overall selection efficiency for these processes is relatively low. However, these processes have a large cross-section (see Section 6.3) and they form the second largest background for all of the analysis channels except 2jets 1tag, where they are the largest background.

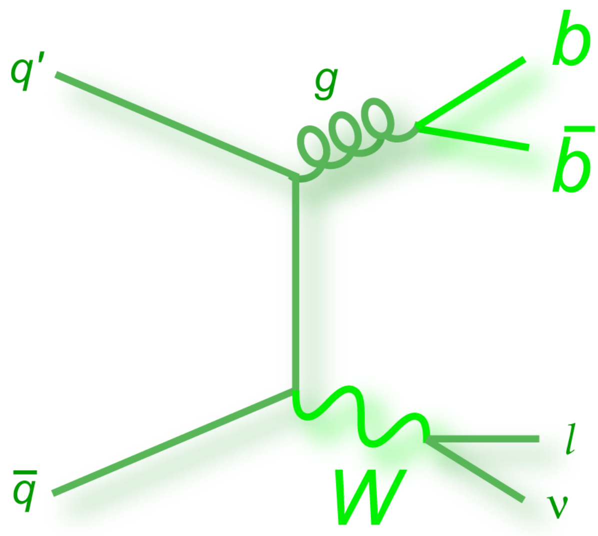

Figure 6.3: Illustration of the Wbb process.

6.2.4 Z+jets

The Z+jets process is the associated production of a Z boson and jets. It is similar to the W+jets process described in Section 6.2.3, but with a Z boson in place of the $W^{\pm}$ boson which leads to an additional lepton in the final state. An example Feynman diagram of Z+jets is shown in Figure 6.4. The Z+jets cross-section is smaller than the W+jets cross-section (see Section 6.3) and the additional lepton in Z+jets events must not be reconstructed for the event to pass the event selection, so the Z+jets background is much smaller for the analysis and it is not broken into sub-processes like W+jets.

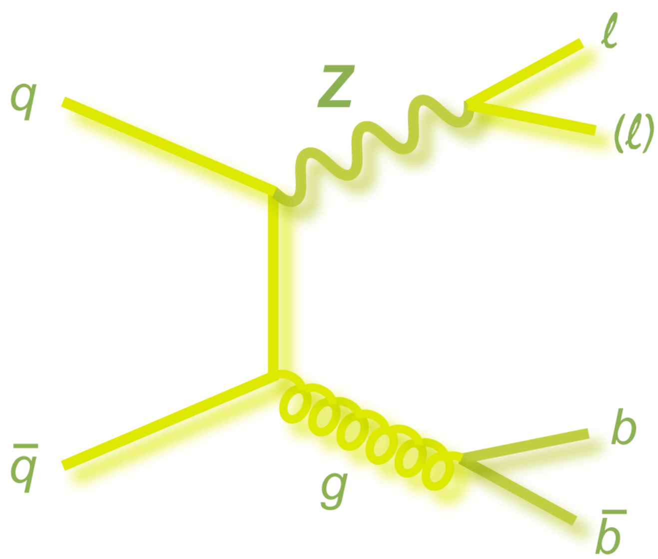

Figure 6.4: Illustration of the Z+jets process.

6.2.5 Diboson processes

The diboson sub-processes are WW, ZZ, and WZ which are the associated production of 2 $W^{\pm}$ bosons, 2 Z bosons, or one $W^{\pm}$ boson and one Z boson respectively. An example Feynman diagram for the WW process is shown in Figure 6.5. These processes are rare with a small total cross-section (see Section 6.3) so they are treated as a single background process. These processes do not involve a top quark decay and have significantly different kinematics than $W' \to t\bar{b}$ and they only rarely produce b-tagged jets, so diboson events are unlikely to pass the event selection. Because of this the diboson background for all of the analysis channels is small.

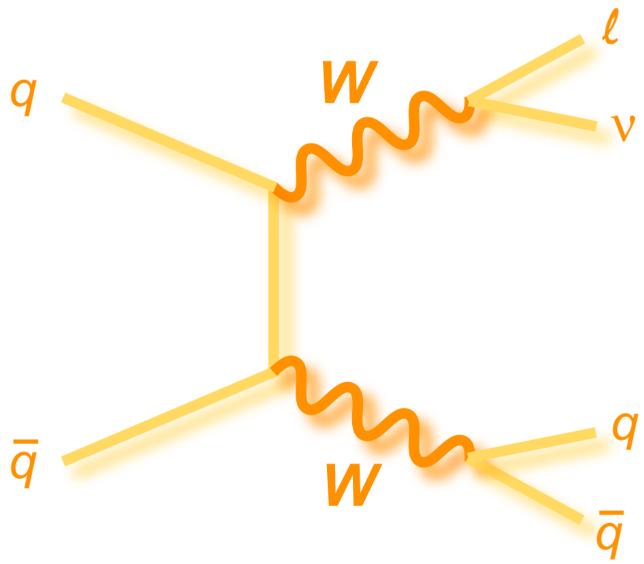

Figure 6.5: Illustration of a diboson process.

6.2.6 Multijets

The multijets background describes events in which the interaction produces two or more jets but no heavy resonant states such as $W^{\pm}$ or Z bosons or top quarks. These events represent the vast majority of collisions that occur at the LHC, but which the trigger system and event selection are designed to reject. Because only the rarest of such events will be included in the analysis it is difficult to accurately simulate this background in Monte Carlo and a data driven technique is used instead, which is described in Section 6.4.2. The resulting estimate is that multijets is a small background for this analysis.

6.3 Monte Carlo simulation

The MC simulation of events is broken down into four stages. Event generation simulates the initial physics event and its decay. Showering and hadronization simulate the formation of jets from any bare quarks or gluons in the generated events. Detector simulation models the interaction of the physics event with the ATLAS detector using a GEANT4 [57] simulation of the ATLAS detector, resulting in a detector response for the event. The final step is event reconstruction where the same algorithms used to analyze data events are applied to the simulated detector responses to build analysis objects.

There are a plethora of software packages available to perform MC simulation of events, and these packages make a variety of different assumptions and simplifications of the physics they are simulating. This leads to the situation that different packages are able to more accurately simulate different physics processes and careful consideration and investigation is necessary to ensure that the simulations used in the analysis are as accurate as possible. For example ALPGEN [58] calculates different jet multiplicities individually, which is important when simulating W+jets events, but POWHEG [59] calculates the corrections from higher order terms in such a way that it minimizes the occurance of negatively weighted events which are unphysical. Since $W' \to t\bar{b}$ is a single top process it was extremely useful to consult the extensive work already done comparing the different MC generator and showering programs for each process by the ATLAS single top group.

For all processes except W' the current ATLAS single top group recomendation has been used. For the W' signal processes the MADGRAPH [60] generator has been used due to its ease of implementation and handling of spin correlations of decays. The W' events were showered with PYTHIA [61] similar to most of the background signals. Table 6.2 shows which programs were chosen to simulate each sample's generation and showering [60] [61] [59] [62] [58] [63]. With the exception of the data driven methods described in Section 6.4, the background and signal samples are normalized to the expected number of events from each process using their theoretical cross-sections (σ), the total luminosity ($\mathcal{L}$), and a k-factor (k) which estimates the higher order corrections to the cross-section. Equation 6.1 gives the normalized number of events expected for each sample (N). The cross-section and k-factor values for the signal and background samples are given in Table 6.1 and Table 6.2 respectively. The W'_L and W'_R samples have different cross-sections at each mass point because the W'_L boson can decay leptonicaly while the W'_R boson cannot, which decreases the cross-section of the $W' \to t\bar{b}$ process by approximately 30% for a W'_L boson relative to that for a W'_R boson. The absence of a leptonic decay channel for a W'_R boson also means that the width of the W'_R boson is approximately 30% smaller than that of a W'_L boson. Since the width of both the W'_L and W'_R bosons are proportional to the W' mass, the absolute value of the difference in the W'_L and W'_R boson widths is larger for larger W' masses. This causes the cross-section for W'_L production to fall less rapidly as the W' mass increases than that of W'_R production, because the increased width of the W'_L makes it more likely to be produced by partons with a lower fraction of the total momentum in a collision, which are far more prevalent.

$$N = k\sigma\mathcal{L} \tag{6.1}$$

W' Mass [GeV]	W'_L σ [pb]	W'_L k	W'_R σ [pb]	W'_R k
500	12.333	1.3684	17.510	1.2906
750	2.7223	1.3144	3.7174	1.2779
1000	0.81915	1.2564	1.0652	1.2796
1250	0.28025	1.2405	0.37278	1.2260
1500	0.10618	1.2202	0.13932	1.2183
1750	0.043693	1.1893	0.055667	1.2062
2000	0.018551	1.1774	0.023718	1.1740
2250	0.0082073	1.1638	0.010283	1.1669
2500	0.0038171	1.1512	0.0046794	1.1485
2750	0.0018512	1.1529	0.0021970	1.1522
3000	0.00095811	1.1687	0.0011035	1.1592

Table 6.1: Cross-sections and k-factors for generated W' samples [3].

Process	σ [pb]	k	Reference	Generator	Showering
single top s-channel	1.6424	1.1067	[64]	POWHEG	Pythia
single top t-channel	25.750	1.1042	[65]	AcerMC	Pythia
single top Wt-channel	20.461	1.0933	[66]	POWHEG	Pythia
$t\bar{t}$	114.51	1.1992	[67]	POWHEG	Pythia
W+lf	31994	1.133	[68]	ALPGEN	Pythia
W+c	1126.0	1.52	[68]	ALPGEN	Pythia
W+cc	403.44	1.133	[68]	ALPGEN	Pythia
W+bb	133.99	1.133	[68]	ALPGEN	Pythia
Z+jets	2804.4	1.229	[68]	ALPGEN	HERWIG
diboson	17.075	1.7223	[69]	HERWIG	HERWIG

Table 6.2: Simulated background samples with associated cross-sections, k-factors, generating programs and showering programs.

6.4 Data driven estimates

While the above method works well to simulate many background processes, it is sometimes useful to use control regions in the data to estimate some backgrounds. For the W+jets process it is necessary to correct the overall normalization as well as the relative abundance of the simulated samples based on the flavor of the associated jets as described in Section 6.4.1. The multijets process has a very high rate of occurrence and a very low acceptance making it very difficult to predict, so this analysis uses the matrix method to estimate this background from data as described in Section 6.4.2.

6.4.1 W+jets normalization

The W+jets samples in this analysis are globally normalized using the charge asymmetry method in the control region where m(W') $<$ 330 GeV, as defined by the event selection in Section 5.3. This region has a signal contamination $< 5\%$ for all W' mass points considered in the analysis. This method normalizes the W+jets sample in each analysis channel using the theoretical asymmetry ratio (r_{MC}) as defined in Equation 6.2 to account for the observed asymmetry in data.

$$r_{MC} = \frac{N_{MC\ W^{+}events}}{N_{MC\ W^{-}events}} \tag{6.2}$$

The asymmetry ratio is used to derive the W+jets normalization because while the theoretically predicted total production rates of W^{+}+jets and W^{-}+jets do not agree with what is seen in experimental data, the ratio of these rates (r_{MC}) does. The W+jets samples are normalized so that the difference in the expected number of W+jets events in Monte Carlo simulation with positive and negative leptons ($N_{W+} - N_{W-}$) is the same as the observed difference in the number of data events with positive and negative leptons ($D^+ - D^-$). This results in an overall normalization factor for each analysis channel which is measured in the control region of that channel, as shown in Equation 6.6.

$$N_{W+} - N_{W-} = D^+ - D^- \tag{6.3}$$

$$(N_{W+} - N_{W-})\frac{N_{W+} + N_{W-}}{N_{W+} + N_{W-}} = D^+ - D^- \tag{6.4}$$

$$(N_{W+} + N_{W-}) = \frac{N_{W+} + N_{W-}}{N_{W+} - N_{W-}}(D^+ - D^-) \tag{6.5}$$

$$N_{W+} + N_{W-} = \frac{r_{MC} + 1}{r_{MC} - 1}(D^+ - D^-) \tag{6.6}$$

While this gives an overall normalization for the W+jets sample in each analysis channel, Monte Carlo predictions of the relative fraction of W+jets events with different jet flavors disagree with what is observed in data by factors of up to 2. To correct for this, the relative normalization of the Wbb, Wcc, Wc, and Wlf samples is determined by fitting to the data. There are a variety of ways to perform this fit, and for this analysis the charge asymmetry analytic method is used. In this method each of the W+jets samples has an associated normalization factor F such that:

$$F_{bb} + F_{cc} + F_c + F_{lf} = 1 \tag{6.7}$$

These relative normalization factors are determined by using the data normalized total number of events in the control region that contain a W$^+$ (W$^-$) boson and pass the b-tagging requirements N_{W+}^{tagged} (N_{W-}^{tagged}) and the data normalized number of events in the control region that contain a W$^+$ (W$^-$) boson with the b-tagging requirements removed $N_{W+}^{pre-tagged}$ ($N_{W-}^{pre-tagged}$) as shown in Equations 6.8 and 6.9.

$$N_{W+}^{tagged} = N_{W+}^{pre-tagged}(F_{bb}P_{bb} + F_{cc}P_{cc} + F_cP_c + F_{lf}P_{lf}) \tag{6.8}$$

$$N_{W-}^{tagged} = N_{W-}^{pre-tagged}(F_{bb}P_{bb} + F_{cc}P_{cc} + F_cP_c + F_{lf}P_{lf}) \tag{6.9}$$

where P is the tagging fraction of each sample, measured for each of the Monte Carlo samples according to:

$$P = \frac{N^{tagged}}{N^{pre-tagged}} \tag{6.10}$$

This leaves three equations (6.7,6.8,6.9) and four variables to be fit (F_{bb},F_{cc},F_c,F_{lf}). In order to solve this system of equations the relative normalization of Wbb and Wcc are assumed to be the same, giving Equation 6.11

$$F_{bb} = F_{cc} \tag{6.11}$$

The relative W+jets normalization is not expected to change between the analysis channels so it is determined for all of the analysis channels using the 2jets 2tag channel because this results in the smallest uncertainty in the normalization factors.

The total normalization factors for each sample are the product of the overall normalization for each analysis channel and the relative normalization of the W+jets flavors and they are given in Table 6.3.

Process	2jets 1tag	2jets 2tag	3jets 1tag	3jets 2tag
W+lf	0.941462	1.31867	0.883688	1.96718
W+c	0.801521	1.12266	0.752335	1.67477
W+cc	1.39795	1.95806	1.31217	2.92102
W+bb	1.39795	1.95806	1.31217	2.92102

Table 6.3: W+jets normalization factors.

6.4.2 Multijets estimate

The contribution of the multijet process to this analysis is estimated using the matrix method [70]. The matrix method uses data events which have passed the event selection in Chapter 5 except with a loose lepton which has relaxed requirements compared to the tight lepton required for the signal region. Both the loose and tight lepton categories are defined in Chapter 4. For both electrons and muons

$$N^{loose} = N^{loose}_{real} + N^{loose}_{fake} \tag{6.12}$$

$$N^{tight} = N^{tight}_{real} + N^{tight}_{fake} \tag{6.13}$$

where N is the number of data events containing a lepton of the indicated type. Equation 6.13 can be rewritten using the conversion efficiencies for loose real or fake leptons to tight real or fake leptons $\epsilon_{real} = \frac{N^{tight}_{real}}{N^{loose}_{real}}$ and $\epsilon_{fake} = \frac{N^{tight}_{fake}}{N^{loose}_{fake}}$ as:

$$N^{tight} = \epsilon_{real} N^{loose}_{real} + \epsilon_{fake} N^{loose}_{fake} \tag{6.14}$$

ϵ_{real} is estimated using the tag and probe method[1] on $Z \to ll$ events, while ϵ_{fake} is estimated

[1]The tag and probe method involves requiring that events contain one tight lepton (the

using a multijets enhanced data sample where the lepton isolation criteria have been removed and subtracting the expected contribution of real leptons in the sample based on Monte Carlo simulations. Equations 6.12 and 6.14 can be combined into a single matrix equation given in Equation 6.15.

$$\begin{pmatrix} N^{loose} \\ N^{tight} \end{pmatrix} = \begin{pmatrix} 1 & 1 \\ \epsilon_{real} & \epsilon_{fake} \end{pmatrix} \begin{pmatrix} N^{loose}_{real} \\ N^{loose}_{fake} \end{pmatrix} \tag{6.15}$$

With the total number of events with loose and tight leptons known from the dataset, Equation 6.15 can be inverted and combined with the definition of the fakes conversion efficiency ϵ_{fake} to solve for N^{tight}_{fake} as shown in Equation 6.16. The conversion efficiencies are dependent on many parameters including the lepton type (electron or muon), the pseudorapidity of the lepton, E_T of the lepton, p_T of the jets, and the relative positions of the lepton, jets, and $E_{\mathrm{T}}^{\mathrm{miss}}$in each event. Averaging over this dependence, the conversion efficiencies are approximately $\epsilon_{real} = 0.75$ and $\epsilon_{fake} = 0.15$ [70]. N^{tight}_{fake} is the multijets estimate for the analysis.

$$N^{tight}_{fake} = \frac{\epsilon_{fake}}{\epsilon_{real} - \epsilon_{fake}} (\epsilon_{real} N^{loose} - N^{tight}) \tag{6.16}$$

6.5 Event yields

Event yields are the expected number of events which pass the event selection for each process. This gives the importance of each background if a simple counting experiment were performed, and gives the expected size of a signal. The final event yields are shown in

tag) and one loose lepton (the probe), then measuring how often the probe passes the tight requirements

Table 6.4 broken into the four analysis channels. The number of data events which pass the event selection for each channel are also included for comparison to the expected background and signal yields.

In all four analysis channels the dominant backgrounds are the $t\bar{t}$ and W+jets processes, with $t\bar{t}$ being the largest background in all of the analysis channels except 2jets 1tag. The 1tag analysis channels contain approximately double the number of signal events of the 2tag channels for high mass W' samples because the jets produced by the W' boson decay have larger momenta and the MV1 b-tagging algorithm has lower efficiency for higher p_T jets. After the event selection cuts, the expected number of signal events is much smaller than the expected number of background events for all but the lowest W' masses in the analysis. For example a 1750 GeV W'_R is expected to produce appoximately 100 events in the analysis with a background of approximately 70,000 events. It is not possible to observe such a signal by simply looking for an excess in the event count so more sophisticated analysis and statistical techniques are used to increase the sensitivity of the analysis as described in Chapter 7 and Chapter 8 respectively.

Sample	2jets 1tag	3jets 1tag	2jets 2tag	3jets 2tag
$W'_R 500$	11908.99	5323.81	12949.42	8316.48
$W'_R 750$	3896.54	2648.34	2694.86	2514.05
$W'_R 1000$	1088.92	917.25	628.33	697.37
$W'_R 1250$	331.79	306.02	158.79	195.92
$W'_R 1500$	100.05	106.23	42.93	58.95
$W'_R 1750$	31.56	35.94	12.45	18.65
$W'_R 2000$	10.95	12.95	4.28	6.47
$W'_R 2250$	4.02	4.97	1.60	2.16
$W'_R 2500$	1.68	1.91	0.71	0.91
$W'_R 2750$	0.79	0.84	0.39	0.45
$W'_R 3000$	0.41	0.41	0.22	0.25
$W'_L 500$	5924.22	2769.90	7114.70	4699.89
$W'_L 750$	2119.14	1408.07	1578.82	1418.04
$W'_L 1000$	631.77	536.05	400.88	443.46
$W'_L 1250$	215.28	201.18	109.11	135.53
$W'_L 1500$	70.61	73.48	31.47	43.29
$W'_L 1750$	24.56	28.93	10.48	14.21
$W'_L 2000$	9.20	10.59	3.44	4.92
$W'_L 2250$	3.59	4.31	1.41	1.99
$W'_L 2500$	1.55	1.78	0.62	0.80
$W'_L 2750$	0.68	0.77	0.32	0.41
$W'_L 3000$	0.38	0.39	0.20	0.22
single top s-channel	123.09	66.60	193.12	107.91
single top t-channel	1729.45	960.21	730.92	951.84
single top Wt-channel	585.03	924.49	282.40	750.19
$t\bar{t}$	4261.02	8756.59	5335.20	14774.80
W+lf	2727.00	1165.34	104.86	173.67
W+c	4545.80	1843.93	416.31	389.15
W+cc	3161.70	2312.68	460.47	637.16
W+bb	3039.62	1941.79	1662.80	2324.34
Z+jets	310.38	342.36	12.69	50.07
diboson	202.15	112.55	91.52	59.79
multijets	986.54	453.47	377.48	396.18
total background	21671.79	18880.02	9667.75	20615.10
data	19362.00	16919.00	9839.00	20388.00

Table 6.4: Event yields for signal samples, background samples, and data by analysis channel.

Chapter 7

Multivariate analysis

The event selection described in Chapter 5 does not optimize the statistical significance of a potential signal in each of the analysis channels. The method used to optimize the significance in this analysis is a boosted decision tree (BDT) multivariate analysis (MVA). The details of the BDT algorithm are discussed in Section 7.1, but the basic premise is that events are sorted into background-like and signal-like bins using a series of cuts called a decision tree. This decision tree optimizes the separation of signal and background events by collecting all of the events into a decision node and then placing a cut on a single variable, with both output possibilities forming a new decision node. A new optimal cut is placed on each decision node iteratively until the specified end conditions are met. Misclassified events, which are signal events in a background-like bin or background events in a signal-like bin, have their relative weight "boosted" and a new decision tree is trained. This training and boosting process is iterated many times and all of the decision trees combined form the BDT. This boosting serves to increase the importance of hard to classify events by increasing their weight in the optimization and make them more likely to be correctly categorized in subsequent decision trees. A final decision weight is assigned to each event based on the aggregate purity of the bins it was sorted into in each decision tree, which represents how signal-like or background-like each event is. This iterative process allows for a more nuanced handling of variable correlations than a simple cuts based analysis which is effectively a single decision tree. The BDT also has the convenient property that it condenses the discrimination power from many variables into a single highly discriminating weight which is more easily displayed for the human analyst.

7.1 Boosted decision trees

The boosted decision tree (BDT) algorithm [71] is designed to optimize the discrimination between signal and background events. The implementation of the BDT algorithm used in this analysis is done by the Toolkit for Multivariate Data Analysis with ROOT (TMVA) [53] and while the principles of the analysis are general to all BDTs, the details are specific to this software package. Each of the analysis channels (2jets 1tag, 2jets 2tag, 3jets 1tag, and 3jets 2tag) has an independent BDT trained with the variables for each channel described in Section 7.1.2, and the BDT settings for each channel are described in Section 7.1.3.

The BDT training begins with a sample of Monte Carlo signal and background events, with each event having a weight equal to its contribution to the overall normalization[1] and a set of kinematic variables defined to be used in the BDT. An optimal cut on one of these variables is determined by maximizing ΔG as defined in Equation 7.1 for all possible cuts on these variables where $G_{pre-cut}$ is calculated for all of the events and $G_{passed\ cut}$ and $G_{failed\ cut}$ are calculated for the events which pass and fail the cut respectively.

$$\Delta G = G_{pre-cut} - G_{passed\ cut} - G_{failed\ cut} \tag{7.1}$$

Where G is called the Gini index and is given in Equation 7.2:

[1]Because of how they are produced, a single Monte Carlo event does not represent a single data event but could represent more or less than one data event depending on the likelihood of the MC event occuring.

$$G = \sum_{events} WP(1 - P) \tag{7.2}$$

In Equation 7.2 W is the event weight, and P is the purity defined as the fraction of events belonging to the signal. With the optimal separation cut defined all of the events are sorted into two bins: events that pass the cut, and events that fail the cut. The process of finding the optimal cut and sorting the events based on that cut forms a decision node.

Each of the two output bins from the first decision node then form their own decision nodes to be applied to only those events. A new optimal cut is determined for each of these nodes and the events are sorted into four bins (two for each decision node). This process is continued iteratively, further subdividing the sample into more bins at each iteration, until a termination condition is met. There are two termination conditions: a minimum number of events is required to be in a bin in order for that bin to become a new decision node, and there is a maximum depth in the decision tree for a node to become a decision node. The initial decision node is at a depth of 1, the bins output from that decision node are at a depth of 2, and so on. Any bins that do not form decision nodes instead form termination nodes and are defined as signal or background nodes based on the majority of events in that termination node. The decision and termination nodes together form a decision tree, an example of which is given in Figure 7.1.

While a single decision tree can provide some discrimination power between signal and background events, the discrimination power can generally be increased by training multiple decision trees and increasing the weight of events misclassified as either signal or background by each tree. A misclassified event is a signal event that is sorted into a background termination node or a background event that is sorted into a signal termination node, and this

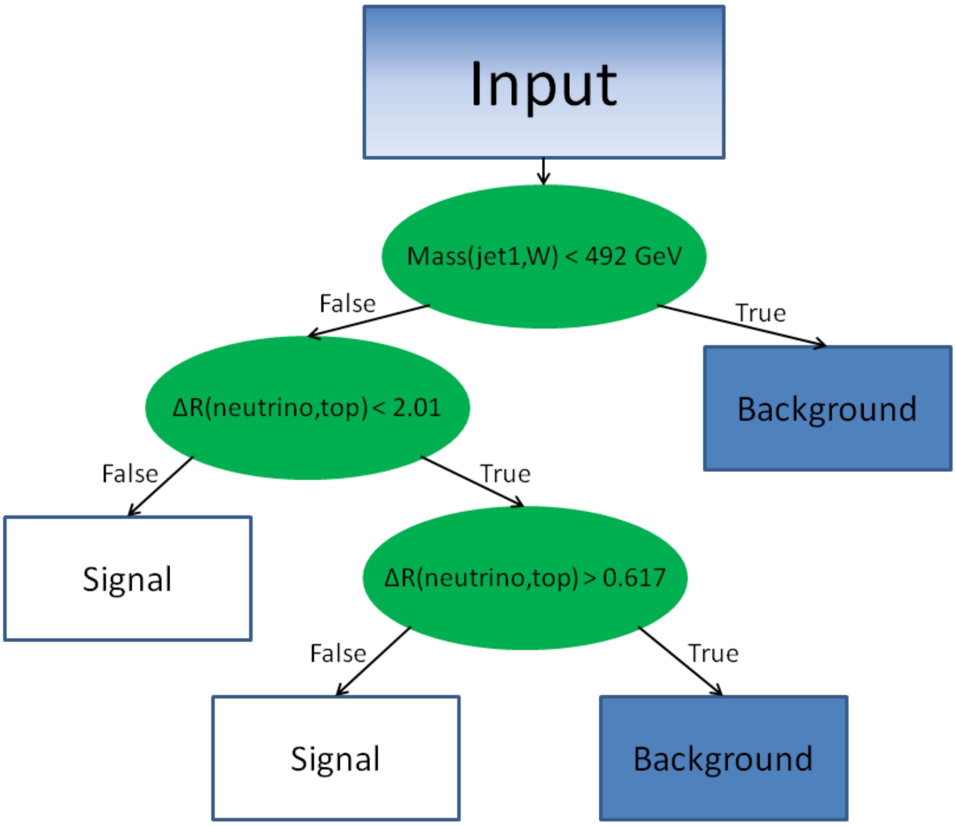

Figure 7.1: An example decision tree which sorts input events into signal and background bins. The variables used in the decision tree are described in Section 7.1.2

analysis uses the Adaboost algorithm [53] to increase the weight of such events when training subsequent decision trees. The new weight of a misclassified event is given by $w_{boosted}$ in Equation 7.3, where β is the boosting strength and is one of the parameters optimized in Section 7.1.3 while $w_{pre-boosted}$ is the event weight before being boosted.

$$w_{boosted} = \left(\frac{1 - err}{err}\right)^{\beta} w_{pre-boosted} \tag{7.3}$$

where err is defined as:

$$err = \frac{sum\ of\ misclassified\ event\ weights}{sum\ of\ all\ event\ weights} \tag{7.4}$$

After the misclassified events have their weights boosted, all events have their weights scaled to keep the total sum of event weights normalized and a new decision tree can be trained. The total number of decision trees trained is one of the parameters optimized in Section 7.1.3.

With each event being sorted by multiple decision trees, an aggregate BDT decision weight (y_{Boost}) is formed by taking a weighted average of the individual decision tree responses as given by Equation 7.5.

$$y_{Boost} = \frac{\sum_{i=1}^{N_{Trees}} ln\left(\frac{1-err_i}{err_i}\right) h_i}{\sum_{i=1}^{N_{Trees}} ln\left(\frac{1-err_i}{err_i}\right)} \tag{7.5}$$

For Equation 7.5, N_{Trees} is the total number of decision trees trained and err_i is given by Equation 7.4 for each tree. The result of each tree for the event is represented by h_i, which is $+1$ (-1) if the event was sorted into a signal (background) termination node by that tree. Thus the final BDT decision weight for each event is a value between -1 and $+1$, where -1

represents an ideal background event and +1 represents an ideal signal event.

7.1.1 Overtraining

If the BDT has too many degrees of freedom compared to the statistical size of the generated samples during training then the BDT begins to optimize the decision trees based on the specific variable values of individual events rather than on the overall distributions. This is called overtraining and it causes the BDT output to be drastically different if the trained BDT is applied to a new sample simulated under identical conditions. In order to check if a BDT is overtrained all of the event samples are split in half before training. One half, called the training sample, is used to train the BDT and is run through the resulting BDT to compute the BDT decision weight distribution. The remaining half of the events, called the testing sample, is run through the already trained BDT and produces an independant BDT decision weight distribution. The training and testing distributions for both the signal and background samples should be similar if the BDT is not overtrained, and they are compared using a Kolmgorov-Smirnov (KS) test [72]. The KS test provides a probability that two samples come from the same distribution, and if the KS result is < 0.5 for either the signal or background distributions then the BDT is determined to be overtrained.

7.1.2 Variable selection

The variables that are used in the BDT to separate the signal and background events have a large impact on the separation power of the BDT. Variables should be chosen that can discriminate between signal and background events, where the discrimination power is defined the same as in Section 5.3. Because the correlations between several different variables are not always obvious for all of the different processes included in the signal and background samples, the analysis begins with a large list of variables in an attempt to be as comprehensive as possible. For each sample the analysis objects, as defined in Chapter 4, are the lepton (lep), reconstructed neutrino (neutrino), reconstructed W boson (W), reconstructed top quark (top), reconstructed W' boson (W'), the leading jet (jet1), the sub-leading jet (jet2), the leading b-tagged jet (bjet1), and in the appropriate analysis channels the third jet (jet3) and sub-leading b-tagged jet (bjet2). For each of these objects the energy, mass, pseudorapidity (η), azimuthal angle (ϕ), transverse momentum (p_T), and transverse energy (E_T) are considered as possible variables for inclusion in the BDT. In addition a set of two body variables is included in this list which consists of the invariant mass, difference in pseudorapidity ($\Delta\eta$), difference in azimuthal angle ($\Delta\phi$), and opening angle (ΔR) for every pair of analysis objects. A final set of global event variables consisting of the $E_{\mathrm{T}}^{\mathrm{miss}}$, the azimuthal angle of the $E_{\mathrm{T}}^{\mathrm{miss}}(\phi(E_{\mathrm{T}}^{\mathrm{miss}}))$, the total sum of the transverse energy in the event (Sum E_T), the total sum of the transverse energy of only the analysis object in the event (H_T), the aplanarity of the event (a measure of how much of the energy in the event resides in one plane), and the sphericity of the event (a measure of how evenly the energy of an event is distributed around the interaction point) are also included. This forms an initial list of approximately 200 variables depending on the analysis channel, however past experience in single top and $W' \to t\bar{b}$ analyses at ATLAS suggests that fewer than 20 variables are necessary for a BDT to achieve good separation of single top signal and background events. In order to remove unnecessary variables, variables with a discrimination power[2] $< 20\%$ are removed from the list for each channel which leaves approximately 50 variables per channel. It is important that these variables are well modeled so the background distributions are

[2] Discrimination power is defined in Section 5.3.

2jets 1tag	3jets 1tag	2jets 2tag	3jets 2tag
p_T(top)	mass(jet1,W)	mass(W')	mass(W')
mass(W')	H_T	ΔR(lepton,top)	sphericity
E(W')	mass(W')	aplanarity	p_T(top)
mass(jet1,jet2)	mass(jet1,jet2)	H_T	$\Delta\eta$(lepton,W)
$\Delta\eta$(lepton,W)	$E_{\mathrm{T}}^{\mathrm{miss}}$	p_T(bjet1)	E_T(bjet1)
Sum E_T	ΔR(neutrino,top)	p_T(bjet2)	ΔR(bjet1,top)
mass(jet1,W)	E(lepton)	mass(bjet1,bjet2)	ΔR(lepton,bjet1)
ΔR(lepton,top)	p_T(top)	E_T(W)	$\Delta\phi$(W,top)
mass(lepton,jet1)	p_T(W)	ΔR(lepton,bjet2)	$\Delta\eta$(lepton,top)
$\Delta\eta$(neutrino,top)	E(W')	ΔR(bjet1,bjet2)	mass(lepton,bjet1)
E_T(lepton)	$\Delta\eta$(lepton,W)	ΔR(lepton,W)	ΔR(bjet1,W)
p_T(W)	mass(lepton,jet1)	p_T(top)	p_T(lepton)
H_T	ΔR(lepton,top)	sphericity	aplanarity
$E_{\mathrm{T}}^{\mathrm{miss}}$	mass(jet1,top)	p_T(lepton)	
$\Delta\eta$(neutrino,jet2)	$\Delta\eta$(neutrino,W)		
ΔR(jet2,W)			
ΔR(lepton,jet2)			
mass(jet1,top)			

Table 7.1: Boosted decision tree variable lists for the four analysis channels. Variables are ranked by importance.

compared to data and any variables with a KS value < 0.5 are removed. A BDT is then trained using the remaining variables and the variables are ranked by importance, which is how frequently they are used in the individual decision trees. The five least important variables are removed from the variable list and the process is repeated until only 20 variables remain. At this point the training and variable removal iterations continue but only a single variable is removed in each iteration until the removal of a variable would cause the separation power of the BDT to degrade to $< 90\%$ of the maximum value obtained during these iterations. Table 7.1 lists the final variables for each of the analysis channels in order of importance, and Figures 7.2-7.14 show the data-Monte Carlo comparison plots for these variables.

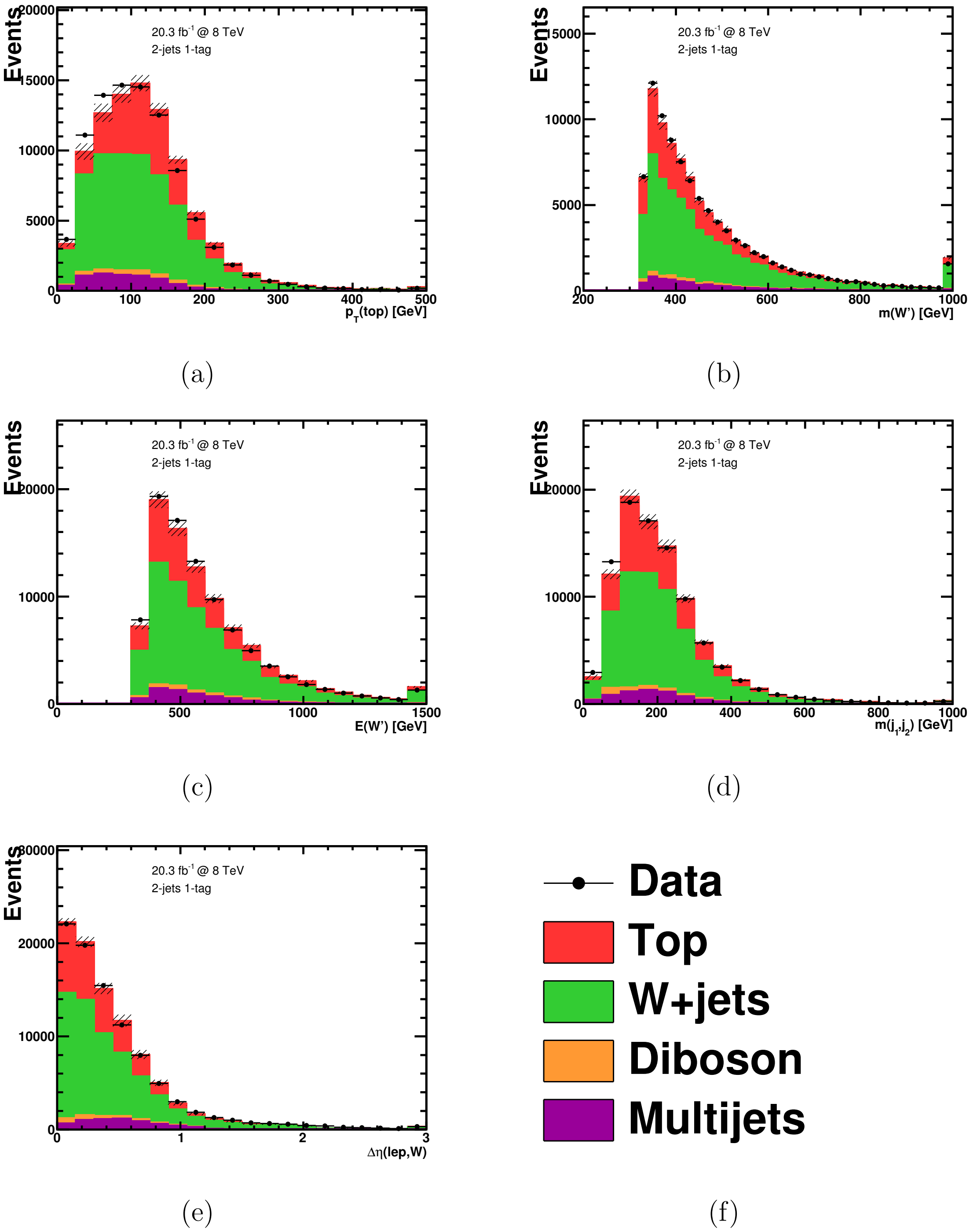

Figure 7.2: Comparison of data to Monte Carlo prediction of the 1st-5th variables by importance in the 2jet 1tag BDT.

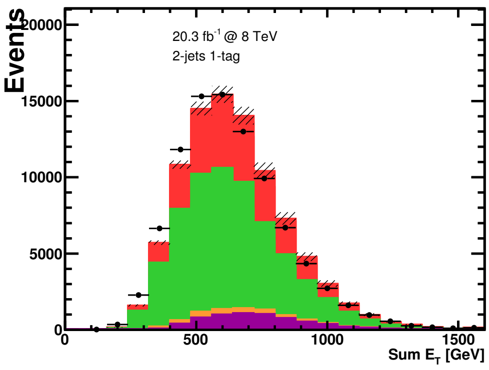

(a)

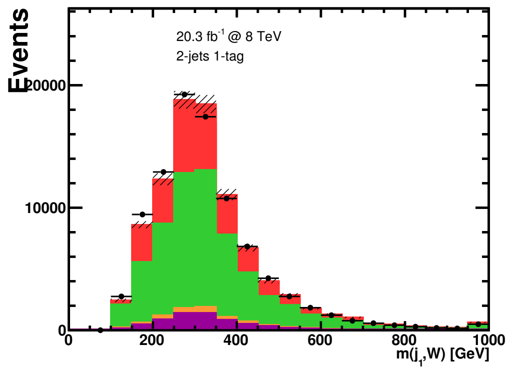

(b)

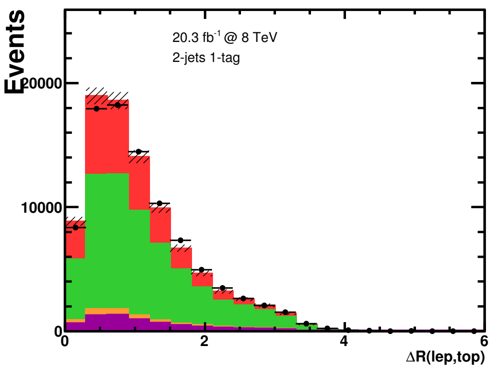

(c)

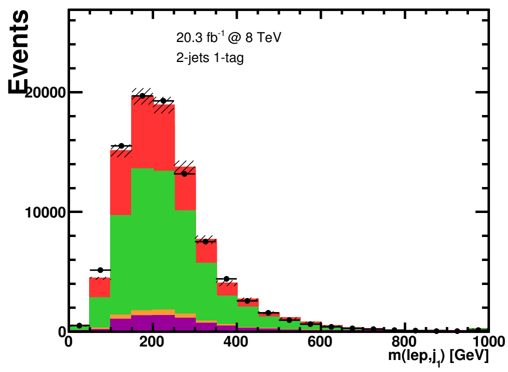

(d)

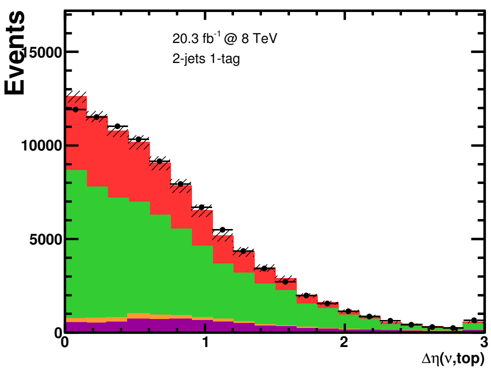

(e)

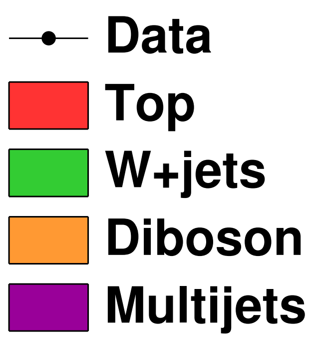

(f)

Figure 7.3: Comparison of data to Monte Carlo prediction of the 6th-10th variables by importance in the 2jet 1tag BDT.

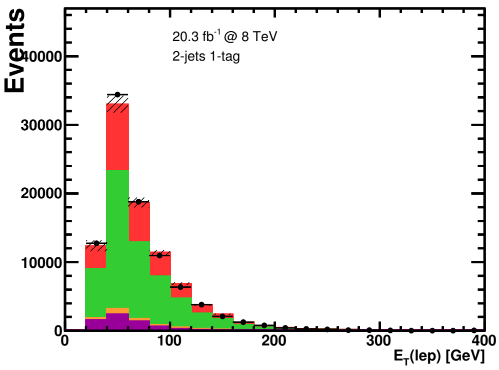

(a)

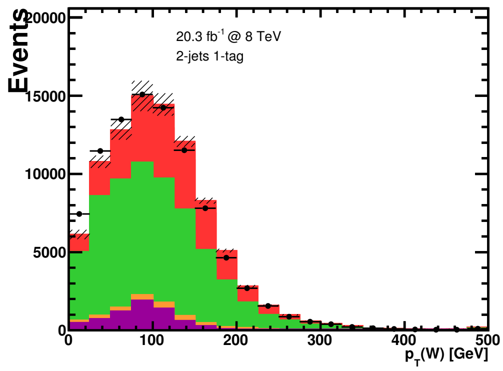

(b)

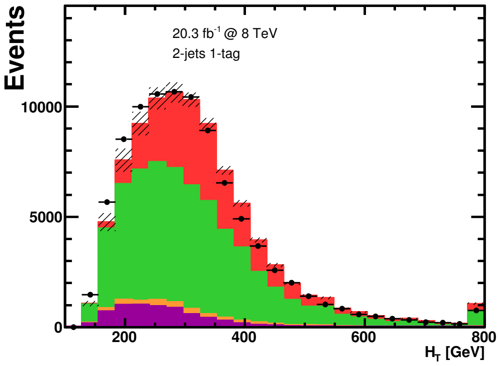

(c)

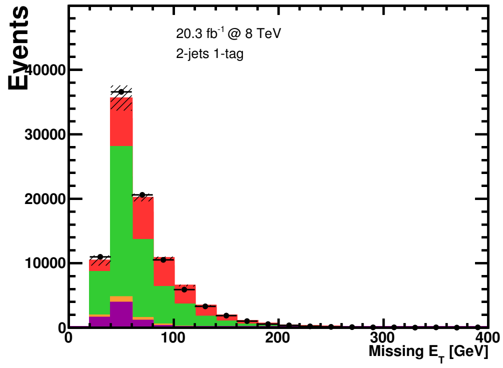

(d)

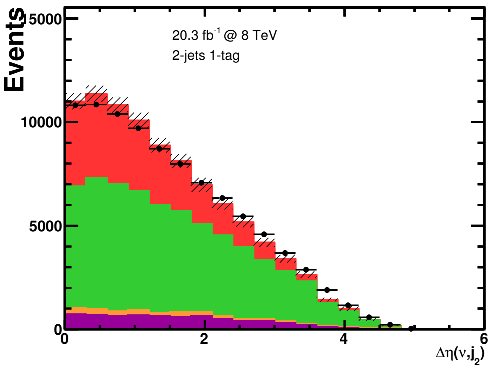

(e)

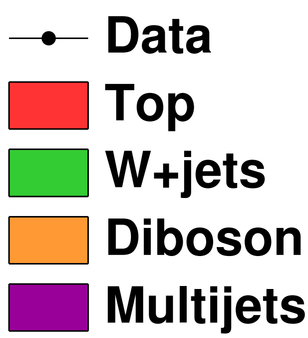

(f)

Figure 7.4: Comparison of data to Monte Carlo prediction of the 11th-15th variables by importance in the 2jet 1tag BDT.

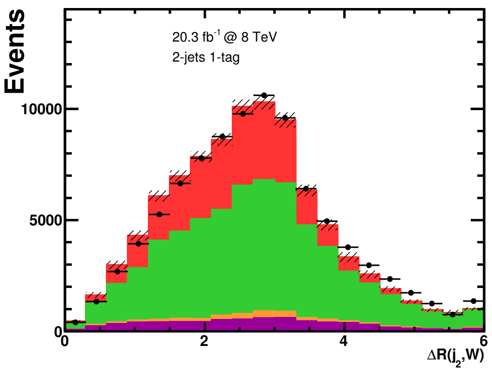

(a)

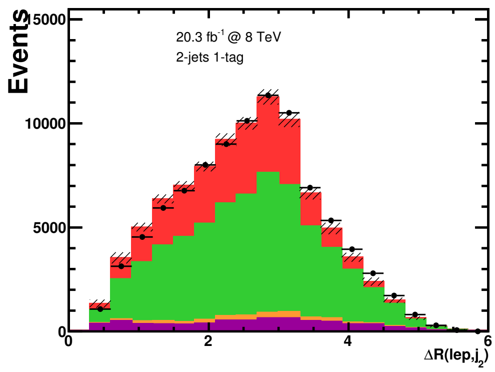

(b)

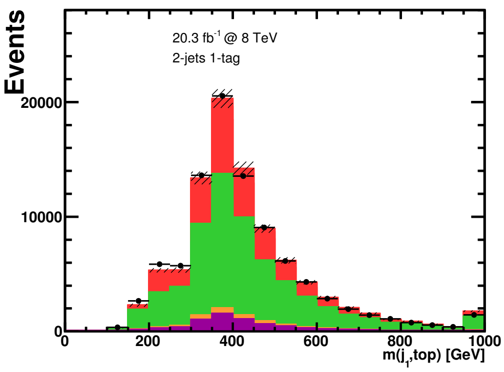

(c)

(d)

Figure 7.5: Comparison of data to Monte Carlo prediction of the 16th-18th variables by importance in the 2jet 1tag BDT.

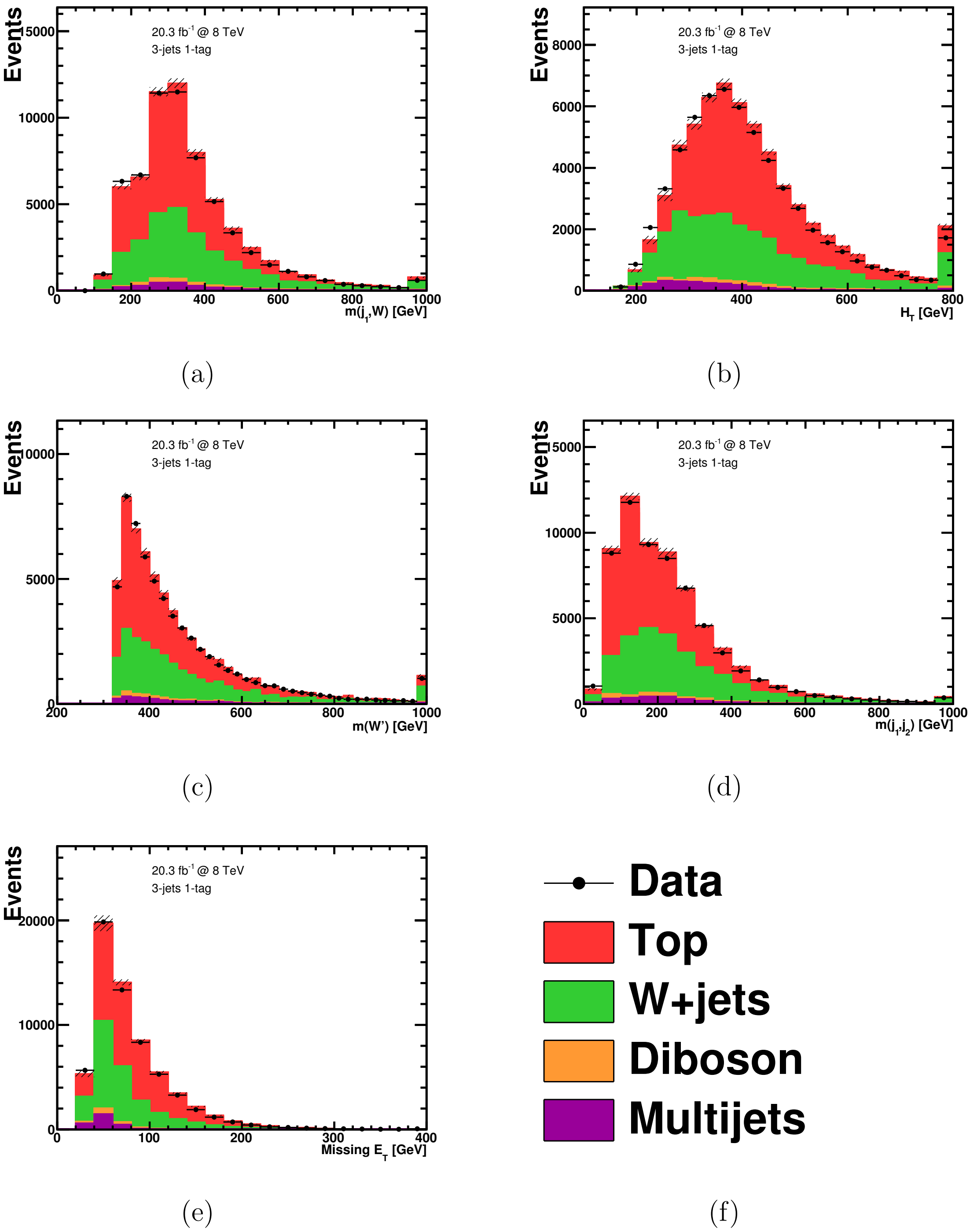

Figure 7.6: Comparison of data to Monte Carlo prediction of the 1st-5th variables by importance in the 3jet 1tag BDT.

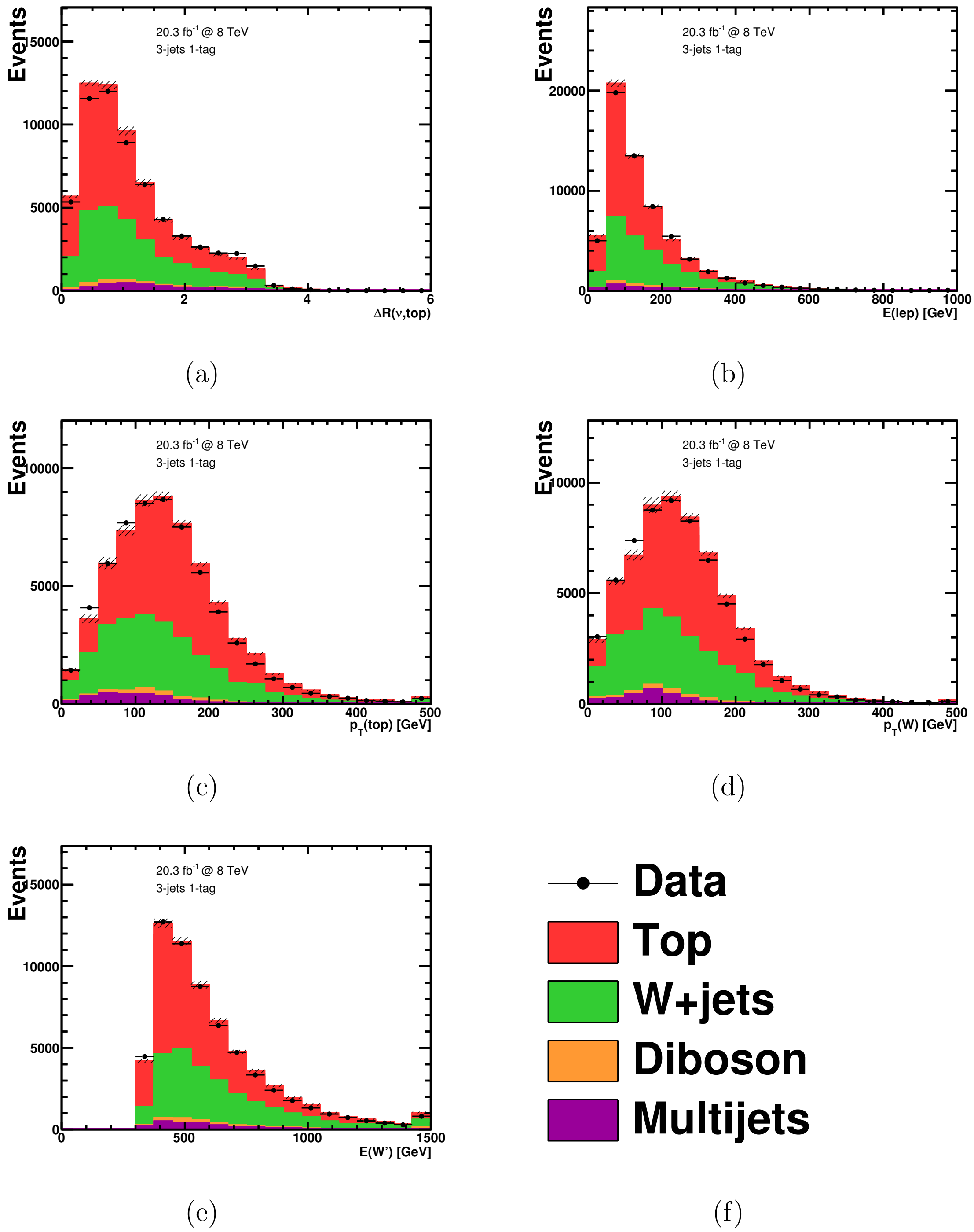

Figure 7.7: Comparison of data to Monte Carlo prediction of the 6th-10th variables by importance in the 3jet 1tag BDT.

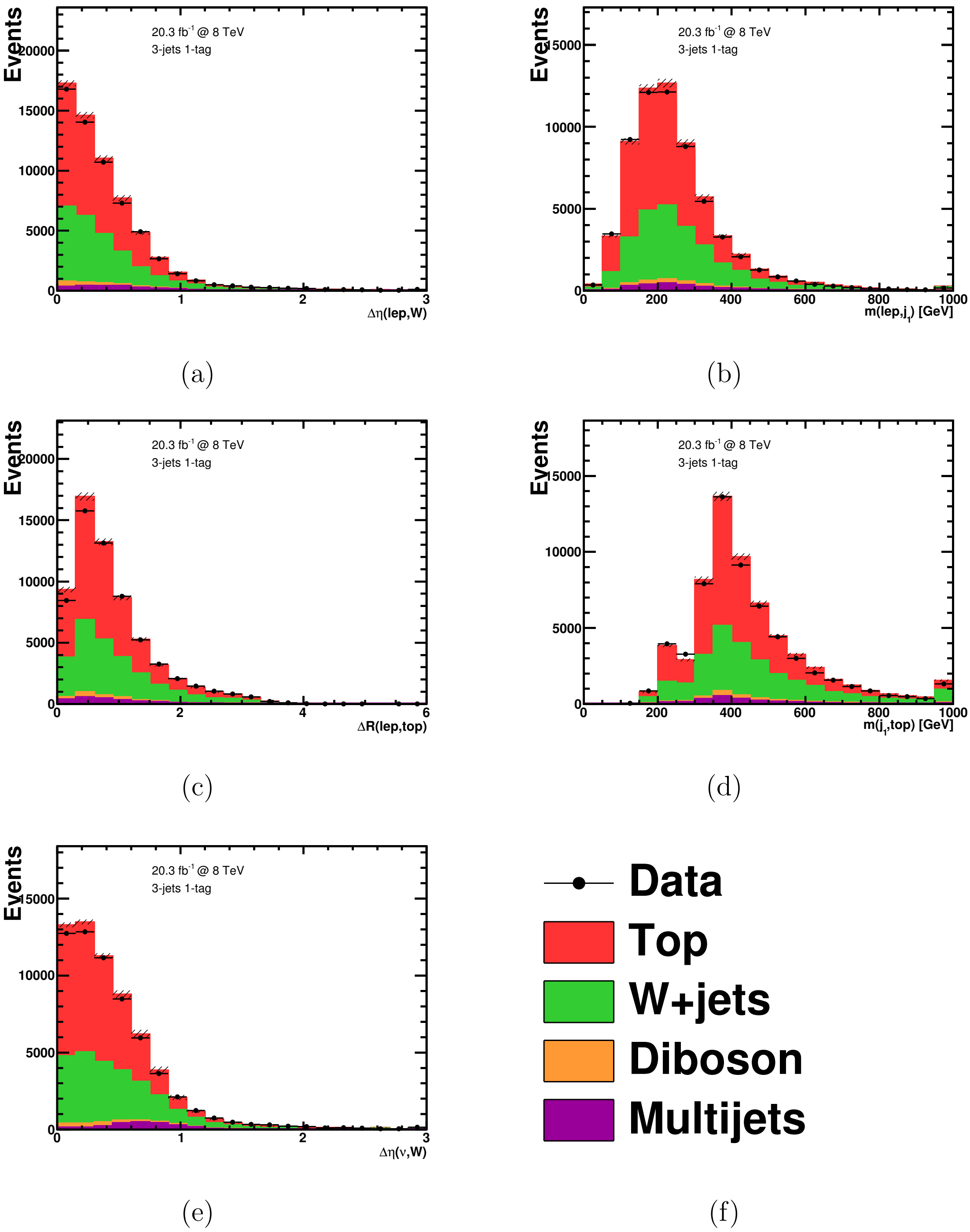

Figure 7.8: Comparison of data to Monte Carlo prediction of the 11th-15th variables by importance in the 3jet 1tag BDT.

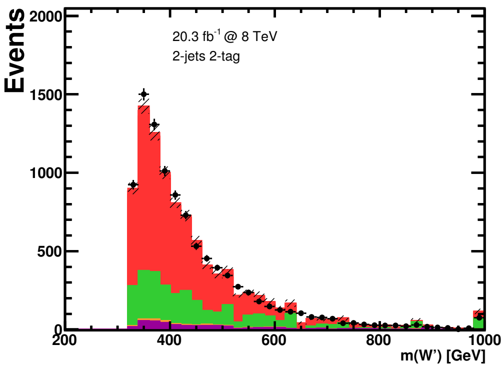

(a)

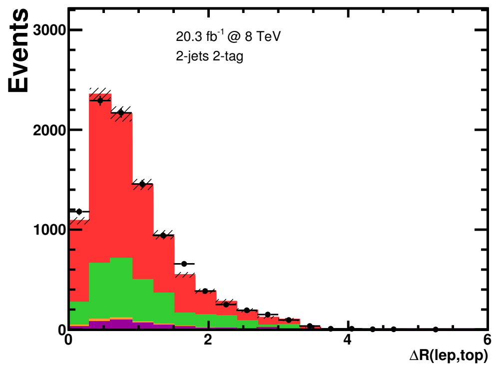

(b)

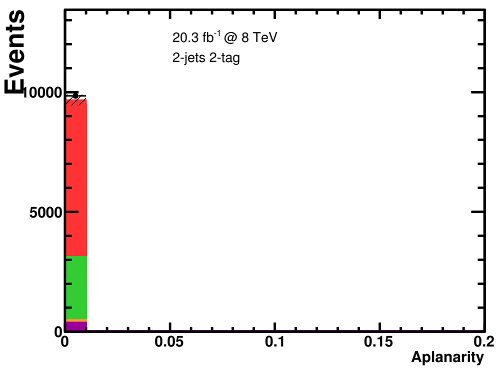

(c)

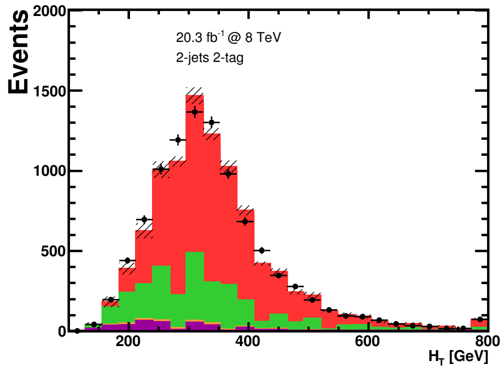

(d)

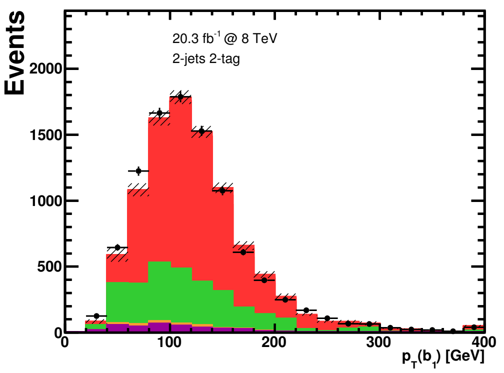

(e)

(f)

Figure 7.9: Comparison of data to Monte Carlo prediction of the 1st-5th variables by importance in the 2jet 2tag BDT.

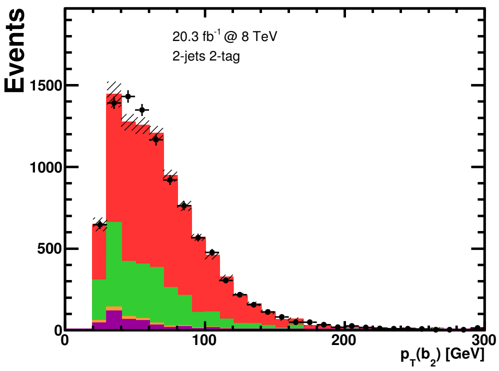

(a)

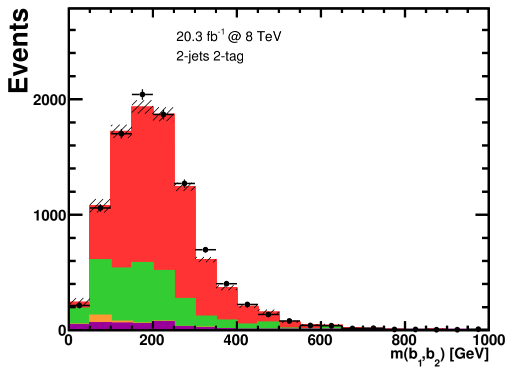

(b)

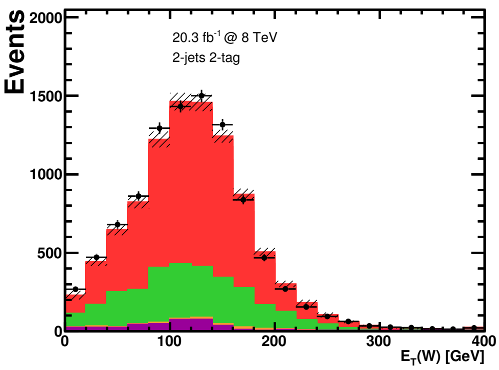

(c)

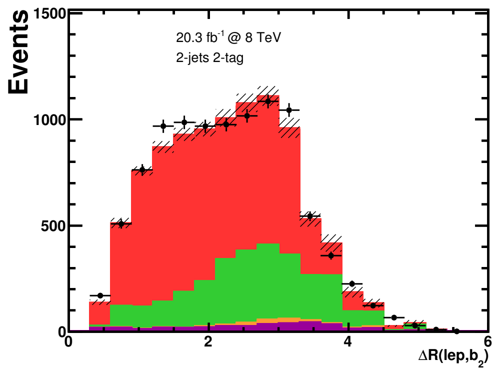

(d)

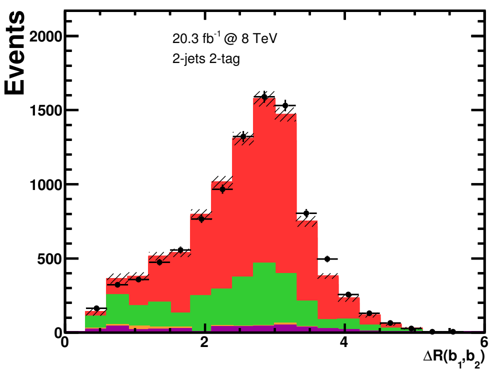

(e)

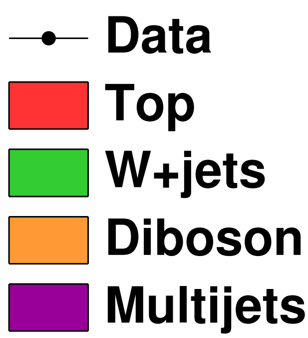

(f)

Figure 7.10: Comparison of data to Monte Carlo prediction of the 6th-10th variables by importance in the 2jet 2tag BDT.

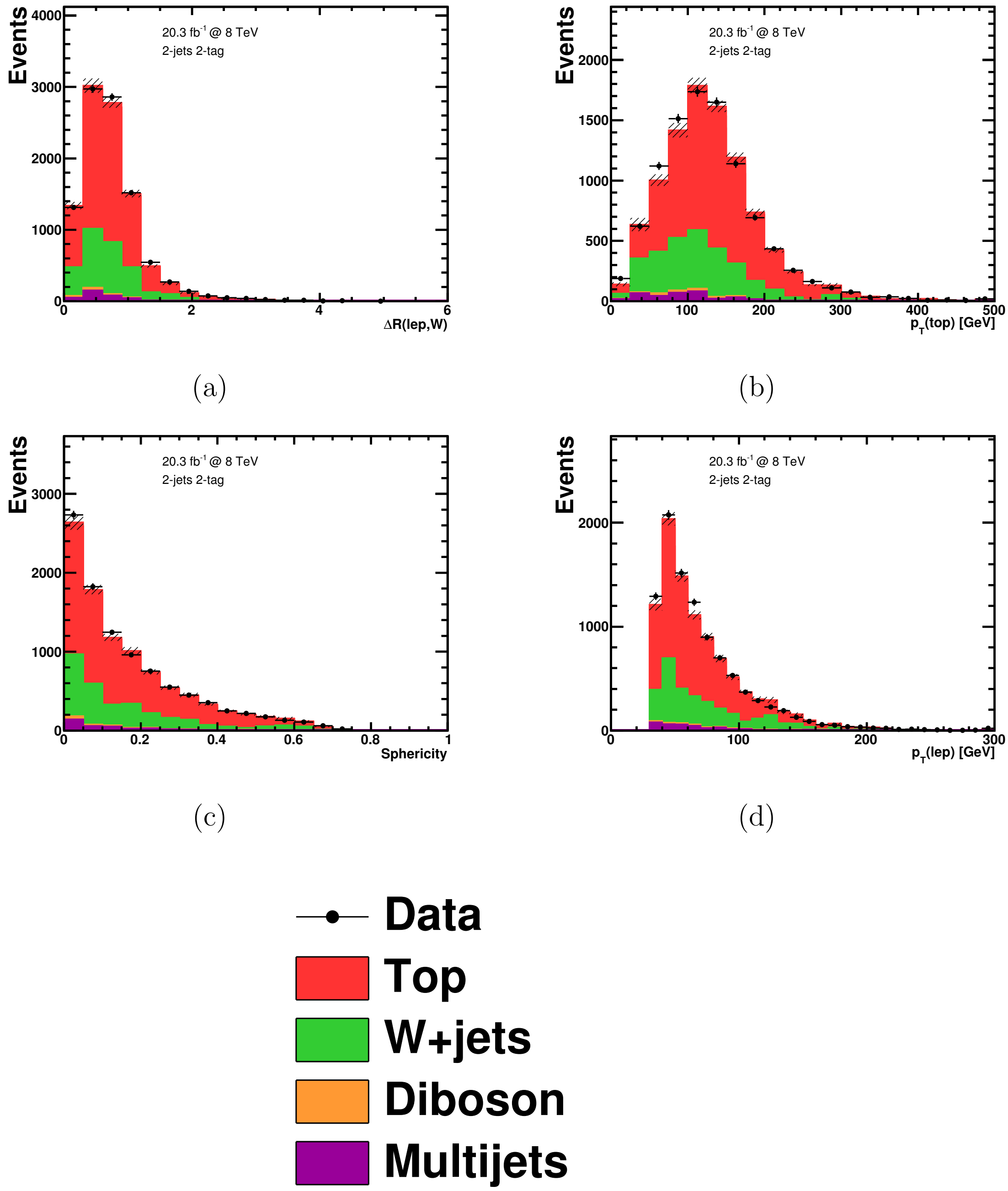

Figure 7.11: Comparison of data to Monte Carlo prediction of the 11th-14th variables by importance in the 2jet 2tag BDT.

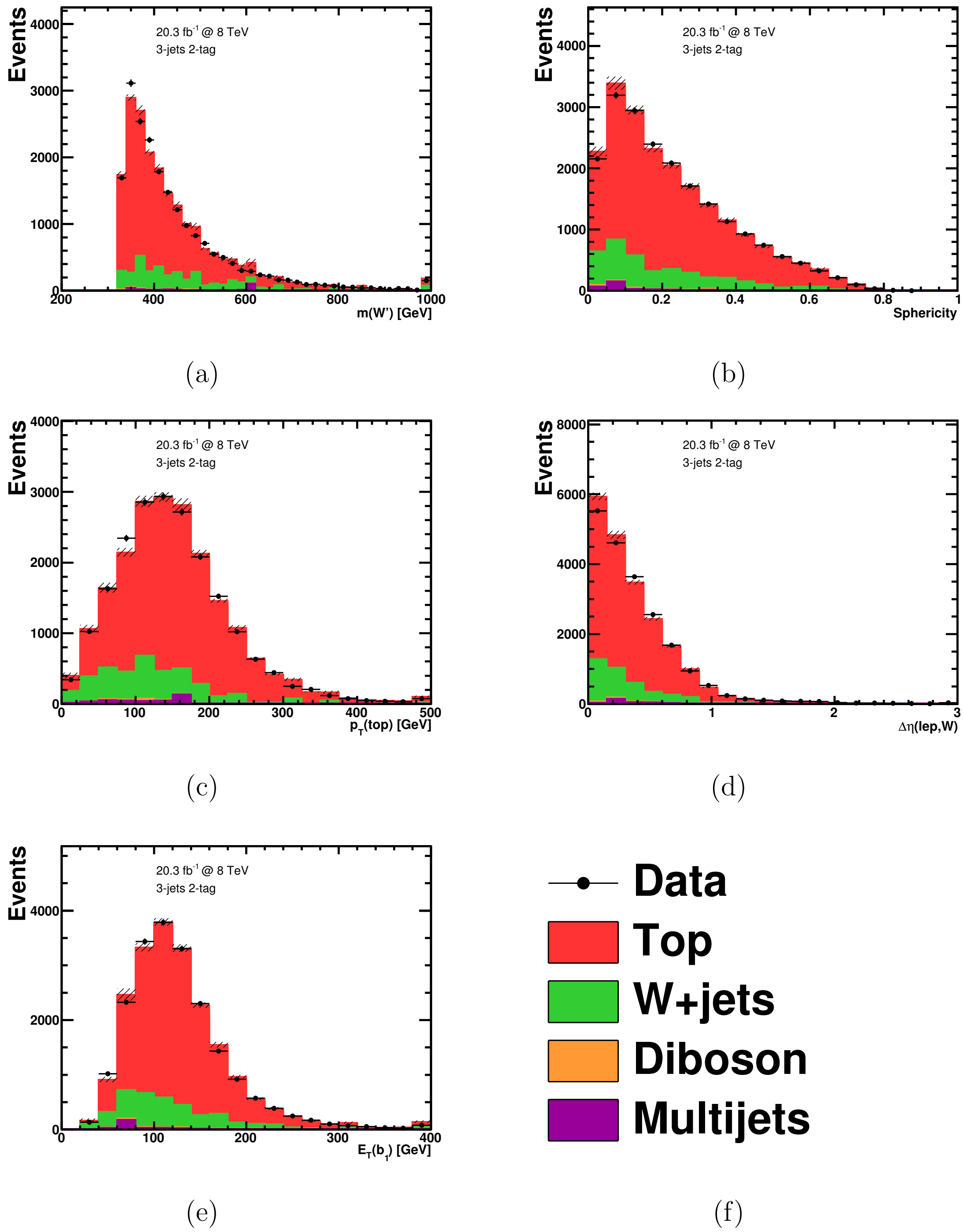

Figure 7.12: Comparison of data to Monte Carlo prediction of the 1st-5th variables by importance in the 3jet 2tag BDT.

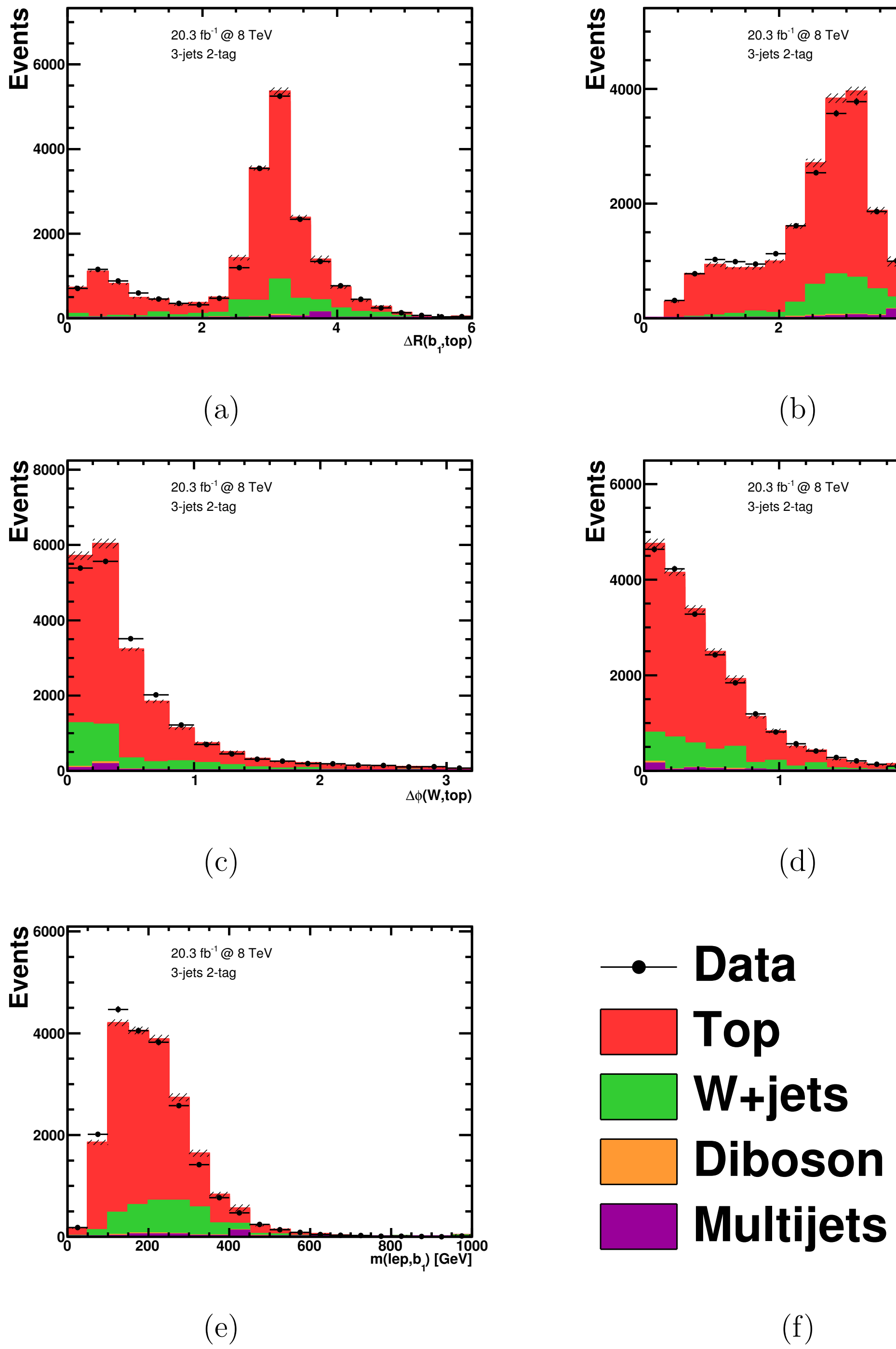

Figure 7.13: Comparison of data to Monte Carlo prediction of the 6th-10th variables by importance in the 3jet 2tag BDT.

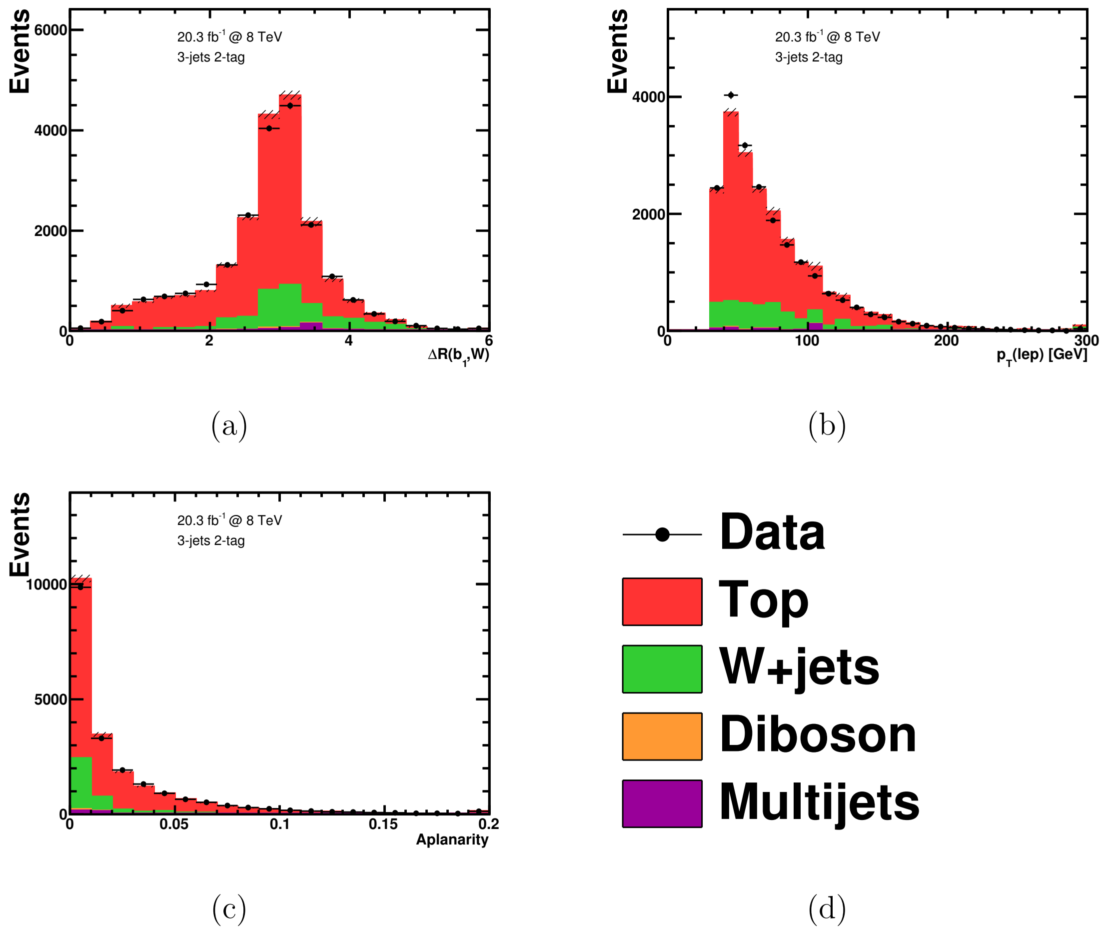

Figure 7.14: Comparison of data to Monte Carlo prediction of the 11th-13th variables by importance in the 3jet 2tag BDT.

7.1.3 BDT parameter optimization

The BDT parameters are the specific values used in the BDT training algorithm described in Section 7.1. These values have a strong impact on the resulting BDT and have a complicated relationship with the variables chosen for the BDT as well as any possible overtraining of the BDT. Because of this it is important to optimize these values but this is not a straight forward process. For each value of these parameters to be tested a new BDT must be trained which makes it computationally impractical to optimize the parameters simultaneously with the variable selection. Instead an iterative approach is taken, with each parameter value being optimized individually by scanning a range of values in discreet steps after the variable selection has been performed. An optimal parameter is chosen based on the BDT separation power after any overtrained trees have been removed. The variable selection and subsequent BDT parameter optimization are then redone if any parameter value changed by more than one step during the optimization. While it is possible for this method to get stuck in local optimizations, it has produced stable results with the available computational resources. A description of the parameters is provided below in the order they are optimized along with the initial training value of each parameter and the range and step size of the optimization scan. The final value of these parameters is provided in Table 7.2.

- **nTrees** is the number of individual decision trees to be trained by the BDT. This affects both the performance and possible overtraining of the BDT by allowing more degrees of freedom in the optimization. The range 60-200 is scanned with a step size of 20 and a default value of 120.

- **nEventsMin** is the minimum number of events for a decision node to be formed instead of a termination node. This affects the BDT performance and any possible

Parameter	2jets 1tag	3jets 1tag	2jets 2tag	3jets 2tag
nTrees	160	100	100	100
nEventsMin	200	200	180	200
maxDepth	10	10	8	8
AdaBoost	0.7	0.7	0.5	0.7
nCuts	10	12	14	12

Table 7.2: Optimized Boosted decision tree parameters for each of the four analysis channels.

overtraining by limiting how complex the individual decision trees can become. The range 100-300 is scanned with a step size of 20 and a default value of 200.

- **maxDepth** is the maximum decision depth of each decision tree in the BDT. Similar to nEventsMin, this affects the BDT performance and any possible overtraining by limiting how complex the individual decision trees can become. The range 6-12 is scanned with a step size of 1 and a default value of 9.

- **AdaBoost** is the boosting strength β in Equation 7.3. This primarily affects the performance of the BDT by adjusting how important the hard to classify events are. The range 0.4-1.0 is scanned with a step size of 0.1 and a default value of 0.7.

- **nCuts** is how many possible cuts are tested for each variable when determining the optimal cut for a decision node. This affects the BDT performance by ensuring the decision nodes have adequate granularity in their optimization. The range 8-16 is scanned with a step size of 2 and a default value of 12.

The figure of merit used to compare BDTs and determine the optimal variables and parameter configuration is ΔLLR, definded in Equation 7.6.

$$\Delta LLR = \sum_{BDT\ Bins} ln\left(1 + \frac{N_{Signal}}{N_{Background}}\right) N_{Signal} \tag{7.6}$$

Where N_{Signal} and $N_{Background}$ are the number of expected signal and background events in each bin. It is important to note that ΔLLR is not the same as the log-likelihood ratio (LLR) described in Section 8.2, but is an estimator of the LLR. It is necessary to use an estimator for the LLR due to computation time constraints. The BDT optimization iterates over many BDT configurations and the calculation of the LLR for a statstically stable number of pseudo-experiments, as described in Section 8.2, would take hours for each BDT tested, where as the calculation of ΔLLR takes seconds.

7.1.4 BDT output distributions

The BDT output distributions for the four analysis channels are shown in Figure 7.15. They show a clear separation of the signal and background processes and no signs of overtraining. Comparisons of the BDT output distributions of the data and background samples for the four analysis channels are shown with their statistical uncertainties in Figure 7.16. The statistical uncertainty is described in Section 8.1.16, and the distributions have an overall good agreement. Individual bins have small excesses or deficits of data compared to the background, and the 1tag analysis channels have a small overall data deficit as expected from the event yields given in Section 6.5.

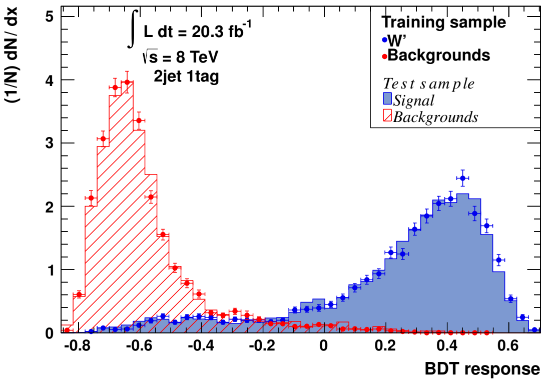

(a)

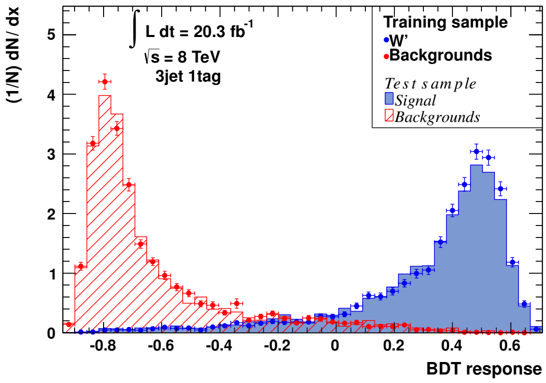

(b)

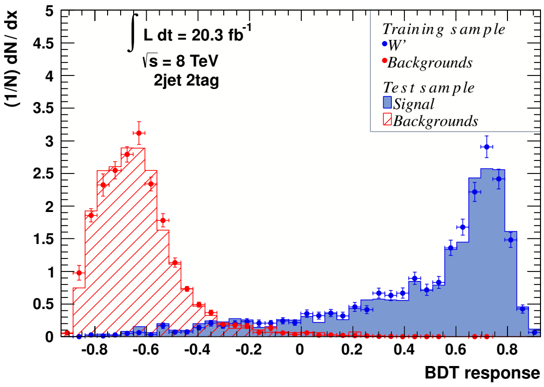

(c)

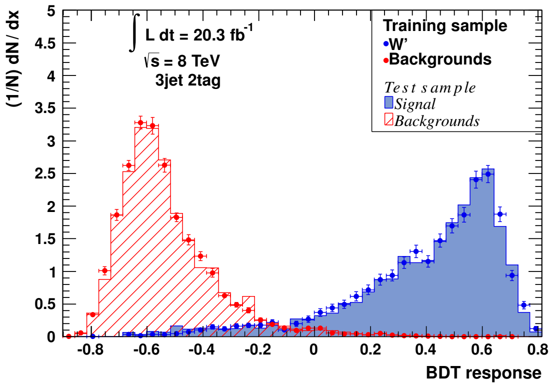

(d)

Figure 7.15: The BDT output distribution with the signal and background processes split into testing and training samples for (a) the 2jet 1tag analysis channel (b) the 3jet 1tag analysis channel (c) the 2jet 2tag analysis channel (d) the 3jet 2tag analysis channel.

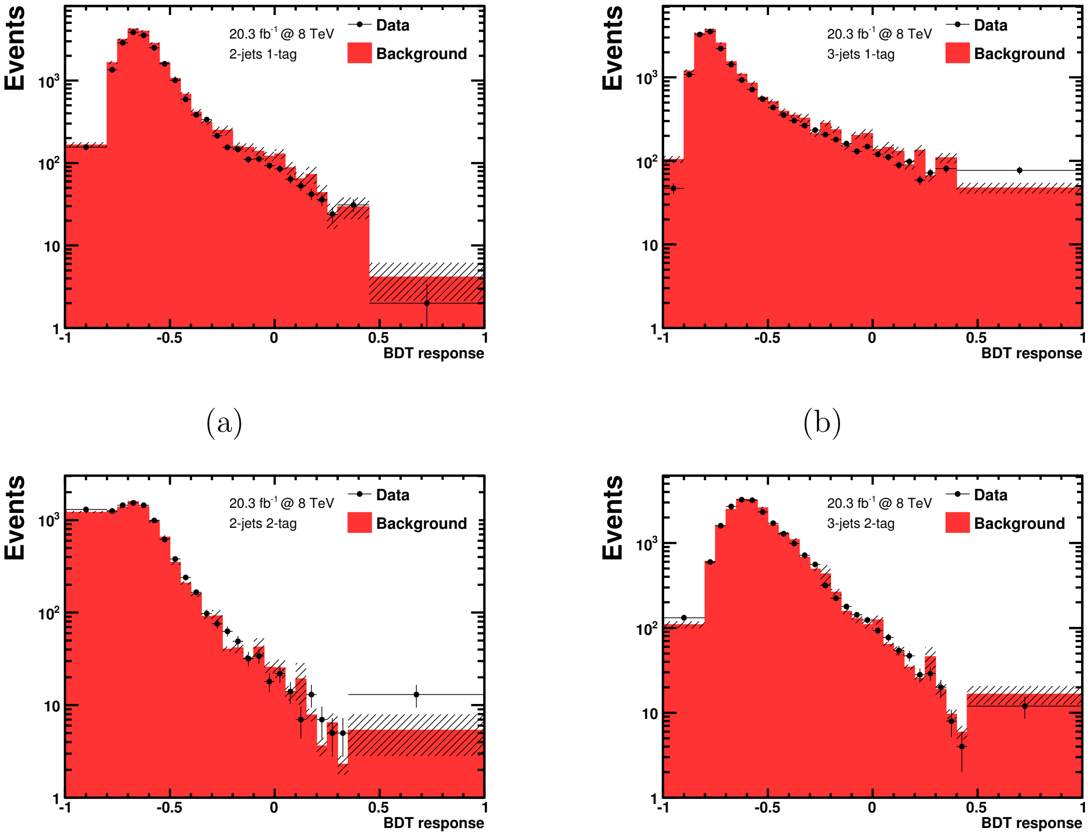

(a) (b) (c) (d)

Figure 7.16: The BDT output distribution of the background samples and data with statistical uncertainties for (a) the 2jet 1tag analysis channel (b) the 3jet 1tag analysis channel (c) the 2jet 2tag analysis channel (d) the 3jet 2tag analysis channel.

Chapter 8

Statistical analysis

With the separation of background and signal events optimized by the multivariate analysis (MVA) described in Chapter 7, the statistical significance of the analysis must be determined. Possible sources of systematic uncertainty and their effects are described in Section 8.1. With no statistically significant excess of events found by the analysis, 95% confidence level (C.L.) limits are placed on the cross-section times branching ratio of W' bosons with masses in the range 0.5 TeV - 3.0 TeV. The methodology used to derive these results is described in Section 8.2, and the results are given in Section 8.3.

8.1 Systematic uncertainties

ATLAS is a complicated experiment as described in Chapter 3, where the calibration and interpretation of the detector response from its many systems may introduce possible biases to the data. Additionally, the simulated Monte Carlo signal and background events may have biases in their generation and simulation which must be accounted for. The size of these potential biases are estimated using ATLAS perscribed procedures [73] and are treated as systematic uncertainties in the analysis. These uncertainties can be broadly categorized into shape uncertainties and rate uncertainties, with many of the uncertainty sources contributing to both types. Rate uncertainties can be easily described by their effect on the event yields but shape uncertainties cannot be so easily quantified because they move events between bins

	2jets 1tag		3jets 1tag	
Systematic Uncertainty	Signal	Background	Signal	Background
JES	-4.6/+4.7	+3.8/-4.0	-1.8/+2.0	+5.5/-5.3
JER	±2.5	±0.6	±0.8	±0.1
Jet Reconstruction	±0.1	±0.3	±0.1	±0.2
JVF	+3.5/-2.8	+2.2/-1.1	+3.5/-09	+0.9/-0.6
b-tagging	-0.7/-0.5	+6.6/+1.1	-2.0/+0.7	+5.9/+2.9
LES/LER	+0.1/-0.1	+0.4/-0.3	+0.1/-0.2	+0.4/-0.1
Lepton Efficiency	±0.9	±2.6	±0.4	±3.7
$E_{\mathrm{T}}^{\mathrm{miss}}$	-0.2/+0.0	+0.7/+0.7	-0.3/-0.3	+0.6/-0.9
PDF	±6.4	±2.1	± 7.7	±3.4
ISR/FSR	-	±1.4	-	±3.4
MC Generator	-	±2.0	-	±2.6
Theory Normalization	-	+1.0/-1.2	-	+2.4/-2.7
W+jets Normalization	-	+8.9/-7.7	-	+5.5/-4.8
Multijet Normalization	-	± 2.3	-	± 1.1
Luminosity	± 3.6	± 3.6	± 3.6	± 3.6

Table 8.1: Summary table of the systematic percentage shifts in the 1.75 TeV W'_R signal and background event yields of the 1tag analysis channels.

in an analysis channel. Tables 8.1 and 8.2 summarize the effects of the rate uncertainties on the background and signal event yields where the W'_R signal sample was generated at a mass of 1.75 TeV. For these tables, the size of uncertainties that contain multiple sources, such as Theory Normalization, are determined by adding the magnitude of the indiviual sources in quadrature. Each uncertainty is described in more detail below and is assessed on all of the signal and background samples except when the description specifies otherwise.

8.1.1 Jet energy scale (JES)

The jet energy scale (JES) is a rate and shape uncertainty. The JES uncertainty represents the potential bias in the measurement of the jet energies and includes both theoretical and experimental components. The theoretical components of the uncertainty come from the use of Monte Carlo simulations to derive the nominal JES correction factors for jets, while the

	2jets 2tag		3jets 2tag	
Systematic Uncertainty	Signal	Background	Signal	Background
JES	-4.1/+5.2	+0.2/-1.1	-2.2/+1.6	+1.1/-3.5
JER	±1.1	±0.1	±2.4	±0.9
Jet Reconstruction	±0.2	±0.3	±0.1	±0.1
JVF	+4.3/-2.6	+1.4/-2.9	+3.0/-1.5	+1.2/-1.1
b-tagging	+16.2/-14.9	+14.3/-4.7	+15.0/-14.0	+16.8/-7.0
LES/LER	+0.4/-0.1	+0.6/-0.5	+0.4/-0.1	+0.7/-0.6
Lepton Efficiency	±2.2	±2.0	±2.1	±4.2
$E_{\mathrm{T}}^{\mathrm{miss}}$	+0.4/+0.7	+0.4/-0.9	+1.0/+0.3	+0.6/+1.7
PDF	±7.7	±2.6	±8.2	±3.9
ISR/FSR	-	±4.0	-	±5.3
MC Generator	-	±6.1	-	±3.9
Theory Normalization	-	+2.8/-3.3	-	+3.7/-4.2
W+jets Normalization	-	+11.4/-11.3	-	+7.3/-7.2
Multijet Normalization	-	±2.0	-	±1.0
Luminosity	± 3.6	± 3.6	± 3.6	± 3.6

Table 8.2: Summary table of the systematic percentage shifts in the 1.75 TeV W'_R signal and background event yields of the 2tag analysis channels.

experimental components of the uncertainty come from an imperfect knowledge of the conditions a collision takes place in, such as the pileup. To estimate these uncertainties additional Monte Carlo samples are produced with varied simulation conditions and compared to data. In order to derive the JES calibration the energy of a jet is balanced in p_T against a reference object. This reference object can be a photon, a leptonically decaying Z boson, a jet in a different pseudorapidity region of the detector, or several jets with lower p_T. Each of these types of reference objects contributes to the overall calibration differently depending on the pseudorapidity and p_T of the jet. There are differences in jets that develop from gluons and the different quark flavors so an additional uncertainty is included in the JES uncertainty to account for the uncertainty in the exact flavor composition of the jets in the samples used to estimate the JES uncertainty. This flavor composition uncertainty contribution to the total JES uncertainty depends on the p_T, pseudorapidity, and flavor of the jet. The resulting total uncertainty in the jet energies is typically 0.5-3% [74]. The effects of the JES uncertainty on the W' search are evaluated by generating Monte Carlo samples with $+1\sigma$ and -1σ shifts in JES and applying the event selection and multivariate analysis to them. The difference in the resulting shifted BDT distributions from the nominal BDT distribution defines the $+1\sigma$ and -1σ uncertainty.

8.1.2 Jet energy resolution (JER)

The jet energy resolution (JER) is a rate and shape uncertainty. The JER uncertainty is the precision with which the energy of jets can be measured by the ATLAS detector. The JER uncertainty is estimated by measuring the p_T balance in dijet events, and ranges from 10 to 20% depending on the p_T of the jet [75]. In order to assess the effect of this resolution on the W' search Monte Carlo samples are generated with all of the jet energies modified by a random offset chosen using a Gaussian distribution with a standard deviation equal to the measured JER uncertainty. The event selection and multivariate analysis are applied to the modified samples, and the difference in the resulting shifted BDT distributions from the nominal BDT distribution defines the $+1\sigma$ and -1σ uncertainty.

8.1.3 Jet reconstruction efficiency

The jet reconstruction efficiency is a rate and shape uncertainty. The effects of the efficiency of the jet reconstruction algorithm on the W' search are estimated by randomly removing jets from the simulated events according to the jet reconstruction efficiency. This efficiency is determined by matching jets reconstructed from tracking information with jets reconstructed from the calorimeter. The jet reconstruction efficiency is over 99% given the event selection used in this analysis, although the reconstruction efficiency varies with the jet p_T. The modified sample has the event selection and multivariate analysis applied to it and half of the difference in the BDT weight distribution between the modified sample and nominal sample is taken as a symmetric uncertainty around the nominal values [76].

8.1.4 Jet vertex fraction (JVF)

The jet vertex fraction (JVF) is a rate and shape uncertainty. The JVF is the fraction of each jet's total p_T with tracks pointing to the event's primary vertex. This is a useful variable for removing pileup jets[1] and a cut is applied to the JVF for each jet as described in Section 4.3. The uncertainty in the efficiency of this cut is determined by taking the difference in cut values necessary to attain the same jet efficiency in data and Monte Carlo Z+jets samples, a difference of 0.03 in the JVF cut [77]. New Monte Carlo samples are produced with the JVF cut varied up and down from the nominal value by this uncertainty and these modified samples have the event selection and multivariate analysis applied to them to determine the effect on the BDT weight distribution. The difference in the resulting shifted BDT distributions from the nominal BDT distribution defines the $+1\sigma$ and -1σ uncertainty.

8.1.5 b-tagging performance

The b-tagging performance uncertainties are rate and shape uncertainties. The MV1 b-tagging algorithm is described in Section 4.3.1 and is central to the analysis for background

[1]Pileup jets are jets in an event which are created from in-time or out-of-time pileup effects. In-time pileup is an energy deposit in the calorimeter which has been mis-attributed to an event but is caused by a particle from another interaction occuring in the same bunch crossing. Out-of-time pileup is an energy deposit in the calorimeter which has been mis-attributed to an event but is caused by an interaction occuring in a different bunch crossing.

rejection and the definition of the analysis channels. The MV1 algorithm produces a value for each jet which a cut is applied to in order to achieve a 70% b-tagging efficiency. This is a complicated procedure and the overall uncertainty in the b-tagging performance is treated as three independant uncertainties: the b-tagging efficiency uncertainty, c-tagging efficiency uncertainty, and mis-tagging rate uncertainty. The b-tagging efficiency is the efficiency with which bottom quark initiated jets ("real" b-jets) are b-tagged, while the c-tagging efficiency is the efficiency with which charm quark initiated jets (c-jets) are b-tagged and the mis-tagging rate is the efficiency with which the remaining jets (light flavor jets) are b-tagged. The c-jets are treated seperately from the light flavor jets because c-jets are kinematically more similar to b-jets and thus much more likely to be b-tagged than light flavor jets. All three of these efficiencies are measured in data by applying the MV1 algorithm to analysis channels with high purities of b-jets, c-jets, and light flavor jets respectively. The uncertainties in the b-tagging efficiency, c-tagging efficiency, and mis-tagging rate are determined through careful consideration of the systematic and statistical uncertainties in the efficiency measurements, as described in the references [52, 78, 79]. The resulting uncertainties in the b-tagging of each jet depend on the p_T and pseudorapidity of the jet and the effects of these uncertainties are independently evaluated by reweighting the Monte Carlo events by $\pm 1\sigma$ shifts in each tagging efficiency. The difference in the resulting shifted BDT distributions from the nominal BDT distribution defines the three $+1\sigma$ and -1σ uncertainties.

8.1.6 Lepton energy scale and resolution

The lepton energy scale and resolution are both rate and shape uncertainties. The lepton energy scale and resolution uncertainties are determined by comparing $Z \to ll$ data and Monte Carlo events. The lepton energy scale is binned in E_T and pseudorapidity and the difference in the dilepton invariant mass peak between the data and Monte Carlo events in each bin determines the lepton energy scale uncertainty for that bin. The lepton energy resolution is not binned in E_T and pseudorapidity, instead the difference in the width of the dilepton invariant mass peak between the data and Monte Carlo events determines the uncertainty in the lepton energy resolution [80, 81]. The effects of the lepton energy scale uncertainty are evaluated by producing Monte Carlo samples with $+1\sigma$ and -1σ shifts in the lepton energy scale and applying the event selection and multivariate analysis to them. The effects of the lepton energy resolution are determined by modifying the nominal lepton energies by a random offset chosen using a Gaussian distribution with a standard deviation equal to the lepton energy resolution uncertainty and applying the event selection and multivariate analysis to the modified events.

8.1.7 Lepton trigger, reconstruction, and identification

The lepton trigger, reconstruction, and identification efficiency uncertainties are rate and shape uncertainties. The simulated Monte Carlo events are weighted by lepton trigger, reconstruction, and identification efficiencies measured in the $Z \rightarrow ll$ and $W \rightarrow l\nu$ channels. Chapter 4 describes the algorithms used to find electrons and muons for the analysis and defines what an electron or muon is at the analysis level. The lepton trigger efficiency is the efficiency with which the analysis level leptons pass the corresponding triggers, the leptons may not pass the trigger because the trigger system uses a more limited detector granularity and calibration than the analysis. The lepton reconstruction efficiency is the efficiency of analysis leptons being found by the lepton algorithms described in Chapter 4 up until the quality cuts. The lepton identification efficiency is the efficiency of analysis leptons passing the lepton quality cuts. Leptons may fail the reconstruction or identification algorithms in data due to temporarily noisy or dead cells in the detector which are not included in the Monte Carlo simulation. All three of these efficiencies are functions of the lepton kinematics and are determined by relaxing the respective requirements and measuring how often the trigger,reconstruction, or identification requirements are met. The uncertainty in these efficiencies is determined by taking half the difference in the measured data and Monte Carlo efficiencies as a symmetric uncertainty about the nominal value [80, 81].

8.1.8 Missing transverse energy ($E_{\mathrm{T}}^{\mathrm{miss}}$)

The $E_{\mathrm{T}}^{\mathrm{miss}}$ uncertainty is a rate and shape uncertainty. As described in Section 4.4, the $E_{\mathrm{T}}^{\mathrm{miss}}$ calculation contains terms for the leptons, jets, soft jets, and cell-out energy and the uncertainty in each of these terms is treated as an independant uncertainty. The effects of the uncertainty in the lepton or jet terms are included in the lepton and jet energy scale and resolution uncertainties described previously. The uncertainty in the soft jet and cell-out terms is estimated using a $Z \to \mu\mu$ sample with no jets having $p_T > 20$ GeV. The projection of the $E_{\mathrm{T}}^{\mathrm{miss}}$ onto the reconstructed Z boson's transverse direction is calculated for a data sample and Monte Carlo simulated sample. The average deviation from unity, defined as the ratio of this variable between the data and Monte Carlo samples, is taken as the uncertainty in the soft jets and cell-out energy [55]. New Monte Carlo samples are generated with the soft jets and cell-out callibrations independantly varied up and down by this uncertainty and the event selection and multivariate analysis are applied to these samples to evaluate the effect on the final BDT weight distribution.

8.1.9 Parton distribution function (PDF)

The parton distribution function (PDF) uncertainty is a rate uncertainty. PDFs are functions which give the probablility of a quark or gluon inside of a proton having some fraction of the proton's total momentum. PDFs are determined by fitting data from many particle physics experiments under a variety of assumptions about the functional form of the PDF. A PDF is used in Monte Carlo event generation to weight events with different initial quark or gluon momenta. The uncertainty in a PDF is expressed as a set of uncertainty eigenvectors, each of which represents the uncertainty in a single fit parameter. In order to estimate the effects of the PDF uncertainty on this analysis, the Monte Carlo samples are reweighted according to each of the 68% confidence level uncertainty eigenvectors for the CT10, MSTW2008NLO68CL [82], and NNPDF23 [83] PDFs. CT10 is the default PDF used for this analysis while MSTW and NNPDF are other common choices of PDFs. The uncertainty due to the PDF is covered by evaluating the uncertainty eigenvector sets of all three of these PDFs and taking half of the largest variation from the nominal sample yield is as a symmetric uncertainty on each Monte Carlo sample.

8.1.10 Initial state radiation and final state radiation (ISR/FSR)

The initial state radiation and final state radiation (ISR/FSR) uncertainty is a rate and shape uncertainty. ISR/FSR is the radiation of a particle immediately before or after the hard interaction of a process. The uncertainty in modeling these effects is estimated by varying the ISR/FSR settings of PYTHIA within the range consistent with previous measurements of $t\bar{t}$ [84]. Six additional $t\bar{t}$ samples are produced using ACERMC+PYTHIA with these varied ISR/FSR PYTHIA settings and have the event selection and multivariate analysis applied to them. The maximum deviation of the resulting BDT weight distributions from the nominal distribution is taken as a symmetric systematic uncertainty on the $t\bar{t}$ sample. This uncertainty is only evaluated for the $t\bar{t}$ sample because it is the largest background for the analysis and a large discrepency in $t\bar{t}$ predictions due to the ISR/FSR settings has been observed [84].

8.1.11 Monte Carlo event generator and parton showering

The different Monte Carlo event generator and parton showering programs make a variety of different approximations and produce events with different kinematic distributions. To reduce the analysis' sensitivity to the effects of a specific event generator or parton showering program a systematic uncertainty is included for all top quark processes which is estimated by taking the difference from the nominal Monte Carlo sample and a Monte Carlo sample produced with a different event generator or parton shower program. For the $t\bar{t}$ sample the nominal POWHEG+PYTHIA sample is compared to samples produced with POWHEG+HERWIG, MC@NLO+HERWIG, and ALPGEN+HERWIG and the largest difference is taken as a symmetric uncertainty. The nominal single top quark t-channel sample produced with ACERMC+PYTHIA is compared to a sample produced with MC@NLO+HERWIG and the difference between the samples is taken as a symmetric uncertainty. For the single top quark s-channel the nominal POWHEG+PYTHIA sample is compared to a sample produced with MC@NLO+HERWIG and the difference is taken as a symmetric uncertainty. For the single top quark Wt channel, the nominal POWHEG+PYTHIA sample is compared to a sample produced with MC@NLO+HERWIG and samples produced with POWHEG+PYTHIA with the two different NLO calculation schemes (diagram removal and diagram subtraction) are compared to each other, and the larger difference is taken as a symmetric uncertainty on the nominal sample. No event generator or parton showering systematic is evaluated for the W+jets or multijets backgrounds because they are estimated using data driven techniques.

8.1.12 Theoretical cross-sections

The theoretical cross-section uncertainties are rate uncertainties. All of the Monte Carlo samples, with the exception of the W+jets and multijets samples, are normalized to a theoretically predicted cross-section. These cross-sections have associated uncertainties in their calculation and each channel is assigned an independent rate uncertainty to account for this. The $t\bar{t}$ sample has a cross-section uncertainty of $-5.9/+5.1\%$. For the single top quark processes the uncertainty in the s-channel cross-section is $\pm 3.9\%$, the uncertainty in the t-channel cross-section is $-2.1/+3.9\%$, and the uncertainty in the Wt channel cross-section is $\pm 6.8\%$. The uncertainty in the Z+jets and diboson samples are calculated by adding in quadrature the 4% uncertainty in the inclusive process cross-section and a 24% uncerainty for each jet in the analysis channel. This gives an uncertainty in the Z+jets and diboson process cross-sections of 34% for the 2jet analysis channels and 42% for the 3jet analysis channels. The contributions of the Z+jets and diboson processes to the total background are small so this large uncertainty on their cross-sections has a small impact on the analysis.

8.1.13 W+jets normalization

The W+jets normalization uncertainty is a rate uncertainty. The W+jets Monte Carlo samples are normalized using a data driven technique described in Section 6.4.1. An uncertainty in this normalization is determined by individually applying the JES, event generator, parton showering, ISR/FSR, PDF, charge misidentification, lepton energy resolution, lepton trigger efficiency, lepton reconstruction efficiency, lepton identification efficiency, theoretical cross-section for other background processes and multijet normalization uncertainties described below to the control region used to derive the W+jets normalization. The variation in the W+jets normalization caused by each of these individual uncertainties is then added in quadrature to calculate the total W+jets normalization uncertainty. The total W+jets normalization uncertainty varies from 15% to 46% depending on the analysis channel and W+jets flavor.

8.1.14 Multijet normalization

The multijet normalization uncertainty is a rate only uncertainty. The multijet background is normalized using the matrix method as described in Section 6.4.2. Since this is a small background and a detailed estimation of the uncertainty in its normalization would be very difficult, a 50% uncertainty on the sample's normalization is applied.

8.1.15 Luminosity

There is a ±3.6% uncertainty in the luminosity of the data set used for this analysis, which is a preliminary result derived from updated van der Meer scans performed in April 2012 [85]. Since all of the Monte Carlo samples are normalized to this luminosity, this uncertainty is assessed as a ±3.6% rate uncertainty in all of the Monte Carlo samples except W+jets and multijets which are normalized using data driven techniques.

8.1.16 Monte Carlo statistics

The Monte Carlo statistical uncertainty is a rate and shape uncertainty. The finite number of Monte Carlo events generated for each process creates a statistical uncertainty in each bin of the BDT weight distribution. The statistical uncertainty in each bin is calculated taking into account the event weights of the Monte Carlo events and is less than 30% for the total background in each bin.

8.2 Limit setting procedure

The statistical analysis for the $W' \to t\bar{b}$ search uses the CL_S method [86, 87] implemented in the MClimit [88] software package. The CL_S method is a binned likelihood method, meaning the likelihood of each bin of the BDT weight distribution is computed and then all of the bins are combined into a global likelihood. This method was chosen because it is more powerful than a single bin counting experiment and is less sensitive to fluctuations in the background, as described below.

The CL_S method is derived from basic Poisson and Gaussian statistics. The likelihood of observing N events if there are μ expected events is given by Poisson statistics as:

$$\mathcal{L}(N|\mu) = \frac{\mu^N e^{-\mu}}{N!} \tag{8.1}$$

The inclusion of uncertainties into this likelihood is done by modifying the expected number of events through nuisance parameters (θ), each representing a single uncertainty. Each background or signal process forms a sample and the expected number of events for each sample (μ_i) is modified by the probability density function of each of the uncertainties that affect that sample (G). Depending on the hypothesis being tested, all of the background samples and possibly a signal sample are summed over to produce the final expected number of events as shown in Equation 8.2

$$\mu = \sum_{i \in sample} \mu_i \prod_{j \in uncertainty} G(\theta_{ij}, \delta_{ij}) \tag{8.2}$$

The probability density function for each of the uncertainties can in principle be any non-negative unitary distribution, but for this analysis they are all assumed to be Gaussian distributions with a mean of 1 and a standard deviation of δ. One of the consequences of Equation 8.2 is that μ is now a multi-dimensional probability distribution and not a single value.

So far this procedure has described a single counting experiment. Each bin of the BDT weight distribution can be treated as an independent counting experiment and the likelihood of observing an event distribution (N_{obs}) with N_k events in the k^{th} bin which has μ_k expected events is given by the product of the independent bins' likelihoods as shown in Equation 8.3.

$$\mathcal{L}(N_{obs}|\theta_{ij}, \delta_{ij}) = \prod_{k \in bins} \frac{{\mu_k}^{N_k} e^{-\mu_k}}{N_k!} \tag{8.3}$$

In order to determine if a signal process at a given mass point is excluded, 10,000 pseudo-experiments are generated for each of two hypotheses: one hyopthesis (H_1) includes the signal and all of the background processes while the other hypothesis (H_0) includes only the background processess. These pseudo-experiments are generated by randomly choosing a value for each nuisance parameter based on that parameter's probability distribution function. This shifted distribution is used to set the expected number of events of a Poisson distribution in each bin (μ_k). These Poisson distributions are then randomly sampled to produce the final pseudo-experiment distribution. For each pseudo-experiment the log-likelihood ratio (LLR) is computed according to Equation 8.4.

$$LLR = -2ln\left(\frac{\mathcal{L}(N_{obs}|H_1)}{\mathcal{L}(N_{obs}|H_0)}\right) \tag{8.4}$$

The LLR of the observed data set is also calculated and used to determine the strength of the limit on the signal process. CL_{S+B} is defined as the fraction of pseudo-experiments generated with the signal-plus-background hypothesis (H_1) with an LLR greater than the LLR of the data set. Similarly, CL_B is defined as the fraction of pseudo-experiments generated with the background-only hypothesis (H_0) with an LLR greater than that of the data set. CL_S is the likelihood of the signal being included in the data and is defined as the ratio of CL_{S+B} to CL_B as shown in Equation 8.5. An advantage of using CL_S rather than CL_{S+B} is that any mis-modeling or fluctuations in the background estimates will affect CL_{S+B} and CL_B similarly and will partially cancel when determining CL_S.

$$CL_S = \frac{CL_{S+B}}{CL_B} \tag{8.5}$$

A signal is excluded at the 95% confidence level if it has a $CL_S < 0.05$. After the signal has been excluded (or not) at its nominal cross-section the process is repeated with the normalization of the signal sample decreased (if the current cross-section was excluded) or increased (if the current cross-section was not excluded) by a factor k. This is iteratively repeated until CL_S equals 0.05. When this occurs the value of k can be used to determine the 95% limit on the cross-section as shown in Equation 8.6.

$$\sigma_{95\%\ limit} = k\sigma_{nominal} \tag{8.6}$$

This can be taken one step further and 95% confidence level limits can be placed on the coupling strengths g'_R and g'_L. The effective Lagrangian density used to generate the signal samples was given in Equation 2.13 and is repeated here in Equation 8.7.

$$\mathcal{L}_{W'} = \frac{1}{2\sqrt{2}} V'_{ij} W'_\mu \bar{f}^i \gamma^\mu (g'_R(1+\gamma_5) + g'_L(1-\gamma_5)) f^j \tag{8.7}$$

The cross-sections of the $W' \to t\bar{b}$ processes are thus proportional to g'^2_R or g'^2_L. The W'_R and W'_L signal samples at each mass point were generated with g'_R or g'_L equal to the Standard Model W coupling stength g. Thus the ratio of the observed limit on the cross-section to the nominal cross-section for the W'_R or W'_L signal sample at each mass point can be used to compute an equivalent limit on $\frac{g'_R}{g}$ or $\frac{g'_L}{g}$ respectively using Equation 8.8 at each mass point.

$$\sqrt{k} = \sqrt{\frac{\sigma_{95\%\ limit}}{\sigma_{nominal}}} = \frac{g'}{g} \tag{8.8}$$

8.3 Results

The limit setting procedure described in Section 8.2 is performed for each of the 22 W'_R and W'_L mass points (11 mass points each) in all four of the analysis channels (2jet 1tag, 2jet 2tag, 3jet 1tag, 3jet 2tag)[2]. These are not limits directly on the W' cross-section but instead they are limits on the W' cross-section corrected by the branching ration of $W' \to t\bar{b}$ and the branching ratio of $W \to l\nu$. The limits on cross-section times branching ratio for the W'_R mass points in each of the analysis channels are plotted in Figure 8.1, and the limits on

[2]It is necessary to compute the limits for each W' mass point seperately because the signal event kinematics, and thus the BDT responses, are different for each mass point.

Analysis Channel	Observed Mass Limit [TeV]	Expected Mass Limit [TeV]
2jet 1tag	1.51	1.47
3jet 1tag	1.66	1.61
2jet 2tag	1.72	1.73
3jet 2tag	1.68	1.71

Table 8.3: Expected and observed mass limits for a W'_R boson in the individual analysis channels.

cross-section times branching ratio for the W'_L mass points in each of the analysis channels are plotted in Figure 8.2. The red line in these plots shows the theoretical cross-section times branching ratio as a function of W' mass which is calculated assuming a coupling strength the same as in the SM. The solid black line shows the observed 95% confidence level limit on the cross-section times branching ratio as a function of W' mass. The region above this line has been excluded at the 95% confidence level and regions where the theoretical cross-section times branching ratio are above the observed limit have been excluded for g' $= g$. The dashed line is the expected limit, which is derived similarly to the observed limit but is the median result of 10,000 background only pseudo-data sets used in place of the data. The green and yellow bands are the 68% (1σ) and 95% (2σ) confidence interval of the expected limit results. The mass value where the theoretical cross-section times branching ratio crosses the observed or expected limit is known as the mass limit and is a commonly used figure of merit for exclusions such as this. The mass limits for each of the analysis channels is given in Table 8.3 for a W'_R boson and in Table 8.4 for a W'_L boson.

The limits on the cross-section times branching ratio can also be used to calculate limits on $\frac{g'}{g}$ as described by Equation 8.8. By using the observed or expected limits on the cross-section times branching ratio, observed or expected limits on $\frac{g'_R}{g}$ and $\frac{g'_L}{g}$ can be calculated for each of the tested mass points for the W'_R and W'_L bosons respectively. These limits

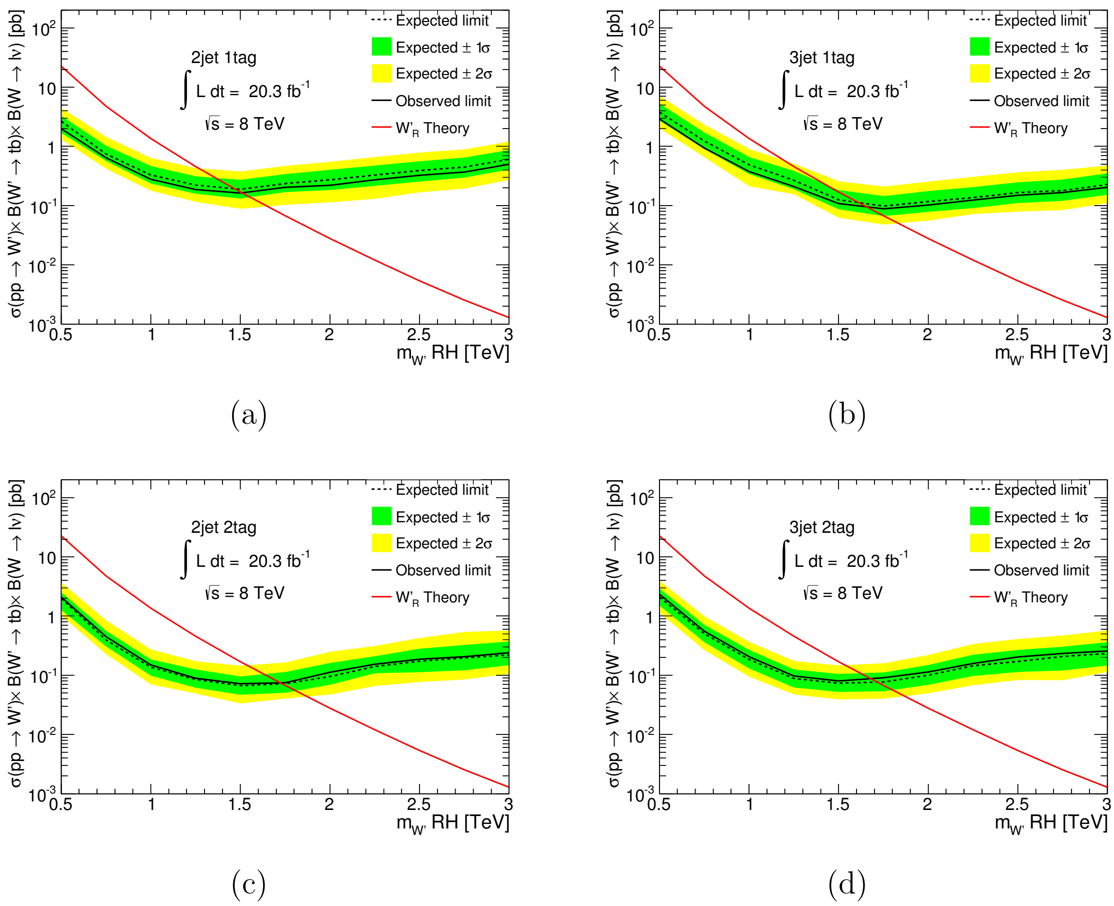

Figure 8.1: 95% confidence level limits on the cross-section times branching ratio of the W_R' boson in the (a) 2jet 1tag channel (b) 3jet 1tag channel (c) 2jet 2tag channel (d) 3jet 2tag channel.

Analysis Channel	Observed Mass Limit [TeV]	Expected Mass Limit [TeV]
2jet 1tag	1.48	1.44
3jet 1tag	1.62	1.58
2jet 2tag	1.59	1.63
3jet 2tag	1.57	1.60

Table 8.4: Expected and observed mass limits for a W_L' boson in the individual analysis channels.

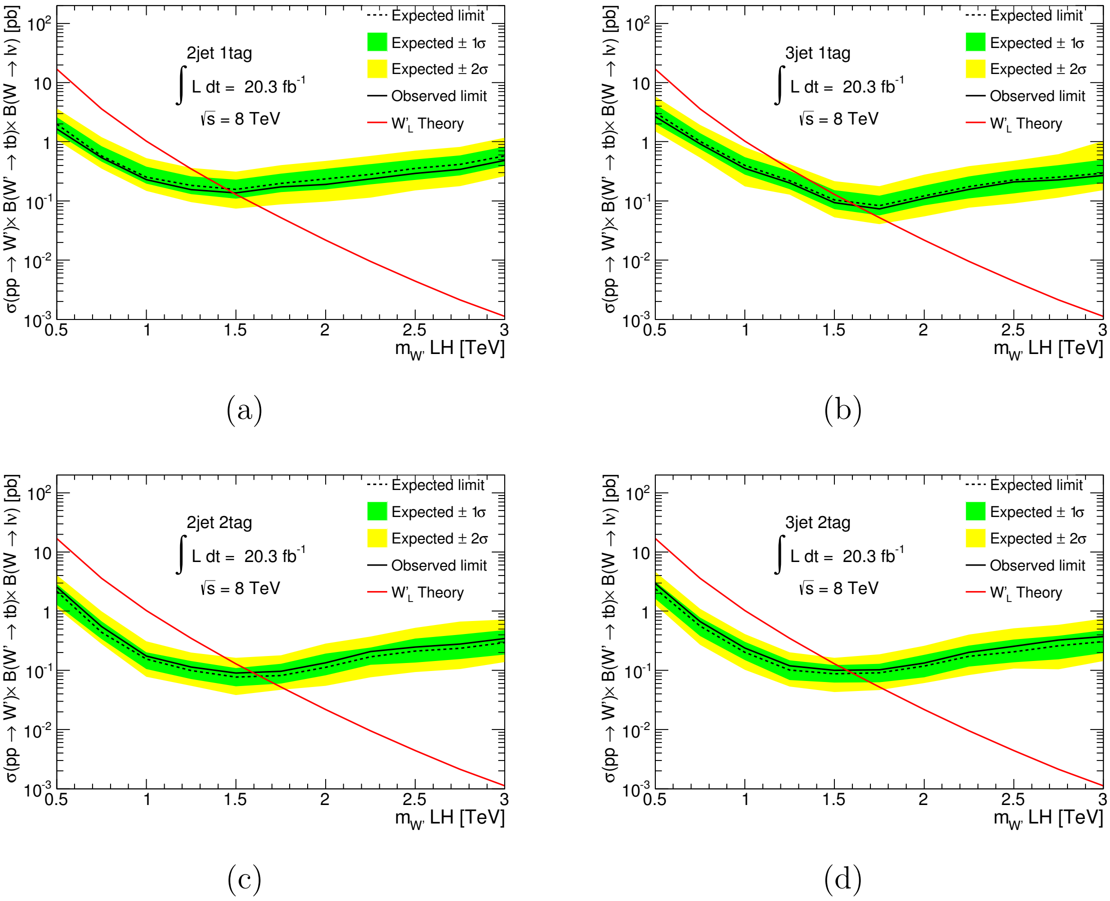

Figure 8.2: 95% confidence level limits on the cross-section times branching ratio of the W'_L boson in the (a) 2jet 1tag channel (b) 3jet 1tag channel (c) 2jet 2tag channel (d) 3jet 2tag channel.

are plotted as a function of the W' mass and an exclusion region is formed, as seen in Figures 8.3 and 8.4. These are limits on parameters in the effective Lagrangian density described in Equation 2.13, and they directly inform the excluded parameter space of theories that include a W' boson.

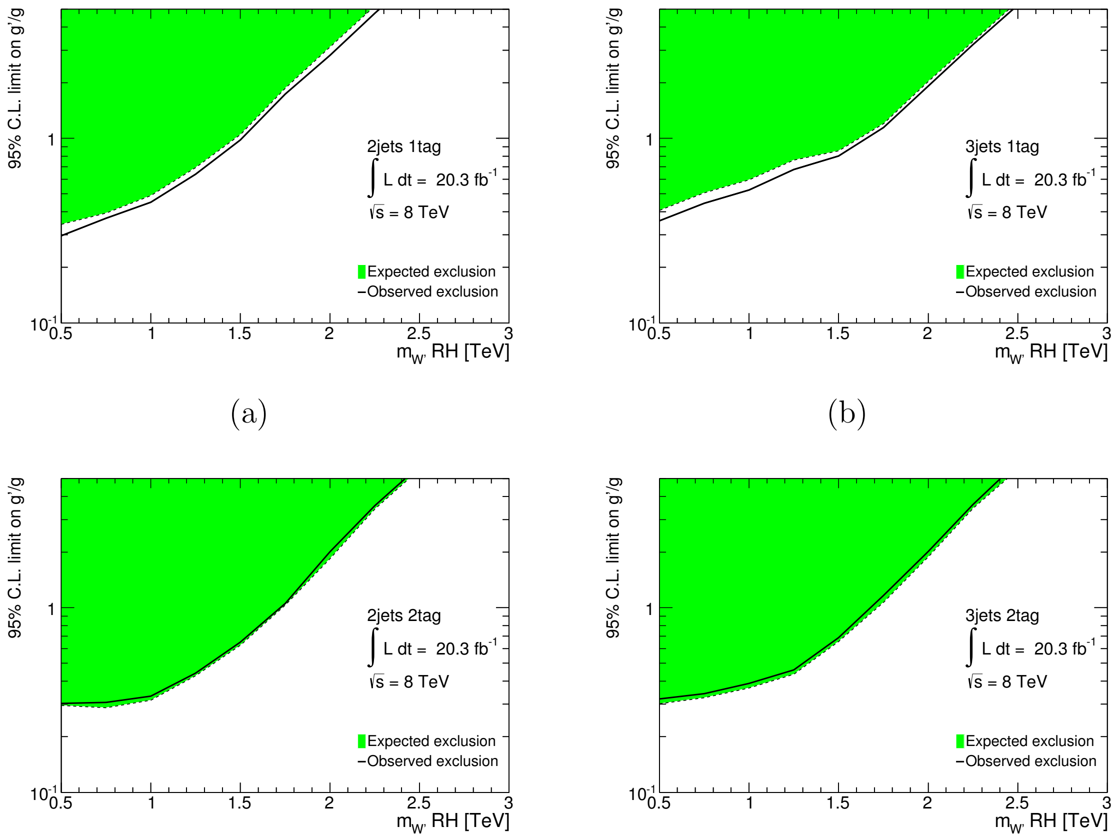

(a) (b) (c) (d)

Figure 8.3: 95% confidence level limits on $\frac{g'_R}{g}$ in the (a) 2jet 1tag channel (b) 3jet 1tag channel (c) 2jet 2tag channel (d) 3jet 2tag channel.

The individual analysis channels can also be combined by treating each channel as more bins in the BDT weight distribution. The resulting combination is analyzed in an identical manner to the individual analysis channels and similar limits can be made. Because of their kinematic similarities, the 2jet 1tag and 3jet 1tag channels are combined to form the

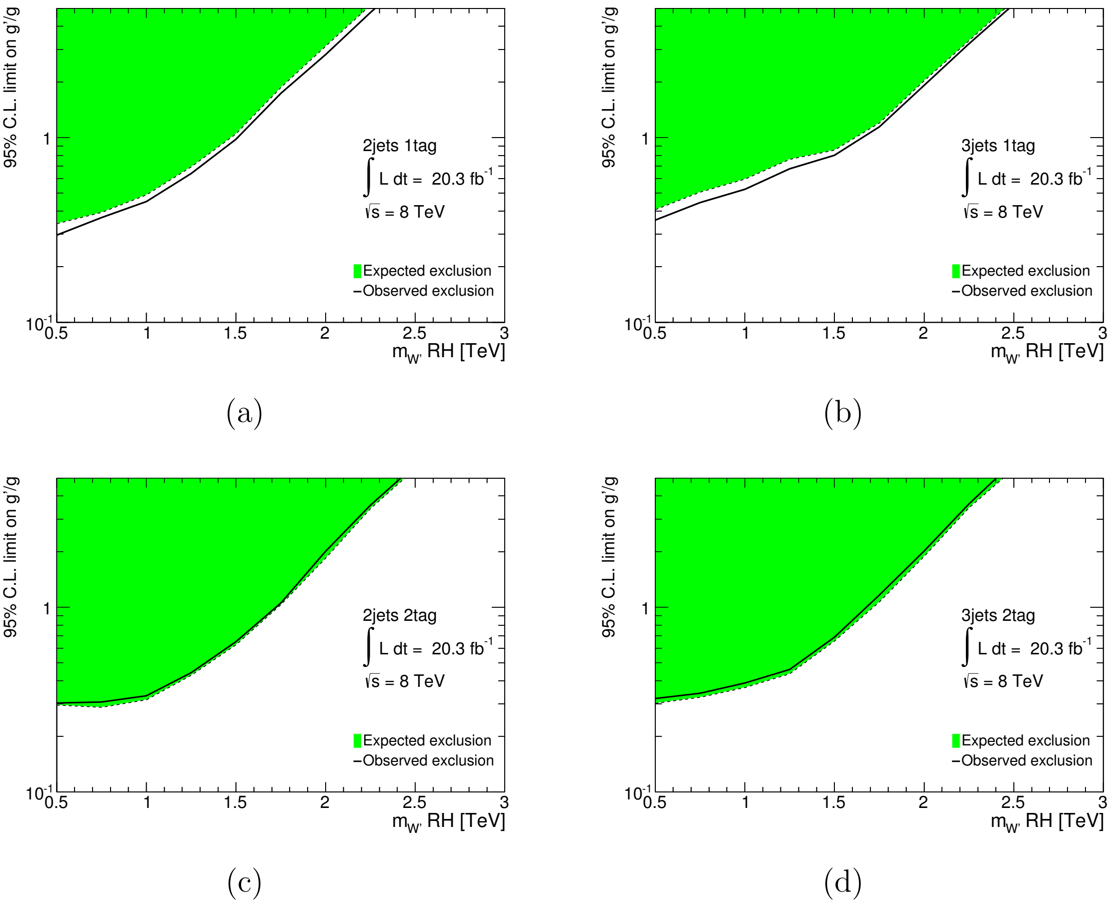

(a) (b) (c) (d)

Figure 8.4: 95% confidence level limits on $\frac{g'_L}{g}$ in the (a) 2jet 1tag channel (b) 3jet 1tag channel (c) 2jet 2tag channel (d) 3jet 2tag channel.

1tag combined channel, and the 2jet 2tag and 3jet 2tag channels are combined to form the 2tag combined channel. A final combination of all of the analysis channels forms the full combination channel. The limits on the cross-section times branching ratio for a W'_R and W'_L boson are shown in Figure 8.5 and 8.6 respectively. The derived mass limits from the combined channels for a W'_R or W'_L boson are given in Tables 8.5 and 8.6. The limits on $\frac{g'_R}{g}$ and $\frac{g'_L}{g}$ are shown in Figures 8.7 and 8.8.

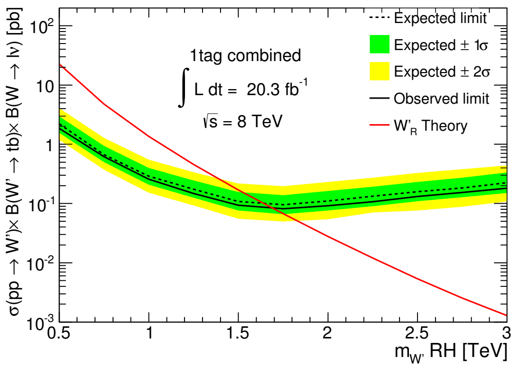

(a)

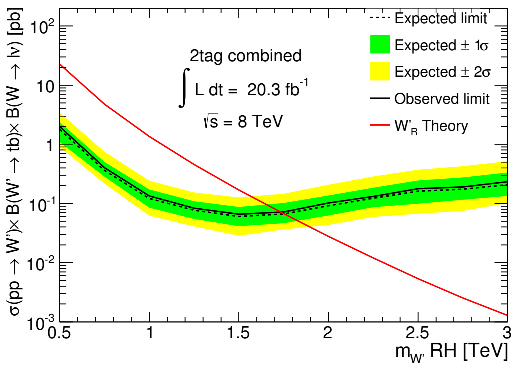

(b)

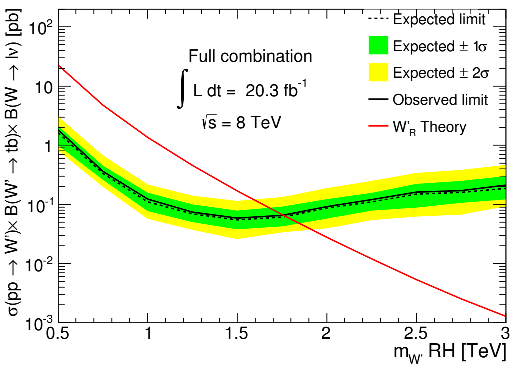

(c)

Figure 8.5: 95% confidence level limits on the cross-section times branching ratio of the W'_R boson in the (a) 1tag combined channel (b) 2tag combined channel (c) full combination channel.

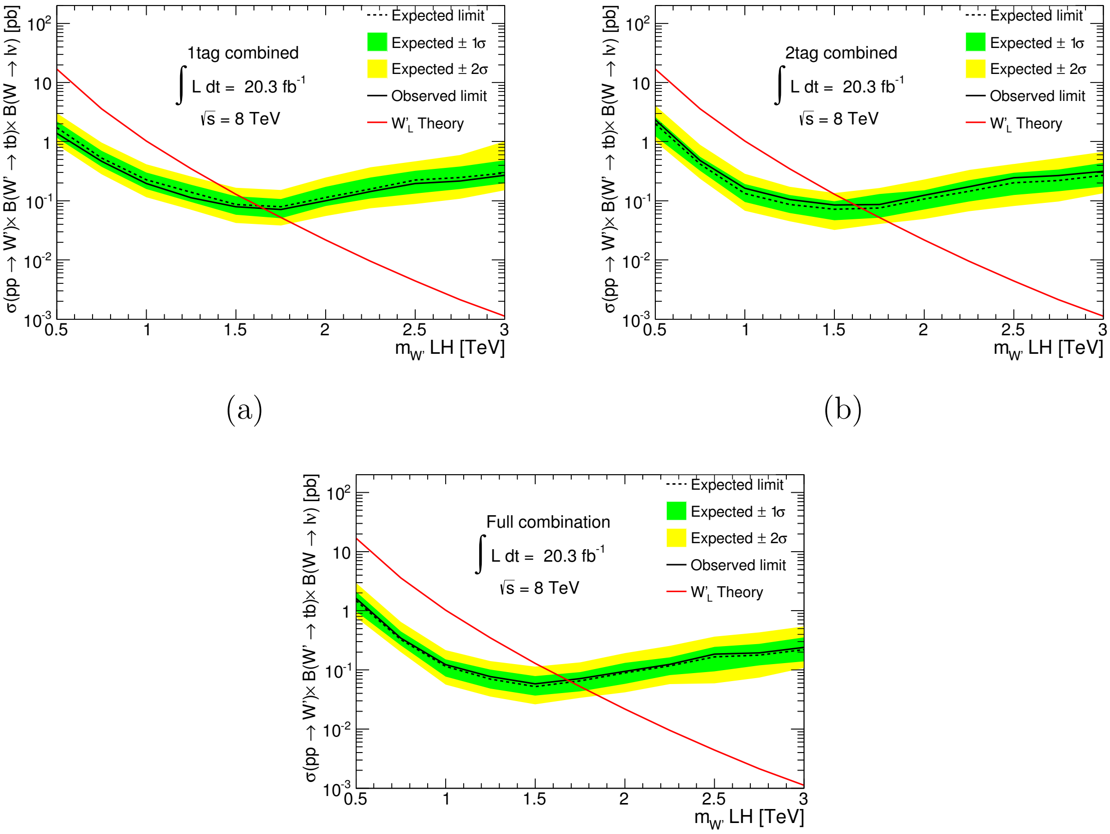

(a) (b)

(c)

Figure 8.6: 95% confidence level limits on the cross-section times branching ratio of the W'_L boson in the (a) 1tag combined channel (b) 2tag combined channel (c) full combination channel.

Analysis Channel	Observed Mass Limit [TeV]	Expected Mass Limit [TeV]
1tag combined	1.69	1.64
2tag combined	1.73	1.75
full combination	1.76	1.77

Table 8.5: Expected and observed mass limits for a W'_R boson in the combined analysis channels.

Analysis Channel	Observed Mass Limit [TeV]	Expected Mass Limit [TeV]
1tag combined	1.65	1.62
2tag combined	1.61	1.65
full combination	1.68	1.70

Table 8.6: Expected and observed mass limits for a W'_L boson in the combined analysis channels.

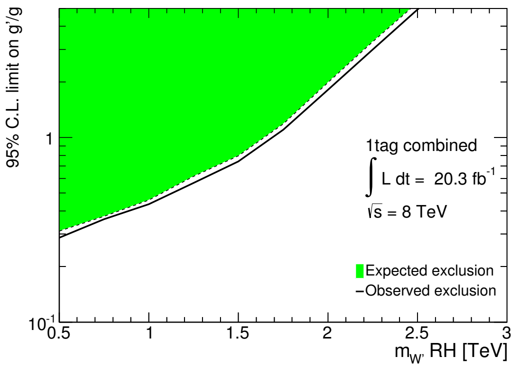

(a)

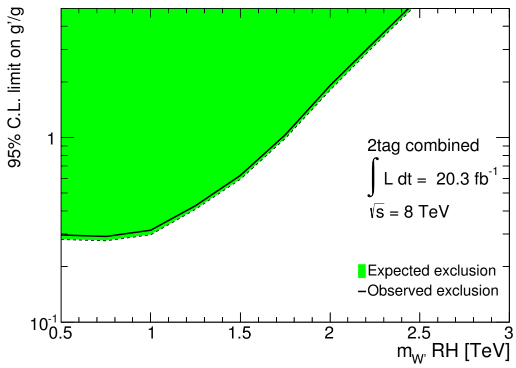

(b)

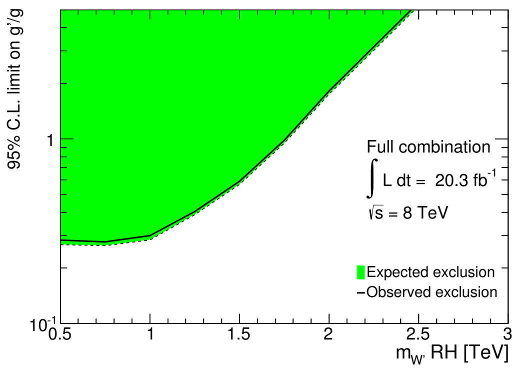

(c)

Figure 8.7: 95% confidence level limits on $\frac{g'_R}{g}$ in the (a) 1tag combined channel (b) 2tag combined channel (c) full combination channel.

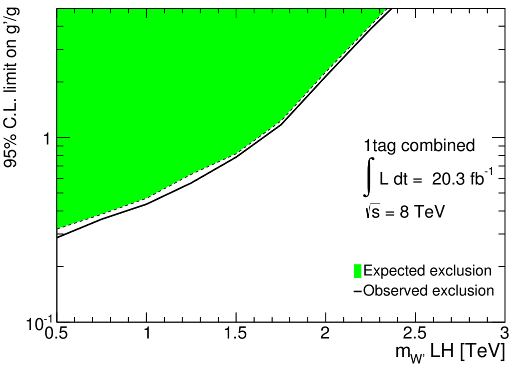

(a)

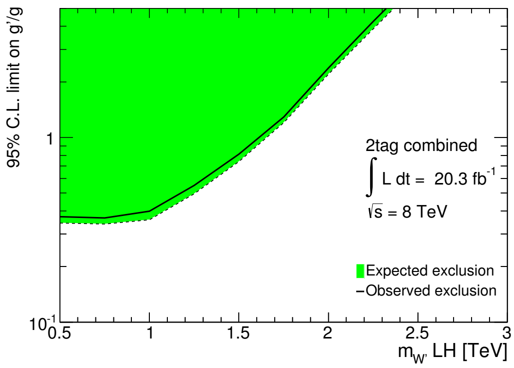

(b)

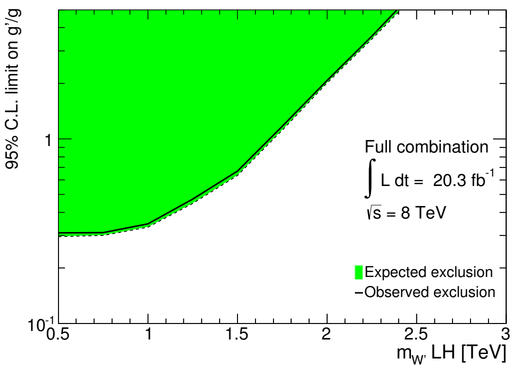

(c)

Figure 8.8: 95% confidence level limits on $\frac{g'_L}{g}$ in the (a) 1tag combined channel (b) 2tag combined channel (c) full combination channel.

Experiment	Observed Mass Limit [TeV]	Luminosity	Collision Energy	Reference
This analysis	1.76	20.3 fb^{-1}	8 TeV	-
CDF (2014)	0.84	9.1 fb^{-1}	1.96 TeV	[89]
D0 (2011)	0.89	2.3 fb^{-1}	1.96 TeV	[24]
ATLAS (2013)	1.84	14.3 fb^{-1}	8 TeV	[90]
CMS (2014)	2.05	19.5 fb^{-1}	8 TeV	[26]

Table 8.7: Observed mass limits for a W'_R boson from different experiments

Experiment	Observed Mass Limit [TeV]	Luminosity	Collision Energy	Reference
This analysis	1.68	20.3 fb^{-1}	8 TeV	-
D0 (2011)	0.86	2.3 fb^{-1}	1.96 TeV	[24]
ATLAS (2013)	1.74	14.3 fb^{-1}	8 TeV	[90]
CMS (2014)	2.05	19.5 fb^{-1}	8 TeV	[26]

Table 8.8: Observed mass limits for a W'_L boson from different experiments

8.4 Comparison with other experiments

This analysis is not the first search for $W' \rightarrow t\bar{b}$, there have been similar searches done previously by the CDF and D0 collaborations at the Tevatron as well as previous results from the CMS and ATLAS collaborations at the LHC. None of these experiments have obseved a W' signal and the mass limit set on the W' boson by these searches is given in Table 8.7 for a W'_R and in Table 8.8 for a W'_L.

This analysis does not set new best limits on the allowed mass of either a W'_R or W'_L boson. The inclusion of the 1tag analysis channels does not significantly improve the sensitivity of the analysis above that of the combination of the 2tag analysis channels. This is surprising given that previous analyses at the Tevatron [23, 24] saw an increase in sensitivity from the inclusion of 1tag events. The most recent result from the CMS collaboration [26] also includes 1tag events although it is unclear how much of the sensitivity comes from the 1tag events since they are not analyzed seperately from the 2tag events. Attempts to replicate the CMS analysis with ATLAS data have not shown an improvement over this analysis. This analysis also does not represent a large improvement over the previous ATLAS result [90] despite analyzing a larger dataset, which could indicate that the analysis sensitivity is limited by systematic uncertainties.

Chapter 9

Conclusion

This analysis is a search for $W' \to t\bar{b}$ using the ATLAS detector. The discovery of such a particle would revolutionize particle physics, and while no such particle was found by this analysis the limits placed on the possible existence of such a particle provides information that affects a wide range of new physics theories.

This analysis uses the entire 8 TeV dataset collected by ATLAS in 2012 and is the first inclusion of events with a single b-tag into a $W' \to t\bar{b}$ search at ATLAS. The sensitivity of the search is limited by systematic uncertainties. These systematic uncertainties will almost certainly improve with time as the ATLAS program matures and the detector and the physics it probes is better understood, but there is ample room for improvement in the analysis technique itself. This analysis uses a boosted decision tree (BDT) algorithm to increase the sensitivity of the analysis to a potential signal. Such a method optimizes the analysis of the nominal sample but the optimization is blind to the potential impact of systematic uncertainties. A modification of the BDT algorithm to take into account the systematic uncertainties and potentially trade some separation power in the nominal sample for an increased robustness against the effects of systematic uncertainties could improve not only this analysis but a large number of analyses which are currently limited by the effects of systematic uncertainties. The inclusion of such a modification to this analysis is discussed in Appendix A, but it did not improve the expected sensitivity of the analysis and was not included in the final result.

Even without such an improvement in the analysis technique or a large reduction in systematics, I expect new searches for $W' \to t\bar{b}$ to be able to reach much higher energies in the near future. With the resumption of data taking at the LHC in 2015 planned to take place with 13 or 14 TeV collisions, the production rate of high mass W' bosons will be up to 50 times higher than what was expected at 8 TeV [91]. Ongoing research [92] suggests that at such high energies searching for the hadronic decay of the $W^{\pm}$ boson may produce an analysis more sensitive to a higher mass W' boson than the leptonic decay this analysis searches for. Such future analyses, whether they be in a hadronic or leptonic channel, will doubtless present their own hurdles for future analyzers to overcome.

APPENDIX

Alternative BDT Configurations

The multivariate analysis described in Chapter 7 was the result of many trials and attempts to improve the sensitivity of the analysis. It offers the best sensitivity while minimizing the complexity of the analysis, but many more complex and less sensitive configurations of the multivariate analysis were investigated during the development of this analysis. It is useful to document these alternative configurations not only to avoid a duplication of effort but also to provide insight and possibly inspiration. In this appendix, two categories of alternative configurations are described: alternative figures of merit for the BDT, and the inclusion of systematic uncertainties into the BDT optimization. The alternative figures of merit for the BDT are replacements for ΔLLR when optimizing the BDT parameters as described in Section 7.1.3. A method of including systematic uncertainties into the BDT is a modification of the method of evaluating the BDT figure of merit described in Section 7.1.3 with the goal of reducing the effects of systematic uncertainties on the final results. The development of the multivariate analysis occured in parallel with the development of the other parts of the analysis, and fully documenting the differences in the analysis when different portions of these studies were performed is beyond the scope of this appendix. Because of this there are no consistent figures of merit across all of the studies and only qualitative claims are made about the performance of the various methods tested.

A.1 Alternative BDT figures of merit

The statistical method described in Section 8.2 is very computationally intensive, and it is not feasible to perform such an analysis on a large number of BDT trainings in order to determine parameter settings which optimise the expected sensitivity of the analysis. Instead it is necessary to use a more computationally simple estimator of the expected sensitivity in order to determine the optimal BDT parameter values. The optimization of the BDT parameters described in Section 7.1.3 uses ΔLLR as the figure of merit for choosing the best BDT parameters because it is an estimator of the figure of merit used in the statistical analysis (LLR), and because its optimal BDT parameterization was more sensitive than the optimal BDT parameterization of any other figures of merit when the statistical analysis was performed on those results. The alternative figures of merit which were investigated are described below:

- **Optimal Cut Significance:** The optimal cut significance is determined by finding the cut on the BDT output which maximizes $\frac{S}{\sqrt{S+B}}$ where S is the number of signal events above the cut value and B is the number of background events above the cut value. This estimates the expected significance of a counting experiment and does not include any information of the distribution shapes except in the placement of the optimal cut. This performed only slightly worse than ΔLLR.

- **Signal and Background Peak Separation:** The signal and background peak separation is the difference in the BDT output values of the peak of the signal distribution and the background distribution. This estimates the separation between the signal and background event distributions. It performed much worse than ΔLLR.

- **Significance above the Signal Peak:** The significance above the signal peak is determined by calculating $\frac{S}{\sqrt{S+B}}$ for events at and above the signal peak. This estimates the expected significance of a counting experiment. It performed slightly worse than ΔLLR and approximately as well as the optimal cut significance.

A.2 Inclusion of systematic uncertainties

A potential weakness of the BDT optimization strategy is that an algorithm is created which optimally sorts the nominal background and signal samples but which is very sensitive to systematic shifts in the variables used to sort the events. In such a situation it may be possible to find an algorithm that less optimally sorts the nominal events but is less sensitive to systematic shifts in the variables used and is more sensitive than the optimal nominal algorithm after the systematic uncertainties are taken into account in the statistical analysis. Attempts were made to develop such an algorithm by modifying the way the BDT figure of merit was evaluated to include information about the systematically shifted event samples.

The BDT was trained with the nominal event sample and then applied to the nominal event sample as well as the systematically shifted event samples. The BDT figure of merit was then evaluated for the nominal sample output as well as the systematically shifted sample outputs and the minimum of these figures of merit was taken as the figure of merit for that BDT training. Optimizations were performed with as few as one systematically shifted sample included up to all of the systematically shifted samples being included, for all of the figures of merit listed in Section A.1. None of the BDT trainings which included systematically shifted samples out-performed the BDT trained with only the nominal event sample. In general the more systematically shifted samples were included in the optimization the worse the resulting BDT performed, with trainings that only included one systematically shifted sample having little or no differences from the training that included only the nominal event sample.

BIBLIOGRAPHY

BIBLIOGRAPHY

[1] J. Beringer and et al. (Particle Data Group) Phys. Rev. D86 **86** (2012) 010001, `2013 partial update for the 2014 edition.`

[2] *Expected electron performance in the ATLAS experiment*, Tech. Rep. ATL-PHYS-PUB-2011-006, CERN, Geneva, Apr, 2011.

[3] D. Duffty and Z. Sullivan, *Model independent reach for W-prime bosons at the LHC*, Phys. Rev. **D86** (2012) 075018, `arXiv:1208.4858 [hep-ph]`.

[4] AAAS, *The Standard Model*, 2012.

[5] J.-L. Caron, *Accelerators chain of CERN : operating and approved projects*, Sep, 2001.

[6] J. Pequenao, *Computer generated image of the whole ATLAS detector*, Mar, 2008.

[7] ATLAS Collaboration, *The ATLAS Experiment at the CERN Large Hadron Collider*, JINST **3** (2008) S08003.

[8] J. Pequenao, *Computer generated image of the ATLAS inner detector*, Mar, 2008.

[9] J. Pequenao, *Computer Generated image of the ATLAS calorimeter*, Mar, 2008.

[10] J. Pequenao, *Computer generated image of the ATLAS Muons subsystem*, Mar, 2008.

[11] J. Pequenao and P. Schaffner, *An computer generated image representing how ATLAS detects particles*, Jan, 2013.

[12] on behalf of the ATLAS collaboration Collaboration, A. Coccaro, *Track Reconstruction and b-Jet Identification for the ATLAS Trigger System*, Tech. Rep. arXiv:1112.0180. ATL-DAQ-PROC-2011-051, CERN, Geneva, Dec, 2011. Comments: 7 pages, 10 figures, conference proceedings for ACAT 2011.

[13] D. Griffiths, *Introduction to Elementary Particles.* Wiley-VCH Verlag GmbH & Co. KGaA, Weinheim, 2004.

[14] E. M. Henley and A. Garcia, *Subatomic Physics*. World Scientific Publishing Co. Pte. Ltd., 2007.

[15] C. Itzykson and J.-B. Zuber, *Quantum Field Theory*. McGraw-Hill, Inc., 1980.

[16] L. H. Ryder, *Quantum Field Theory*. Press Syndicate of the University of Cambridge, 2006.

[17] (Super-Kamiokande Collaboration) Collaboration, *Evidence for Oscillation of Atmospheric Neutrinos*, Phys. Rev. Lett. **81** (1998) 1562–1567.

[18] [ATLAS Collaboration] Collaboration, G. Aad et al., *Observation of a new particle in the search for the Standard Model Higgs boson with the ATLAS detector at the LHC*, Phys. Lett. B **716** (2012) 1, `arXiv:arXiv:1207.7214 [hep-ex]`.

[19] [CMS Collaboration] Collaboration, S. Chatrchyan et al., *Observation of a new boson at a mass of 125 GeV with the CMS experiment at the LHC*, Phys. Lett. B **716** (2012) 30, `arXiv:arXiv:1207.7235 [hep-ex]`.

[20] R. N. Mohapatra and J. C. Pati, *Left-Right Gauge Symmetry and an Isoconjugate Model of CP Violation*, Phys.Rev. **D11** (1975) 566–571.

[21] K. Babu, X.-G. He, and E. Ma, *New Supersymmetric Left-Right Gauge Model: Higgs Boson Structure and Neutral Current Analysis*, Phys.Rev. **D36** (1987) 878.

[22] H. Georgi, E. E. Jenkins, and E. H. Simmons, *The un-unified standard model*, Nuclear Physics B **331** (1990) no. 3, 541 – 555.
`http://www.sciencedirect.com/science/article/pii/055032139090083P`.

[23] CDF Collaboration Collaboration, T. Aaltonen et al., *Search for the Production of Narrow t anti-b Resonances in 1.9 fb-1 of p anti-p Collisions at s**(1/2) = 1.96-TeV*, Phys.Rev.Lett. **103** (2009) 041801, `arXiv:0902.3276 [hep-ex]`.

[24] D0 Collaboration Collaboration, V. M. Abazov et al., *Search for $W' \to tb$ resonances with left- and right-handed couplings to fermions*, Phys.Lett. **B699** (2011) 145–150, `arXiv:1101.0806 [hep-ex]`.

[25] ATLAS Collaboration Collaboration, G. Aad et al., *Search for tb resonances in proton-proton collisions at $\sqrt{s} = 7$ TeV with the ATLAS detector*, Phys.Rev.Lett. **109** (2012) 081801, `arXiv:1205.1016 [hep-ex]`.

[26] CMS Collaboration Collaboration, S. Chatrchyan et al., *Search for W' to tb decays in the lepton + jets final state in pp collisions at $\sqrt{s}$ = 8 TeV*, `arXiv:1402.2176 [hep-ex]`.

[27] E. Boltezar, H. Haseroth, W. Pirkl, T. Sherwood, U. Tallgren, P. Tetu, D. Warner, and M. Weiss, *The New CERN 50MeV Linac*, Proc. 1979 Linear Accelerator Conference **BNL 51134** (1979) no. 66, .

[28] B. Mikulec, A. Blas, C. Carli, A. Findlay, K. Hanke, G. Rumolo, and J. Tan, *LHC Beams from the CERN PS Booster*, .

[29] M. Barnes, M. Benedikt, E. W. Blackmore, A. Blas, J. Borburgh, R. Cappi, M. Chanel, V. Chohan, F. Cifarelli, G. Clark, G. Daems, L. R. Evans, A. B. Fowler, R. Garoby, J. Gonzlez, D. G. Grier, J. Gruber, S. Hancock, C. E. Hill, A. Jansson, E. Jensen, S. R. Koscielniak, A. Krusche, R. Losito, P. Maesen, F. Mammarella, K. D. Metzmacher, A. Mitra, J. Olsfors, M. Paoluzzi, J. Pedersen, R. Poirier, U. Raich, K. W. Reiniger, T. C. Ries, J. P. Riunaud, J. P. Royer, M. Sassowsky, K. Schindl, H. O. Schnauer, L. Sermeus, M. Thivent, H. M. Ullrich, W. Van Cauter, M. Vretenar, and F. V. Vlker, *The PS complex as proton pre-injector for the LHC: design and implementation report*. CERN, Geneva, 2000.

[30] P. Collier and B. Goddard, *PREPARATION OF THE SPS AS LHC INJECTOR*. CERN, Geneva, 1998.

[31] O. S. Brning, P. Collier, P. Lebrun, S. Myers, R. Ostojic, J. Poole, and P. Proudlock, *LHC Design Report*. CERN, Geneva, 2004.

[32] ATLAS Collaboration Collaboration, *ATLAS detector and physics performance: Technical Design Report, 1*. Technical Design Report ATLAS. CERN, Geneva, 1999. Electronic version not available.

[33] ATLAS Collaboration Collaboration, *ATLAS magnet system: Technical Design Report, 1*. Technical Design Report ATLAS. CERN, Geneva, 1997.

[34] G. Aad, M. Ackers, F. A. Alberti, M. Aleppo, G. Alimonti, J. Alonso, E. C. Anderssen, A. Andreani, A. Andreazza, J.-F. Arguin, K. E. Arms, D. Barberis, M. B. Barbero, M. Bazalova, R. B. Beccherle, K. H. Becks, P. K. Behera, F. Bellina, J. Beringer, K. Bernardet, J. B. Biesiada, L. Blanquart, J. Boek, G. R. Boyd, P. Breugnon, P. Buchholz, B. Butler, M. Caccia, A. C. Capsoni, C. Caso, D. Cauz, M. Cepeda, R. Cereseto, M. Cervetto, M. L. Chu, M. Citterio, J. C. Clemens, Y. C. Coadou, M. Cobal, A. Coccaro, S. Coelli, S. Corrard, M. Cristinziani, S. Cuneo, S. Dauria, M. Dameri, G. Darbo, S. Dardin, B. DeLotto, U. De Sanctis, J. B. De Vivie

De Regie, C. del Papa, P. Delpierre, B. Di Girolamo, W. Dietsche, F. Djama, D. Dobos, M. Donega, J. Dopke, K. Einsweiler, A. Eyring, D. Fasching, L. Feligioni, D. Ferguson, W. Fernando, P. Fischer, M. J. Fisher, T. Flick, G. Gagliardi, E. Galyaev, K. K. Gan, M. Garca-Sciveres, N. Garelli, G. G. Gariano, G. G. Gaycken, C. Gemme, P. Gerlach, M. G. D. Gilchriese, M. P. Giordani, D. Giugni, K. W. Glitza, C. Gssling, T. Golling, F. Goozen, I. Gorelov, G. Gorfine, C. Grah, H. M. Gray, I. M. Gregor, J. Grosse-Knetter, K. Grybel, P. Guterrez, G. D. Hallewell, N. Hartman, M. Havranek, B. Heinemann, T. Hen, M. R. Hoeferkamp, D. Hoffmann, M. Holder, W. Honerbach, C. Horn, S. Hou, G. S. Huang, F. Huegging, E. W. Hughes, I. Ibragimov, I. Ilyashenko, M. Imhaeuser, J. M. Izen, J. Jackson, D. Jana, R. C. Jared, P. Jez, T. Johnson, J. Joseph, H. Kagan, M. Karagounis, R. D. Kass, M. Keil, S. Kersten, P. Kind, J. Klaiber-Lodewigs, L. Klingbeil, R. Klingenberg, A. Korn, V. V. Kostyukhin, I. Kostyukhina, O. Krasel, H. Krger, K. Krger, J. Kudlaty, T. Khl, O. Kvasnicka, K. Lantzsch, T. Lari, S. L. Latorre, S. C. Lee, T. Lenz, G. Lenzen, J. Lepidis, J. Levque, M. Leyton, D. Lopez Mateos, K. F. Loureiro, D. Lke, L. Luisa, J. Lys, R. J. Madaras, P. Mttig, F. M. Manca, E. Mandelli, M. Marcisovsky, Z. Marshall, G. Martnez, L. Masetti, M. Ma, M. Mathes, R. McKay, G. Meddeler, R. Meera-Lebbai, C. Meroni, J. Metcalfe, W. T. Meyer, D. W. Miller, W. Miller, S. Montesano, M. M. Monti, P. Morettini, J. M. Moss, T. Mouthuy, P. Nechaeva, W. Ockenfels, G. A. Odino, M. Olcese, B. Osculati, F. Parodi, A. Pekedis, K. Perez, I. Peric, C. Pizzorno, J. Popule, R. Post, F. Ragusa, A. M. Rahimi, B. Raith, S. Rajek, K. Reeves, I. Reisinger, J. D. Richardson, E. I. Rosenberg, L. P. Rossi, I. Rottlnder, A. R. Rovani, A. Rozanov, O. Runlfsson, E. R. Ruscino, A. F. Saavedra, F. S. Sabatini, M. Saleem, S. Sandvoss, B. Sanny, L. Santi, M. I. Scherzer, C. Schiavi, A. Schreiner, J. Schultes, A. Schwartzman, R. Seibert, S. C. Seidel, H. Severini, S. Shanava, P. Scho, P. Skubic, A. C. Smith, D. S. Smith, J. Snow, T. Stahl, T. Stockmanns, S. Strandberg, M. Strauss, D. Ta, F. Tegenfeldt, P. K. Teng, R. Ter-Antonian, J. Thadome, T. Tic, L. Tomasek, M. Tomasek, F. Tomasi, K. Toms, C. Tran, J. Treis, N. Triplett, C. Troncon, L. Vacavant, S. Vahsen, J. Valenta, G. Vegni, F. Vernocchi, E. Vigeolas, J. Virzi, E. Viscione, V. Vrba, J. Walbersloh, W. Walkowiak, J. Weber, T. F. Weber, J. Weingarten, C. Weldon, N. Wermes, U. Werthenbach, J. S. Wirth, R. Witharm, B. Witt, M. Wittgen, J. Wstenfeld, R. Wunstorf, J. Wyckoff, W.-M. Yao, C. Young, R. Zaidan, M. Zdrazil, F. Zetti, J. Zhong, M. Ziolkowski, G. Zizka, and M. M. Zoeller, *ATLAS pixel detector electronics and sensors*, J. Instrum. **3** (2008) P07007.

[35] A. Abdesselam and T. Akimoto, *The Barrel Modules of the ATLAS SemiConductor Tracker*, Tech. Rep. ATL-INDET-PUB-2006-005. ATL-COM-INDET-2006-009. CERN-ATL-COM-INDET-2006-009, CERN, Geneva, Jul, 2006.

[36] A. Abdesselam and F. Anghinolfi, *The ATLAS semiconductor tracker end-cap module*, Nucl. Instrum. Methods Phys. Res., A **575** (2007) no. 3, 353–389.

[37] ATLAS Collaboration, *The ATLAS TRT barrel detector*, Journal of Instrumentation **3**

(2008) no. 02, P02014.

[38] ATLAS Collaboration, *The ATLAS TRT end-cap detectors*, Journal of Instrumentation **3** (2008) no. 10, P10003.

[39] A. Bingl, *The ATLAS TRT and its Performance at LHC*, Journal of Physics: Conference Series **347** (2012) no. 1, 012025.

[40] B. Aubert, B. Beaugiraud, J. Colas, P. Delebecque, L. D. Ciaccio, M. E. Kacimi, P. Ghez, C. Girard, M. Gouanre, D. Goujdami, A. Jeremie, S. Jzquel, R. Lafaye, N. Massol, P. Perrodo, H. Przysiezniak, G. Sauvage, J. Thion, I. Wingerter-Seez, R. Zitoun, Y. Zolnierowski, R. Alforque, H. Chen, J. Farrell, H. Gordon, R. Grandinetti, R. Hackenburg, A. Hoffmann, J. Kierstead, J. Koehler, F. Lanni, D. Lissauer, H. Ma, D. Makowiecki, T. Muller, S. Norton, V. Radeka, D. Rahm, M. Rehak, S. Rajagopalan, S. Rescia, K. Sexton, J. Sondericker, I. Stumer, H. Takai, A. Belymam, D. Benchekroun, C. Driouichi, A. Hoummada, M. Hakimi, M. Knee, R. Stroynowski, B. Wakeland, V. Datskov, V. Drobin, M. Aleksa, J. Bremer, T. Carli, M. Chalifour, J. Chevalley, F. Djama, L. Ema, C. Fabre, P. Fassnacht, F. Gianotti, A. Gonidec, J. Hansen, L. Hervas, T. Hott, C. Lacaste, C. Marin, P. Pailler, A. Pleskatch, D. Sauvage, G. Vandoni, V. Vuillemin, H. Wilkens, S. Albrand, B. Belhorma, J. Collot, P. de Saintignon, D. Dzahini, A. Ferrari, J. Fulachier, M. Gallin-Martel, J. Hostachy, G. Laborie, F. Ledroit-Guillon, P. Martin, J. Muraz, F. Ohlsson-Malek, S. Saboumazrag, S. Viret, R. Othegraven, C. Zeitnitz, D. Banfi, L. Carminati, D. Cavalli, M. Citterio, G. Costa, M. Delmastro, M. Fanti, L. Mandelli, M. Mazzanti, F. Tartarelli, E. Aug, S. Baffioni, J. Bonis, W. Bonivento, C. Bourdarios, C. D. la Taille, L. Fayard, D. Fournier, G. Guilhem, P. Imbert, L. Iconomidou-Fayard, G. L. Meur, M. Mencik, J.-M. Noppe, G. Parrour, P. Puzo, D. Rousseau, A.-C. Schaffer, N. Seguin-Moreau, L. Serin, G. Unal, J.-J. Veillet, F. Wicek, D. Zerwas, F. Astesan, W. Bertoli, B. Canton, F. Fleuret, D. Imbault, D. Lacour, B. Laforge, P. Schwemling, E. Abouelouafa, A. B. Mansour, R. Cherkaoui, Y. E. Mouahhidi, H. Ghazlane, A. Idrissi, K. Bazizi, D. England, V. Glebov, T. Haelen, F. Lobkowicz, P. Slattery, J. Belorgey, N. Besson, M. Boonekamp, D. Durand, J. Ernwein, B. Mansouli, F. Molini, J. Meyer, P. Perrin, J. Schwindling, J. Taguet, H. Zaccone, B. Lund-Jensen, S. Rydstroem, Y. Tayalati, B. Botchev, G. Finocchiaro, J. Hoffman, R. McCarthy, M. Rijssenbeek, J. Steffens, M. Zdrazil, and H. Braun, *Construction, assembly and tests of the {ATLAS} electromagnetic barrel calorimeter*, Nuclear Instruments and Methods in Physics Research Section A: Accelerators, Spectrometers, Detectors and Associated Equipment **558** (2006) no. 2, 388 – 418.

[41] M. Andrieux, B. Belhorma, A. Belymam, D. Benchekroun, R. Cherkaoui, C. Clement, J. Collot, P. de Saintignon, C. Driouichi, D. Dzahini, Y. E. Mouahhidi, H. Erridi, A. Ferrari, H. Ghazlane, J. Hostachy, A. Hoummada, A. Idrissi, G. Laborie, B. Lund-Jensen, P. Martin, J. Muraz, and J. Soederqvist, *Construction and test of the*

first two sectors of the ATLAS barrel liquid argon presampler, Nuclear Instruments and Methods in Physics Research Section A: Accelerators, Spectrometers, Detectors and Associated Equipment **479** (2002) no. 2-3, 316 – 333.

[42] A. E. L. A. E. C. Group, M. Aleksa, F. Astesan, D. Banfi, F. Barreiro, P. Barrillon, C. Benchouk, W. Bertoli, J. Bremer, H. M. Braun, B. Canton, L. Carminati, T. Carli, C. Cerna, M. Chalifour, J. L. Chevalley, M. Citterio, J. Collot, G. Costa, P. Dargent, B. Dekhissi, J. E. Derkaoui, F. Djama, C. Fabre, A. Fallou, M. Fanti, P. Fassnacht, D. Fournier, C. G. Ruiz, F. Gianotti, J. Giner, A. Gonidec, F. Henry-Couannier, L. Hervas, T. Hott, F. Hubault, D. Imbault, P. Karst, V. A. Kazanin, K. Y. Kotov, L. Labarga, D. Lacour, B. Laforge, P. Lopez-Iturriaga, G. Mac, V. Malychev, L. Mandelli, P. S. Mangeard, B. Mansouli, C. P. Marin, A. L. Maslennikov, M. Mazzanti, J. P. Meyer, E. Monnier, E. N. D. Busto, V. Niess, C. Oliver, I. A. Orlov, P. M. Pailler, S. V. Peleganchuk, J. D. Peso, A. Pleskatch, P. Pralavorio, S. Prat, P. Puzo, M. Raymond, B. Resende, S. Rodier, P. Romero, F. Rossel, D. Sauvage, A. G. Schamov, P. Schwemling, J. Schwindling, C. Serfon, J. Setien, L. Serin, A. Soukharev, C. D. L. Taille, A. Talyshev, G. Tartarelli, Y. A. Tikhonov, S. Tisserant, J. Toth, G. Unal, G. Vandoni, J. J. Veillet, V. Vuillemin, H. G. Wilkens, and H. Zhang, *Construction, assembly and tests of the ATLAS electromagnetic end-cap calorimeters*, Journal of Instrumentation **3** (2008) no. 06, P06002.

[43] ATLAS TileCal Collaboration Collaboration, J. Abdallah, P. Adragna, C. Alexa, R. Alves, P. Amaral, A. Ananiev, K. Anderson, X. Andresen, A. Antonaki, V. Batusov, P. Bednar, E. Bergeaas, C. Biscarat, O. Blanch, G. Blanchot, C. Bohm, V. Boldea, F. Bosi, M. Bosman, C. Bromberg, Y. A. Budagov, D. Calvet, C. Cardeira, T. Carli, J. Carvalho, M. Cascella, M. V. Castillo, J. Costello, M. Cavalli-Sforza, V. Cavasinni, A. S. Cerqueira, C. Clment, M. Cobal, F. Cogswell, S. Constantinescu, D. Costanzo, P. Da Silva, M. Davidek, T. David, J. Dawson, K. De, T. Del Prete, B. Di Girolamo, S. Dita, J. Dolejsi, Z. Dolezal, A. Dotti, R. Downing, G. Drake, I. Efthymiopoulos, D. Errede, S. Errede, A. Farbin, D. Fassouliotis, E. Feng, A. Fenyuk, C. Ferdi, B. C. Ferreira, A. Ferrer, V. Flaminio, J. Flix, P. Francavilla, E. Fullana, V. Garde, K. Gellerstedt, V. Giakoumopoulou, V. Giangiobbe, O. Gildemeister, V. Gilewsky, N. Giokaris, N. Gollub, A. Gomes, V. Gonzlez, J. Gouveia, P. Grenier, P. Gris, V. Guarino, C. Guicheney, A. Sen-Gupta, H. Hakobyan, M. Haney, S. Hellman, A. Henriques, E. Hign, N. Hill, S. Holmgren, I. Hruska, M. Hurwitz, J. Huston, I. Jen-La Plante, K. Jon-And, T. Junk, A. Karyukhin, J. Khubua, J. Klereborn, S. Kopikov, I. Korolkov, P. Krivkova, Y. Kulchitsky, Y. Kurochkin, P. Kuzhir, V. Lapin, T. Le Compte, R. Lefvre, R. Leitner, J. Li, M. Liablin, M. Lokajcek, Y. Lomakin, P. Lourtie, L. Lovas, A. Lupi, C. Maidantchik, A. Maio, S. Maliukov, A. Manousakis, C. Marques, F. Marroquim, F. Martin, E. Mazzoni, F. S. Merritt, A. Myagkov, R. Miller, I. Minashvili, L. Miralles, G. Montarou, S. Nmcek, M. Nessi, I. Nikitine, L. Nodulman, O. Norniella, A. Onofre, M. Oreglia, B. Palan, D. Pallin, D. Pantea, A. Pereira, J. E. Pilcher, J. Pina, J. Pinho, E. Pod, F. Podlyski, X. Portell, J. Poveda, L. Pribyl, L. E. Price,

J. Proudfoot, M. Ramalho, M. Ramstedt, L. Raposeiro, J. Reis, R. Richards, C. Roda, V. Romanov, P. Rosnet, P. Roy, A. Ruiz, V. Rumiantsau, N. Russakovich, J. Sada Costa, O. Salto, B. Salvacha, E. Sanchis, H. Sanders, C. Santoni, J. Santos, J. G. Saraiva, F. Sarri, L. P. Says, G. Schlager, J. L. Schlereth, J. M. Seixas, B. Selldn, N. Shalanda, P. Shevtsov, M. Shochet, V. Simaitis, M. Simonyan, A. Sisakian, J. Sjlin, C. Solans, A. Solodkov, J. Solovianov, O. Silva, M. Sosebee, F. Span, P. Speckmeyer, R. Stanek, E. Starchenko, P. Starovoitov, M. Suk, I. Sykora, F. Tang, P. Tas, R. Teuscher, S. Tokar, N. Topilin, J. Torres, D. Underwood, G. Usai, A. Valero, S. Valkr, J. A. Valls, A. Vartapetian, F. Vazeille, C. Vellidis, F. Ventura, I. Vichou, I. Vivarelli, M. Volpi, A. White, A. Zaitsev, A. Zenin, T. Zenis, Z. Zenonos, S. Zenz, and B. Zilka, *Design, Construction and Installation of the ATLAS Hadronic Barrel Scintillator-Tile Calorimeter*, Tech. Rep. ATL-TILECAL-PUB-2008-001. ATL-COM-TILECAL-2007-019, CERN, Geneva, Nov, 2007.

[44] D. M. Gingrich, G. Lachat, J. L. Pinfold, J. Soukup, D. Axen, C. Cojocaru, G. Oakham, M. O'Neill, M. G. Vincter, M. Aleksa, J. Bremer, M. Chalifour, C. Fabre, P. Fassnacht, A. Gonidec, P. Pailler, G. Vandoni, A. Cheplakov, V. Datskov, V. Drobin, A. Fedorov, S. Golubykh, N. Javadov, V. Kalinnikov, S. Kakurin, M. Kazarinov, V. Kukhtin, E. Ladygin, A. Lazarev, A. Neganov, I. Pisarev, N. Rousakovitch, E. Serochkin, S. N. Shilov, A. N. Shalyugin, Y. Usov, J. Bn, D. Bruncko, E. Kladiva, P. Stavina, P. Strzenec, M. Heldmann, M. Hohlfeld, K. Jakobs, L. Kpke, E. Marschalkowski, D. Meder, R. Othegraven, U. Schfer, D. Schroff, H. Secker, J. Thomas, W. Walkowiak, C. Zeitnitz, G. Azuelos, P.-A. Delsart, C. Leroy, R. Mazini, R. Mehdiyev, A. Akimov, M. Blagov, A. Komar, A. Snesarev, M. N. Speransky, V. Sulin, M. Yakimenko, M. Aderholz, T. Barillari, H. Brettel, W. Cwienk, J. Fent, A. Fischer, J. Habring, J. Huber, A. Karev, A. E. Kiryunin, L. Kurchaninov, H. Laskus, S. Menke, P. Mooshofer, H. Oberlack, D. Salihagic, P. Schacht, H. Schmcker, H. Stenzel, D. Striegel, W. Tribanek, J. Zimmer, T. Chen, J. Ping, M. Qi, A. Falou, G. Mace, S. V. Chekulaev, S. Denisov, M. Levitsky, A. Minaenko, G. Y. Mitrofanov, A. Moiseev, A. Pleskatch, V. V. Sytnik, L. Zakamsky, P. Benoit, K. W. Hoyle, A. Honma, M. J. Losty, R. Maharaj, C. J. Oram, E. W. Pattyn, M. Rosvick, C. Sbarra, H. P. Wellisch, M. Wielers, P. S. Birney, M. Dobbs, M. Fincke-Keeler, D. Fortin, T. A. Hodges, T. Ince, N. Kanaya, R. K. Keeler, R. Langstaff, M. Lefebvre, R. A. McPherson, D. C. O'Neil, R. Seuster, D. Forbush, P. Mockett, F. Toevs, and H. M. Braun, *Construction, assembly and testing of the ATLAS hadronic end-cap calorimeter*, Tech. Rep. ATL-LARG-PUB-2007-009. CERN-ATL-COM-LARG-2007-006, CERN, Geneva, Apr, 2007.

[45] R. S. Orr, *THE ATLAS FORWARD CALORIMETER*, Tech. Rep. ATL-LARG-PROC-2011-007, CERN, Geneva, Oct, 2011.

[46] *The ATLAS Forward Calorimeter*, JINST **3** (2008) no. 02, P02010. `http://stacks.iop.org/1748-0221/3/i=02/a=P02010`.

[47] ATLAS Collaboration Collaboration, *ATLAS muon spectrometer: Technical Design Report*. Technical Design Report ATLAS. CERN, Geneva, 1997. distribution.

[48] ATLAS Collaboration Collaboration, *ATLAS level-1 trigger: Technical Design Report*. Technical Design Report ATLAS. CERN, Geneva, 1998.

[49] ATLAS Collaboration Collaboration, P. Jenni, M. Nessi, M. Nordberg, and K. Smith, *ATLAS high-level trigger, data-acquisition and controls: Technical Design Report*. Technical Design Report ATLAS. CERN, Geneva, 2003.

[50] M. Cacciari, G. Salam, and G. Soyez, *The anti-kt jet clustering algorithm*, Journal of High Energy Physics **2008** (2008) no. 04, 063.

[51] ATLAS Collaboration Collaboration, *b-jet tagging calibration on c-jets containing D^{*+} mesons*, Tech. Rep. ATLAS-CONF-2012-039, CERN, Geneva, Mar, 2012.

[52] ATLAS Collaboration Collaboration, *Commissioning of the ATLAS high-performance b-tagging algorithms in the 7 TeV collision data*, Tech. Rep. ATLAS-CONF-2011-102, CERN, Geneva, Jul, 2011.

[53] A. Hoecker, P. Speckmayer, J. Stelzer, J. Therhaag, E. von Toerne, and H. Voss, *TMVA: Toolkit for Multivariate Data Analysis*, PoS **ACAT** (2007) 040, `arXiv:physics/0703039`.

[54] ATLAS Collaboration Collaboration, *Measurement of the Mistag Rate with 5 fb^{-1} of Data Collected by the ATLAS Detector*, Tech. Rep. ATLAS-CONF-2012-040, CERN, Geneva, Mar, 2012.

[55] *Performance of Missing Transverse Momentum Reconstruction in ATLAS studied in Proton-Proton Collisions recorded in 2012 at 8 TeV*, Tech. Rep. ATLAS-CONF-2013-082, CERN, Geneva, Aug, 2013.

[56] P. Sturm and W. Wagner, *Measurement of the t-Channel Single Top-Quark Production Cross-Section with the ATLAS Detector at $\sqrt{s} = 7$ TeV*. PhD thesis, Wuppertal U., Wuppertal, Nov, 2012. Presented 01 Jun 2012.

[57] GEANT4 Collaboration, S. Agostinelli et al., *GEANT4: A simulation toolkit*, Nucl. Instrum. Meth. A **506** (2003) 250–303.

[58] M. L. Mangano, M. Moretti, F. Piccinini, R. Pittau, and A. D. Polosa, *ALPGEN, a generator for hard multiparton processes in hadronic collisions*, JHEP **07** (2003) 001.

[59] P. Nason, *A new method for combining NLO QCD computations with parton shower simulations*, JHEP 11(2004)-040, hep-ph/0409146 (2004) .

[60] J. Alwall, M. Herquet, F. Maltoni, O. Mattelaer, and T. Stelzer, *MadGraph 5 : Going Beyond*, JHEP **1106** (2011) 128, `arXiv:1106.0522 [hep-ph]`.

[61] T. Sjostrand, S. Mrenna, and P. Skands, *PYTHIA Generator version 6.418*, JHEP **05** (2006) 026.

[62] G. Corcella et al., *HERWIG 6.5: an event generator for Hadron Emission Reactions With Interfering Gluons (including supersymmetric processes)*, JHEP **01** (2001) 010.

[63] B. P. Kersevan and R. W. Elzbieta, *The Monte Carlo Event Generator AcerMC version 3.5 with interfaces to PYTHIA 6.4, HERWIG 6.5 and ARIADNE 4.1*, hep-ph/0405247 (2008) .

[64] N. Kidonakis, *NNLL resummation for s-channel single top quark production*, Phys.Rev. **D81** (2010) 054028, `arXiv:1001.5034 [hep-ph]`.

[65] N. Kidonakis, *Next-to-next-to-leading-order collinear and soft gluon corrections for t-channel single top quark production*, Phys.Rev. **D83** (2011) 091503, `arXiv:1103.2792 [hep-ph]`.

[66] N. Kidonakis, *Two-loop soft anomalous dimensions for single top quark associated production with a W- or H-*, Phys.Rev. **D82** (2010) 054018, `arXiv:1005.4451 [hep-ph]`.

[67] M. Cacciari, M. Czakon, M. Mangano, A. Mitov, and P. Nason, *Top-pair production at hadron colliders with next-to-next-to-leading logarithmic soft-gluon resummation*, Phys.Lett. **B710** (2012) 612–622, `arXiv:1111.5869 [hep-ph]`.

[68] T. A. collaboration, *Single Boson and Diboson Production Cross Sections in pp Collisions at* $\sqrt{s} = 7$ *TeV*, .

[69] J. M. Campbell and R. Ellis, *MCFM for the Tevatron and the LHC*, Nucl.Phys.Proc.Suppl. **205-206** (2010) 10–15, `arXiv:1007.3492 [hep-ph]`.

[70] ATLAS Collaboration, K. Becker et al., *Estimation of Fake Lepton Background for Top Analyses Using the* $\sqrt{s} = 8$ *TeV Dataset*, ATL-COM-PHYS-2013-1100. `https://cds.cern.ch/record/1571043/`.

[71] B. P. e. a. Roe, *Boosted Decision Trees as an Alternative to Artificial Neural Networks for Particle Identification*, physics/0408124v2 (2004) .

[72] F. J. Massey, *The Kolmogorov-Smirnov Test for Goodness of Fit*, Journal of the American Statistical Association **46** (1951) no. 253, 68–78.

[73] ATLAS top group, *TopSystematicUncertainties, 2012*, .

[74] S. Adomeit, F. Balli, T. Carli, C. Doglioni, D. Gillberg, G. Halladjian, B. Malaescu, L. Mijovic, C. Meyer, A. Picazio, S. Schramm, A. Schwartzman, J. Taenzer, K. Terashi, and D. Lopez Mateos, *Jet energy scale and its systematic uncertainty in proton-proton collisions at sqrt(s)=7 TeV with ATLAS 2011 data*, Tech. Rep. ATLAS-COM-CONF-2012-171, CERN, Geneva, Aug, 2012.

[75] [ATLAS Collaboration] Collaboration, G. Aad et al., *Jet energy resolution in proton-proton collisions at sqrt(s)=7 TeV recorded in 2010 with the ATLAS detector*, The European Physical Journal C **73** (2013) no. 3, 1–27. http://dx.doi.org/10.1140/epjc/s10052-013-2306-0.

[76] ATLAS Collaboration, *Jet Reconstruction Efficiency*, https://twiki.cern.ch/twiki/bin/viewauth/AtlasProtected/TopJetReconstructionEfficiency.

[77] T. A. collaboration, *Pile-up subtraction and suppression for jets in ATLAS*, .

[78] ATLAS Collaboration Collaboration, *b-jet tagging calibration on c-jets containing D^{*+} mesons*, Tech. Rep. ATLAS-CONF-2012-039, CERN, Geneva, Mar, 2012.

[79] ATLAS Collaboration Collaboration, *Measurement of the Mistag Rate with 5 fb^{-1} of Data Collected by the ATLAS Detector*, Tech. Rep. ATLAS-CONF-2012-040, CERN, Geneva, Mar, 2012.

[80] G. Aad et al., *Electron performance measurements with the ATLAS detector using the 2010 LHC proton-proton collision data*, The European Physical Journal C **72** (2012) no. 3, 1–46. http://dx.doi.org/10.1140/epjc/s10052-012-1909-1.

[81] *Preliminary results on the muon reconstruction efficiency, momentum resolution, and momentum scale in ATLAS 2012 pp collision data*, Tech. Rep. ATLAS-CONF-2013-088, CERN, Geneva, Aug, 2013.

[82] A. Martin, W. Stirling, R. Thorne, and G. Watt, *Uncertainties on alpha(S) in global PDF analyses and implications for predicted hadronic cross sections*, Eur.Phys.J. **C64** (2009) 653–680, arXiv:0905.3531 [hep-ph].

[83] R. D. Ball, L. Del Debbio, S. Forte, A. Guffanti, J. I. Latorre, et al., *A first unbiased global NLO determination of parton distributions and their uncertainties*, Nucl.Phys. **B838** (2010) 136–206, arXiv:1002.4407 [hep-ph].

[84] ATLAS Collaboration Collaboration, G. Aad et al., *Measurement of $t\bar{t}$ production with a veto on additional central jet activity in pp collisions at sqrt(s) = 7 TeV using the ATLAS detector*, Eur.Phys.J. **C72** (2012) 2043, arXiv:1203.5015 [hep-ex].

[85] ATLAS Collaboration, G. Aad et al., *Improved luminosity determination in pp collisions at $\sqrt{s}$ = 7 TeV using the ATLAS detector at the LHC*, Eur.Phys.J. **C73** (2013) 2518, arXiv:1302.4393 [hep-ex].

[86] T. Junk, *Confidence level computation for combining searches with small statistics*, Nucl.Instrum.Meth. **A434** (1999) 435–443, arXiv:hep-ex/9902006 [hep-ex].

[87] A. L. Read, *Presentation of search results: the CL_s technique*, J. Phys. G **28** (2002) no. 10, 2693–704.

[88] T. Junk, *Confidence level computation for combining searches with small statistics*, Nucl. Instrum. Meth. **A434** (1999) 435–443, arXiv:hep-ex/9902006 [hep-ex].

[89] CDF Collaboration Collaboration, F. Anza et al., *Search for W'-like resonances decaying to tb in the E/T plus jets sample with the full CDF dataset*, 2014.

[90] *Search for $W' \to t\bar{b}$ in proton-proton collisions at a centre-of-mass energy of $\sqrt{s}$ = 8 TeV with the ATLAS detector*, Tech. Rep. ATLAS-CONF-2013-050, CERN, Geneva, May, 2013.

[91] Z. Sullivan, *Next-to-leading order pp -¿ W' -¿ tb production at 14 TeV and 33 TeV*, arXiv:1308.3797 [hep-ph].

[92] *Search for W' resonances decaying into t b-bar with fully hadronic final state with 20 $fb^{-}1$ of 8 TeV pp collisions*, Summer, 2014.